SIMULATION OF NONLINEAR ELECTRONIC SPECTROSCOPY IN THE CONDENSED PHASE

LAURENCE E. FRIED* and SHAUL MUKAMEL

Department of Chemistry, University of Rochester, Rochester, New York

CONTENTS

*Current address: Chemistry and Materials Science Department, L-277, Lawrence Livermore National Laboratory, Livermore, CA.

Advances in Chemical Physics, Volume LXXXIV, Edited by I. Prigogine and Stuart A. Rice.
ISBN 0-471-58926-5

I. INTRODUCTION

The simulation of spectroscopic measurements is useful because it allows direct connections to be made between theory and experiment. Comparison of simulated results to experiment can either be used to improve potential functions or offer interpretations of experimental results. Comparison of simulations with solvable models can provide invaluable physical insight. The information gained by simulating spectroscopic observables, however, is only as good as the simulation methods themselves.

We will concern ourselves here with simulation of the spectroscopy of large systems. We will call these large systems "condensed phase," although the methods discussed here could just as well be applied to a single protein or to an atomic cluster. Since exact quantum dynamics cannot be computed for large systems, it is necessary to use semiclassical techniques. Methods for simulating infrared (IR) spectra and off-resonant light scattering in the condensed phase have been extensively discussed in the pioneering work of Hellwarth [1] and in several important simulation studies [2–7]. The unifying feature of these techniques is that the experimental signal is the Fourier transform of a time-correlation function [8,9] on the ground-state potential surface. IR spectroscopy probes the dipole autocorrelation function, whereas light scattering probes the polarizability autocorrelation function. These correlation functions have a well-defined classical limit where the relevant operator (dipole operator, polarizability operator) is replaced by its classical analogue, and the time evolution is calculated classically. Much work has also been done on the semiclassical quantization of isolated molecules [10–14], focusing primarily on the calculation of single vibrational eigenstates. In the condensed phase, however, it is most appropriate to concentrate on *lineshapes* which span many eigenstates and contain coarse grained information [15].

In contrast to IR and light-scattering spectroscopies, many experimental techniques involve electronic transitions. The interest in electronic spectroscopy in the condensed phase has grown in recent years. This growth has been fueled by the availability of ultrafast ultraviolet and visible light sources as well as by recent progress in nonlinear spectroscopic techniques. Much more interesting dynamical information can be extracted from nonlinear spectroscopic techniques [16–28] than from the electronic absorption spectrum [29–32]. For example, while the electronic absorption spectrum is often dominated by inhomogeneous broadening, nonlinear spectroscopies such as hole burning [33–37] and photon echo spectroscopy [38–40] eliminate inhomogeneous broadening.

As with the IR spectra, it is possible to express electronic spectra using

a dipole correlation function. This correlation function, however, does not have a classical limit, since the electronic transition dipole for a two-level system [29] has no classical counterpart [41]. This is reflected by its singular dependence on $\hbar$. Any semiclassical method must therefore be based on a *subjective* choice of reference model, rather than on a direct expansion [42] in $\hbar$. It is left to physical intuition to choose reasonable semiclassical approximations for electronic spectroscopy [43]. An equivalent way to view the difficulties encountered in the classical simulation of electronic spectroscopy is to note that these spectroscopies depend on nuclear dynamics when the system is in an electronic coherence. By an electronic coherence, we mean that the right (bra) side of the density matrix is in a different electronic state than the left (ket) side. An electronic coherence has no classical analogue.

The general formulation of nonlinear spectroscopy in the condensed phase using the density matrix in Liouville space was recently reviewed [32], as was the application of the multimode Brownian oscillator model [44,45] to nonlinear spectroscopy. We shall attempt to resolve here what the best current simulation techniques are for resonant and near-resonant electronic spectroscopy. It is our hope that this chapter will help clarify the advantages and shortcomings of various computational methods and analytical models.

A second, equally important, question considered in this chapter is how to interpret nonlinear spectroscopy in the condensed phase. We undertake a comprehensive examination of the spectroscopy of benzene–Ar_N clusters. We show that the multimode Brownian oscillator model gives a simple way of interpreting the spectra of clusters. We also present an analysis of how spectroscopic observables converge to the bulk in these systems. We find that there are substantial non-bulk effects visible in the spectroscopy of benzene–Ar_N clusters even at $N = 200$, although the average energy per particle behaves in a bulk-like manner for $N \geq 50$.

One of the most interesting results of our numerical studies is that benzene–Ar_N clusters can show jump-type dynamics (i.e., the potential energy shows sudden jumps as a function of time) typical of phase coexistence. The existence of such jumps prompts us to consider how spectroscopic techniques could monitor this sort of dynamics, and how simulation methods treat jump dynamics. It also leads us to study the physical behavior behind the jumps, with our principal finding being that the jumps are due to a shell-specific "melting" (i.e., a transition to large amplitude motion).

Since this chapter covers a broad range of subject matter, we have organized it into parts that may be read more or less independently. Each section is broken into several subsections, and long subsections are

followed by a brief summary. We hope that this format will help readers who are not interested in technical details to find the main points of this review. Section II discusses and compares various methods for calculating spectroscopic observables in the condensed phase. We also consider how experimental results can be analyzed in terms of an inhomogeneous distribution of a few Brownian oscillators. Section III then applies these methods to the spectroscopy of benzene–Ar clusters. The review is concluded with (a) appendices concerning the scaling of spectroscopic observables with size, (b) analytical results concerning model problems, and (c) a discussion of how to map classical simulation results onto a quantum mechanical model system.

II. SEMICLASSICAL THEORY OF OPTICAL LINESHAPES

In this section we discuss semiclassical methods for simulating the linear and nonlinear optical spectroscopy of a chromophore in a solvent. The methods discussed here are independent of the precise nature of the chromophore and solvent, except that chromophore vibronic transitions should be well separated from solvent vibronic transitions. We assume that there is only one relevant excited electronic state of the chromophore which is sufficiently close to the laser frequency to dominate the optical response. The chromophore in its ground electronic state is denoted by $|g\rangle$, whereas the chromophore in the excited electronic state is denoted by $|e\rangle$. This model applies for a wide variety of chromophore–solvent combinations: Examples include benzene–argon [46] and Nile blue–ethylene glycol [47].

The motivation for using semiclassical methods is that an exact quantum mechanical treatment of a system with many degrees of freedom (N) is impossible, since the computational work of a matrix diagonalization scales exponentially with the number of degrees of freedom. On the other hand, simple phenomenological models, such as the Bloch equations [29,48,49], are often inadequate. Recent experiments on photon echoes in liquids [40,50,51] provide good examples of the limitations of the Bloch equations. The inadequacy of the Bloch approach is evident in nonlinear spectroscopies, which can eliminate inhomogeneous broadening and are thus more sensitive to dynamical details. The computational work of the methods considered here is dominated by the force evaluations necessary to run a trajectory, which scale as N^2. While it is possible to formulate more exact algorithms, we believe that the techniques considered here represent a good compromise between accuracy and computational cost. In the following subsection we consider the qualitative effects that a theory of spectroscopy in the condensed phase must reproduce.

A. Features of Spectroscopy in the Condensed Phase

A successful theory of spectroscopy in condensed phases must incorporate many physical processes. The first is inhomogeneous broadening. Inhomogeneous broadening occurs because the chromophore can experience distinct solvent environments which do not interconvert on the experimental timescale. Therefore, the concept of inhomogeneous broadening always carries with it the implicit notion of an underlying *experimental* "timescale of interest," which we will call τ_r. In the context of linear absorption, τ_r is clearly the inverse of the absorption linewidth [27,52–54]. In the context of nonlinear spectroscopy, however, one must be careful about the definition of τ_r. For instance, ultrashort laser pulses can limit the experimental time τ_r to be less than the inverse absorption lineshape. A system that is inhomogeneously broadened has a distribution of transition frequencies $W(\omega_{eg})$. In liquids, $W(\omega_{eg})$ often is a Gaussian. The recurrence of a Gaussian $W(\omega_{eg})$ in many different physical contexts [55] is a consequence of the central limit theorem, which states that a sum of many independent processes will have a Gaussian probability distribution. For condensed-phase systems the "independent processes" are the interactions of the chromophore with each solvent atom. The extent to which the effective number of processes is large and the extent to which they are independent are controlled by system size (if finite) and by the long-range nature of interactions and correlations. Many systems have $W(\omega_{eg})$ distributions that are strongly non-Gaussian. A good example of this occurs in cluster spectra, which can be dominated by one or two isomers [56,57].

In addition to $W(\omega_{eg})$, a successful theory of spectroscopy in the condensed phase must take into account nuclear dynamics. In linear spectroscopy, nuclear dynamics during an optical transition lead to vibrational structure in the spectrum, or to motional narrowing, depending on whether the nuclear dynamics is oscillatory or overdamped. In the motional narrowing mechanism [58,59], overdamped nuclear dynamics produce (a) a narrowing of the linear absorption spectrum $I(\omega)$ and (b) and a corresponding increase in the far wings of $I(\omega)$.

Nuclear dynamics can also have a profound influence on nonlinear spectroscopies. In nonlinear spectroscopy, vibrations can occur either during an optical transition (when the system is in an electronic coherence) or in-between optical transitions [when the system is in an electronic population; see Eqs. (2.11a)–(2.11d)]. Once again, we can qualitatively classify the system vibrations as being underdamped or overdamped in nature. Coherent (underdamped) vibrations lead to quantum beats [23,60–64], in which the measured signal oscillates at the difference

between two or more vibrational frequencies. Coherent vibrations which occur when the system is in an electronic population cause the quantum beats found in impulsive stimulated scattering (ISS) spectroscopy [23,60]. Underdamped vibrations which occur during an electronic coherence produce structured spectra in hole burning spectroscopy [33]. Overdamped nuclear dynamics also lead to well-known effects in nonlinear spectroscopy. Overdamped dynamics while the system is in an electronic coherence is responsible for the decay of a photon echo signal [65]. Overdamped dynamics while the system is in an electronic coherence produces the time-resolved Stokes shift [22,66–68], which is a direct probe of solvation dynamics.

So far we have implicitly assumed that there is a clear separation between dynamics and inhomogeneous effects. This separation is by no means universal. Analysis of Raman excitation profiles for various chromophores in liquids using a stochastic model have shown that the system is in the *intermediate modulation* regime [31,69–71], where the timescale of nuclear dynamics is of the same order of magnitude as the inverse absorption linewidth. This was confirmed by recent photon echo experiments in polar solvents [50,51]. Simulations [72] have demonstrated that the spectroscopy of a small polar dye in water is also in the intermediate modulation regime. Thus, it can be artificial and perhaps misleading to speak of inhomogeneous versus dynamical effects. Rather, one should speak of a distribution of nuclear frequencies $W_v(\omega)$. This distribution should not be confused with the distribution of electronic transition frequencies $W(\omega_{eg})$ discussed above. The concepts of inhomogeneous broadening and homogeneous broadening only have meaning when $W_v(\omega)$ and τ_r are specified. Vibrations whose frequencies are much less than $1/\tau_r$ contribute to inhomogeneous broadening, whereas vibrations whose frequencies are much greater than $1/\tau_r$ contribute to homogeneous broadening. In general, however, lineshapes can lie in the regime which is between the inhomogeneous and homogeneous limits.

Although we are discussing semiclassical techniques, quantum mechanical effects can also be crucial. Obviously, semiclassical techniques can only have a limited ability to build in quantum effects. For instance, tunneling is completely beyond the scope of the methods discussed here. Two effects, however, can be simply incorporated into semiclassical techniques. The first of these is zero-point motion. The time-honored way of including zero-point motion is to assign the system to an optimal harmonic reference system [73], then let the energy $E = \Sigma_i \hbar\omega_i[\bar{n}(\omega_i) + \frac{1}{2}]$, where ω_i is the frequency of mode i in the harmonic reference system, and

$$\bar{n}(\omega) \equiv [\exp(\hbar\omega/k_B T) - 1]^{-1} . \tag{2.1}$$

Here T is the temperature and k_B is Boltzmann's constant. Methods for obtaining a harmonic reference system for a liquid have been proposed [74–76].

There are effects due to vibrational quantization besides zero-point energy. One experimental manifestation of quantized vibrations is that the electronic absorption spectrum becomes more asymmetric because the $|v_g = 0\rangle \rightarrow |v_e = n\rangle$ absorption is allowed at low temperatures, but the $|v_g = n\rangle \rightarrow |v_e = 0\rangle$ absorption is not allowed for $k_B T \ll \hbar\omega$. As we discuss below, some of the features of vibrational quantization can be reproduced in a classical simulation by once again invoking a harmonic reference system.

A final effect to be considered is the shape of the ground- and excited-state potential energy surfaces. Some physical effects depend crucially on anharmonicity. A good example is reactive pump–probe spectroscopy [18,77–79]. Many standard ways of treating spectroscopy in condensed phases, such as stochastic models [58,59,80], implicitly assume that the ground- and excited-state potential energy surfaces have the same frequency. This assumption is a common feature of linearized theories of solvation [81,82] which expand the spectroscopic response in powers of the solute–solvent interaction. While linear solvation theories can be successful in many contexts (the Marcus theory of electron transfer [83] is a prime example [55]), nonlinear spectroscopies can be sensitive to differences between ground- and excited-state frequencies. Therefore linear solvation theory often does not hold for nonlinear spectroscopies.

To summarize, a successful theory of spectroscopy in the condensed phase should include the following ingredients:

- *Distribution of transition frequencies:* The chromophore can experience a distribution of static solvent environments. The resulting distribution of transition frequencies $W(\omega_{eg})$ is often Gaussian. However, non-Gaussian $W(\omega_{eg})$ [84] are both important and common.

- *Nuclear dynamics:* Nuclear dynamics can be either coherent or overdamped in character, and can occur when the system is in an electronic coherence or when it is in an electronic population. Each type of nuclear motion causes separate spectroscopic effects.

- *Distribution of system timescales:* Condensed-phase systems (e.g., liquids, glasses [85–87], and clusters [88]) can have a broad, continuous distribution of timescales, ranging from the femtosecond regime to microseconds [88]. The classification of line broadening as either inhomogeneous or homogeneous is usually not possible.

- *Vibrational quantization:* Semiclassical simulations can take into account some limited but important vibrational quantum effects. Zero-point motion and vibrational quantization can be accounted for by adopting a harmonic reference system, and then building in quantum effects based on the reference system.
- *Potential shape:* The ground- and excited-state potential energy surfaces can be anharmonic and can have shapes that are different from one another. Thus, linearized solvation theories, which assume that the ground and excited potential energy surfaces have the same shape, are often significantly in error.

B. Formulation of Linear and Nonlinear Spectroscopy

In this section we review the formulation of linear and four-wave mixing spectroscopies [45,89]. We consider the nonlinear spectroscopy of a chromophore in a solvent. The chromophore is assumed to have two relevant electronic states, $|g\rangle$ (the ground state) and $|e\rangle$ (the excited state). In other words, we assume that the applied laser frequencies are close enough to resonance that transitions between $|g\rangle$ and $|e\rangle$ dominate all others. We also assume that the chromophore electronic transition $|e\rangle \leftarrow |g\rangle$ is far away from any solvent electronic transitions. The Hamiltonian for this system in the presence of an electric field $\mathbf{E}(t)$ is

$$H_T = H - \boldsymbol{\mu} \cdot \mathbf{E}(t)\,, \tag{2.2a}$$

where

$$H = |g\rangle H_g(\mathbf{Q}, \mathbf{P})\langle g| + |e\rangle H_e(\mathbf{Q}, \mathbf{P})\langle e|\,, \tag{2.2b}$$

$$H_g = \sum_i \frac{\mathbf{P}_i^2}{2m_i} + V_g(\mathbf{Q})\,, \tag{2.2c}$$

$$H_e = \sum_i \frac{\mathbf{P}_i^2}{2m_i} + V_e(\mathbf{Q}) + \omega_{eg}^0\,, \tag{2.2d}$$

$$\boldsymbol{\mu} = |e\rangle \boldsymbol{\mu}_{eg} \langle g| + |g\rangle \boldsymbol{\mu}_{ge} \langle e|\,. \tag{2.2e}$$

Here, H_g and H_e are the adiabatic Hamiltonians of the chromophore plus solvent system. The set of nuclear positions is represented by the vector $\mathbf{Q}$. The set of nuclear momenta is represented by the vector $\mathbf{P}$. ω_{eg}^0 is the gas-phase 0–0 absorption frequency of the chromophore. V_j ($j = g, e$) is the adiabatic potential surface associated with state j. $\mathbf{P}_i$ is the momentum of atom i, and m_i is its mass.

In the discussion that follows, we will make the Franck–Condon approximation and neglect the coordinate dependence of the transition dipole μ_{eg}. (This approximation is distinct from the classical Condon approximation discussed below.) Once this approximation is made, the vector nature of the electric field and polarization may also be eliminated. We then use $E(t)$ to denote the electric field and use $P(t)$ to denote the polarization. We also set $\mu_{eg} = 1$ without loss of generality. $\hbar = 1$ units are used in all equations.

The interaction between light and matter produces an optical polarization $P(t)$:

$$P(t) \equiv \mathrm{Tr}[\mu\hat{\rho}(t)], \tag{2.3}$$

where $\hat{\rho}(t)$ is the thermal density matrix of the matter, evolved with the Hamiltonian H_T:

$$\hat{\rho}(t) \equiv e^{-itH_T}|g\rangle\hat{\rho}_g\langle g|e^{itH_T}, \tag{2.4}$$

where T is the temperature and k_B is Boltzmann's constant. Here we assume $\hbar\omega^0_{eg} \gg k_B T$. $\hat{\rho}_g$ is the thermal density matrix:

$$\hat{\rho}_g \equiv e^{-H\hat{g}/kT}/\mathrm{Tr}[e^{-H_g/kT}].$$

The optical polarization $P(t)$ acts as a source in the Maxwell equations [29] and produces light which is detected as the signal. If the detector has the same direction and polarization as one of the lasers, the signal will be related linearly to P for the optically thin samples considered here. This occurs in pump–probe spectroscopy where the difference absorption of the probe is monitored or in heterodyne detection [30,90]. Using phase-sensitive detection, it becomes possible to probe separately the real and the imaginary parts of the Fourier transform of $P(t)$, $P(\omega)$ [90]. When the signal is generated in another direction, the signal will be proportional to $|P(t)|^2$ in an ideal impulsive experiment or to $|P(\omega)|^2$ in an ideal frequency domain experiment.

We consider weak-field spectroscopy here, where the magnitude of $E(t)$ is sufficiently small that an expansion of $P(t)$ in powers of $E(t)$ converges (or at least gives a good asymptotic approximation [91]). Writing $E(t) = \zeta E(t)$, where $\zeta = 1$ is a formal ordering parameter, we have [92]:

$$P(t) = \sum_{n=1} \zeta^n P^{(n)}(t). \tag{2.5}$$

Linear spectroscopy (ordinary absorption) measures $P^{(1)}(t)$, whereas nonlinear spectroscopy measures higher-order components of the polarization. For a homogeneous and isotropic medium, $P^{(2)}$ vanishes. Therefore $P^{(3)}$ is often the lowest-order nonlinear polarization. Expanding Eq. (2.3) in powers of ζ yields [31,45]

$$P^{(1)}(\mathbf{r}, t) = \int_0^\infty dt_1 \, \hat{S}^{(1)}(t_1) E(\mathbf{r}, t - t_1) , \tag{2.6a}$$

$$\hat{S}^{(1)}(t) \equiv -2 \operatorname{Im} J(t_1) , \tag{2.6b}$$

$$J(t_1) = \operatorname{Tr}[e^{iH_g t_1} e^{-iH_e t_1} \hat{\rho}_g] , \tag{2.6c}$$

where Im denotes the imaginary part. Similarly, we find for the nonlinear polarization that

$$P^{(3)}(\mathbf{r}, t) = \int_0^\infty dt_1 \int_0^\infty dt_2 \int_0^\infty dt_3 \, \hat{S}^{(3)}(t_3, t_2, t_1) E(\mathbf{r}, t - t_3) \times E(\mathbf{r}, t - t_3 - t_2) E(\mathbf{r}, t - t_3 - t_2 - t_1) , \tag{2.7a}$$

$$\hat{S}^{(3)}(t_3, t_2, t_1) \equiv -2 \operatorname{Im} \sum_{\alpha=1}^{4} R_\alpha(t_3, t_2, t_1) , \tag{2.7b}$$

where

$$R_1(t_3, t_2, t_1) = \operatorname{Tr}[e^{iH_e(t_1+t_2+t_3)} e^{-iH_g t_3} e^{-iH_e t_2} e^{-iH_g t_1} \hat{\rho}_g] , \tag{2.8a}$$

$$R_2(t_3, t_2, t_1) = \operatorname{Tr}[e^{iH_g t_1} e^{iH_e(t_2+t_3)} e^{-iH_g t_3} e^{-iH_e(t_1+t_2)} \hat{\rho}_g] , \tag{2.8b}$$

$$R_3(t_3, t_2, t_1) = \operatorname{Tr}[e^{iH_g(t_1+t_2)} e^{iH_e t_3} e^{-iH_g(t_2+t_3)} e^{-iH_e t_1} \hat{\rho}_g] , \tag{2.8c}$$

$$R_4(t_3, t_2, t_1) = \operatorname{Tr}[e^{iH_e t_1} e^{iH_g t_2} e^{iH_e t_3} e^{-iH_g(t_1+t_2+t_3)} \hat{\rho}_g] . \tag{2.8d}$$

$\hat{S}^{(1)}(t_1)$ is called the *linear response function*, and $\hat{S}^{(3)}(t_3, t_2, t_1)$ is called the *nonlinear response function*. The $\mathbf{r}$ dependence of E and P causes *phase matching* [29,30,92]. There are three interactions with E contributing to $P^{(3)}$. In principle, each interaction can be with a distinct laser. If laser fields E_1, E_2, and E_3 having wavevectors k_1, k_2, and k_3 interact with the sample, then phase matching causes the generated light to have any of the wavevectors $\pm k_1 \pm k_2 \pm k_3$.

It is also possible to express the response functions in an alternative form, using *Liouville space* [54,93–97] Green functions. To this end we

define the Liouville space propagator G_{nm} through its action on a nuclear operator A:

$$G_{nm}(t)A \equiv \exp(-iH_n t)A\exp(+iH_m t)\,, \qquad n, m = g, e\,. \tag{2.9}$$

Using Eqs. (2.9) and (2.3) we get

$$J(t_1) = \mathrm{Tr}[G_{eg}(t_1)\hat{\rho}_g]\,, \tag{2.10}$$

and

$$R_1(t_3, t_2, t_1) = \mathrm{Tr}[G_{ge}(t_3)G_{ee}(t_2)G_{ge}(t_1)\hat{\rho}_g]\,, \tag{2.11a}$$

$$R_2(t_3, t_2, t_1) = \mathrm{Tr}[G_{ge}(t_3)G_{ee}(t_2)G_{eg}(t_1)\hat{\rho}_g]\,, \tag{2.11b}$$

$$R_3(t_3, t_2, t_1) = \mathrm{Tr}[G_{ge}(t_3)G_{gg}(t_2)G_{eg}(t_1)\hat{\rho}_g]\,, \tag{2.11c}$$

$$R_4(t_3, t_2, t_1) = \mathrm{Tr}[G_{ge}(t_3)G_{gg}(t_2)G_{ge}(t_1)\hat{\rho}_g]\,. \tag{2.11d}$$

Using the Liouville form, we may give $P^{(3)}$ the following interpretation: The first interaction with E sets up an optical coherence in the sample. $G_{eg}(t_1)$ [or $G_{ge}(t_1)$] represents the evolution and dephasing of this coherence. The second interaction converts the optical coherence into either a population on the ground electronic state ($|g\rangle$) or a population on the excited electronic state ($|e\rangle$). The solvent relaxes toward thermal equilibrium during the time t_2 between the second and third interaction, and its evolution is given by $G_{ee}(t_2)$ or $G_{gg}(t_2)$. The third interaction converts the population back into a coherence, whose time evolution until the detection time is given by $G_{eg}(t_3)$ or $G_{ge}(t_3)$. These are Liouville space pathways where we follow simultaneously the evolution of the bra and the ket.

Considering the difference between the two forms is an instructive example of the utility of the Liouville space formulation. Although Eqs. (2.8a)–(2.8d) are not significantly more complicated than Eqs. (2.11a)–(2.11d), in the former the physical picture of coherence versus population dynamics is lost in the scrambling of the time arguments. The concepts of coherence and dephasing are essential in understanding condensed-phase spectroscopy; the fact that the Liouville space formulation brings these features of the formulas to the forefront is a compelling reason for its use. Throughout this chapter we shall use the Liouville space formulation.

The singularity of electronic correlation functions as $\hbar \to 0$ is apparent using Eqs. (2.9) by noting that each $\exp(-iH_j t)$ factor is actually

$\exp[-(i/\hbar)H_j t]$, where $j = g, e$ (we set $\hbar = 1$ for brevity). For $G_{nm}(t)$ with $n = m$, the singularity of the bra and the ket evolution cancels as $\hbar \to 0$, resulting in classical propagation [98]. However, for $n \neq m$, the dependence on $\hbar$ does not have a classical limit in a strict mathematical sense. Nevertheless, we will demonstrate that by defining a harmonic reference system it is still possible to construct useful semiclassical approximations.

The experimental signal for various techniques can be readily expressed in terms of $P^{(1)}(\mathbf{r}, t)$ and $P^{(3)}(\mathbf{r}, t)$. We give three examples here. For linear absorption, we have

$$I(\omega) = \frac{1}{\pi} \operatorname{Re} \int_0^\infty dt\, e^{i\omega t} J(t)\,, \tag{2.12}$$

where $I(\omega)$ is the normalized electronic absorption lineshape. The generated field intensity in a four-wave mixing experiment when the signal appears in a new direction [e.g., photon echo, transient grating, and coherent anti-stones raman spectroscopy (CARS)] is

$$S(t) = |P^{(3)}(t)|^2\,. \tag{2.13}$$

For pump–probe spectroscopy with an ultrafast probe and spectrally dispersed detection at frequency ω we have [89]

$$S_{PP}(\omega, \tau) \propto \frac{1}{\pi} \operatorname{Im} \int_0^\infty P^{(3)}(t) e^{-i\omega t}\, dt\,. \tag{2.14}$$

C. Simulation of Condensed-Phase Electronic Spectroscopy

In this section we survey simulation methods for optical measurements in the condensed phase. We focus on phase averaging and the inhomogeneous cumulant expansion, which we feel are the most useful currently available techniques. These methods allow an arbitrary inhomogeneous distribution of transition frequencies $[W(\omega_{eg})]$, while also treating the response of the solvent to the chromophore.

Before discussing methods, let us establish some notation. The following definitions are used for averages throughout this chapter:

$$\langle A(\Gamma) \rangle \equiv \int d\Gamma\, A(\Gamma) \rho_g(\Gamma)\,, \tag{2.15a}$$

$$\langle A \rangle_{t_a} \equiv \frac{1}{t_a} \int_0^{t_a} dt\, A[\Gamma_0(t)]\,, \tag{2.15b}$$

$$\langle A \rangle_\infty \equiv \lim_{t_a \to \infty} \langle A \rangle_{t_a} , \tag{2.15c}$$

$$\Gamma \equiv (\mathbf{Q}, \mathbf{P}) , \tag{2.15d}$$

where $\rho_g(\Gamma) \equiv e^{-H_g(\Gamma)/k_B T}$, A is an arbitrary classical function, and $[\mathbf{Q}_0(t), \mathbf{P}_0(t)]$ is the initial phase-space point Γ_0 propagated for a time t by classical mechanics. Equation (2.15a) is a thermal classical expectation value, Eq. (2.15b) is a finite-time microcanonical average, and Eq. (2.15c) is a microcanonical average. For an improved semiclassical approximation, $\rho_g(\Gamma)$ may be replaced by the Wigner function of $e^{-H_g/k_B T}$ [98].

1. *Inhomogeneous Cumulant Expansion*

In the inhomogeneous cumulant expansion, an inhomogeneous distribution is added to the cumulant expansion for spectroscopic lineshapes [41,96,100]. The inhomogeneous distribution is labeled by the parameter Γ. In other words, the phase space of the solvent–solute system is divided into noninterconverting regions, with the region labeled by Γ. Many different physical situations could be described by a distribution of Γ: For instance, Γ could label various noninterconverting potential wells. The motivation for introducing phase-space regions is that effects due to an inhomogeneous distribution can be treated exactly. As a simple example, the inhomogeneous cumulant distribution can reproduce an arbitrary distribution of transition frequencies $W(\omega_{eg})$, while the ordinary cumulant expansion assumes that $W(\omega_{eg})$ is a Gaussian.

Within the cumulant expansion, all optical quantities can be expressed in terms of the quantum autocorrelation function

$$C(t;\Gamma) \equiv \mathrm{Tr}_\Gamma[e^{iH_g t} U e^{-iH_g t} U \hat{\rho}_g] - \mathrm{Tr}_\Gamma[U\hat{\rho}_g]^2 , \tag{2.16}$$

where

$$U \equiv V_e - V_g + \omega_{eg}^0 \tag{2.17}$$

and

$$\omega_{eg} \equiv \langle U \rangle . \tag{2.18}$$

$U(\Gamma)$ is called the *energy gap*. ω_{eg} is the first moment of the absorption spectrum. Tr_Γ is defined as a trace restricted to the (quantum [101]) phase-space region Γ.

The linear and nonlinear response functions can be expressed in terms of the function $g(t;\Gamma)$ [100]:

$$g(t;\Gamma) = i\,\mathrm{Tr}_\Gamma[U\hat{\rho}_g]t + \int_0^t dt' \int_0^{t'} dt''\, C(t'';\Gamma)\,. \tag{2.19}$$

For linear spectroscopy we have

$$J(t) = \int d\Gamma\, W(\Gamma)\exp[-g(t;\Gamma)]\,, \tag{2.20}$$

while for nonlinear spectroscopy we have

$$R_1(t_3,t_2,t_1) = \int d\Gamma\, W(\Gamma)\exp[-g(t_3;\Gamma) - g^*(t_1;\Gamma) - f_+^*(t_3,t_2,t_1;\Gamma)]\,, \tag{2.21a}$$

$$R_2(t_3,t_2,t_1) = \int d\Gamma\, W(\Gamma)\exp[-g(t_3;\Gamma) - g(t_1;\Gamma) + f_+(t_3,t_2,t_1;\Gamma)]\,, \tag{2.21b}$$

$$R_3(t_3,t_2,t_1) = \int d\Gamma\, W(\Gamma)\exp[-g^*(t_3;\Gamma) - g(t_1;\Gamma) + f_-(t_3,t_2,t_1;\Gamma)]\,, \tag{2.21c}$$

$$R_4(t_3,t_2,t_1) = \int d\Gamma\, W(\Gamma)\exp[-g^*(t_3;\Gamma) - g^*(t_1;\Gamma) - f_-^*(t_3,t_2,t_1;\Gamma)]\,, \tag{2.21d}$$

where

$$f_-(t_3,t_2,t_1;\Gamma) = g(t_2;\Gamma) - g(t_2+t_3;\Gamma) - g(t_1+t_2;\Gamma) + g(t_1+t_2+t_3;\Gamma)\,, \tag{2.22a}$$

$$f_+(t_3,t_2,t_1;\Gamma) = g^*(t_2;\Gamma) - g^*(t_2+t_3;\Gamma) - g(t_1+t_2;\Gamma) + g(t_1+t_2+t_3;\Gamma)\,, \tag{2.22b}$$

and $W(\Gamma) \equiv \mathrm{Tr}_\Gamma[\hat{\rho}_g]$.

In applying the inhomogeneous cumulant expansion to a realistic problem we must do two things: First, phase space must be partitioned into noninterconverting (or very slowly interconverting) regions, and second, we must calculate the quantum autocorrelation function $C(t)$ within each region. Let us defer the discussion of how to divide phase space into regions until later and concentrate on the calculation of $C(t)$.

$C(t)$ cannot be evaluated analytically for many-body problems with realistic potentials. Instead, we can calculate $C(t)$ classically. $C(t)$ is complex and satisfies $C(-t) = C^*(t)$. In contrast, classical correlation functions are real and symmetric: $C(-t) = C(t)$. It is therefore preferable to obtain a classical approximation to the symmetrized correlation function

$$C_s(t) \equiv \tfrac{1}{2}[C(t) + C(-t)] , \tag{2.23}$$

which is also real and symmetric. $C(t)$ can be obtained from $C_s(t)$ by using the fluctuation–dissipation theorem [41,65]:

$$C(\omega) = [1 + \tanh(\omega/2k_B T)]C_s(\omega) . \tag{2.24}$$

Here we have defined the Fourier transform by

$$A(\omega) = \frac{1}{2\pi}\int_{-\infty}^{\infty} dt\, e^{i\omega t}A(t) , \tag{2.25a}$$

$$A(t) = \int_{-\infty}^{\infty} d\omega\, e^{-i\omega t}A(\omega) . \tag{2.25b}$$

Note that $C_s(-\omega) = C_s(\omega)$.

Let us introduce the classical correlation function:

$$C_c(t) \equiv \int_\Gamma d\mathbf{Q}\, d\mathbf{P}\, U(\mathbf{Q}[t])U(\mathbf{Q})\rho_g(\mathbf{Q},\mathbf{P}) , \tag{2.26a}$$

$$\rho_g(\mathbf{Q},\mathbf{P}) \equiv e^{-H_g(\mathbf{Q},\mathbf{P})/k_B T} / \int d\mathbf{Q}\, d\mathbf{P}\, e^{-H_g(\mathbf{Q},\mathbf{P})/k_B T} , \tag{2.26b}$$

where ρ_g is the classical density matrix in the ground state, and H_g is the classical ground-state Hamiltonian. $Q[t]$ is the coordinate of the phase point $(\mathbf{Q},\mathbf{P})$ propagated forward classically for a time t. The notation $\int_\Gamma$ refers to an integral over the phase-space region Γ. Then the following relation holds:

$$C_s(\omega) \approx \frac{(\bar{n}(|\omega|) + \frac{1}{2})|\omega|}{k_B T} C_c(\omega) . \tag{2.27}$$

Equation (2.27) is derived by invoking a *displaced harmonic reference system* (see Appendix C). $C(\omega) \approx C_c(\omega)$ if $\omega \ll k_B T$, as one would expect.

A convenient and numerically efficient method for evaluating the correlation function is to use the Wiener–Khinchine theorem [102,103],

which was first proposed by Einstein [104]. We calculate the Fourier transform of $U(t)$, $U(\omega)$, and then

$$C_c(\omega) = |U(\omega)|^2 . \tag{2.28}$$

We now turn to the problem of dividing phase space into regions. There is no simple solution to the problem applicable to all situations. We suggest a simple method of dividing phase space that is reasonable for large systems. Namely, we let a "region" be comprised of (a) an initial condition $(\mathbf{Q}, \mathbf{P})$ and (b) the trajectory generated from that initial condition for a time period t_a. This has the effect of turning the canonical average over phase-space regions in Eq. (2.26a) into finite-time microcanonical averages [see Eq. (2.15b)]. t_a should be chosen short compared to any barrier crossing times, so that the motion of most trajectories will be confined to a single potential well. t_a should also be chosen to be long compared to a typical vibrational period within a well. If the barrier crossing is too rapid to meet these requirements, the potential wells should not be treated as producing an "inhomogeneous distribution"; that is, Γ should span rapidly interconverting potential wells, but not slowly interconverting potential wells.

To summarize the conclusions of this section, we give a specific procedure for calculating optical lineshapes via the inhomogeneous cumulant expansion:

1. Generate initial conditions $(\mathbf{Q}, \mathbf{P})$ from the classical Boltzmann distribution. This can be done through a variety of methods (e.g., molecular dynamics equilibration or Monte Carlo equilibration).
2. Determine an averaging time t_a that meets the requirements discussed above by running test trajectories.
3. Run trajectories from the initial conditions. For each trajectory do the following:
4. Calculate $U(t)$ along each trajectory.
5. Calculate $C_c(\omega)$ [Eq. (2.28)], and then find $C_s(\omega)$ [Eq. (2.27)] and $C(\omega)$ [Eq. (2.24)].
6. Take the inverse Fourier transform of $C(\omega)$. Use Eq. (2.19) to find $g(t)$ by numerical integration.
7. Apply Eqs. (2.20) and (2.21a)–(2.21d) to find the trajectory's contribution to the desired optical response function.
8. Repeat for many independent trajectories until satisfactory convergence is reached.

A possible alternative to the method described here is to include zero-point energy directly into the trajectories themselves. This can be done by defining

$$C_c'(t) \equiv \int_\Gamma d\mathbf{Q}\, d\mathbf{P}\, U(\mathbf{Q}[t])U(\mathbf{Q})\rho_g'(\mathbf{Q},\mathbf{P})\,, \tag{2.29}$$

where $\rho_g'(\mathbf{Q},\mathbf{P})$ is the Wigner function of H_g, and $\mathbf{Q}[t]$ is propagated classically on the ground-state Hamiltonian. We then have

$$C_s(\omega) \approx C_c'(\omega)\,. \tag{2.30}$$

Equations (2.30) and (2.27) are exact when applied to a displaced harmonic system, but yield distinct approximations when applied to realistic potentials. There are no practical methods for calculating the Wigner function ρ' other than a local harmonic expansion of the potential energy surface. This is not appropriate for systems undergoing large-amplitude motion. Equation (2.27) avoids the many problems that can be encountered when including zero-point energy in classical simulations [105–107], but relies on an approximate correction factor for the inclusion of zero-point energy into lineshapes. Equation (2.30) assumes that zero-point energy can be included into the classical trajectories without introducing unphysical effects related to energy transfer among modes [107].

2. *Phase Averaging*

The phase-averaging approach is a microscopic classical approximation for $P^{(3)}$ [108–110]. The only approximation in its derivation is the classical limit: Quantum population dynamics on the $|e\rangle$ and $|g\rangle$ surfaces are replaced by classical dynamics, and time-ordered exponentials are replaced by ordinary exponentials. We introduce two trajectories: $\mathbf{Q}_1(t)$ and $\mathbf{Q}_2(t)$. Each trajectory begins from the same initial condition $(\mathbf{Q},\mathbf{P})$ when $t=0$. $\mathbf{Q}_1(t)$ is the coordinate of the initial condition propagated with H_g. The other trajectory $\mathbf{Q}_2(t)$ is run on the ground state for the t_1 period and on the excited state for the t_2 and t_3 periods. Associated with $\mathbf{Q}_1(t)$ and $\mathbf{Q}_2(t)$ are the energy gap functions:

$$U_j(t) = U[\mathbf{Q}_j(t;\mathbf{Q},\mathbf{P})]\,, \qquad j=1,2\,. \tag{2.31}$$

In terms of these quantities, the phase-averaging approach yields

$$J(t) = \left\langle \exp\left[-i \int_0^t U_1(t')\, dt' \right] \right\rangle , \tag{2.32}$$

whereas for nonlinear spectroscopy, phase averaging gives

$$R_1(t_3, t_2, t_1) = \left\langle \exp\left[i \int_{t_2+t_1}^{t_1+t_2+t_3} U_2(t')\, dt' \right] \exp\left[i \int_0^{t_1} U_2(t')\, dt' \right] \right\rangle , \tag{2.33a}$$

$$R_2(t_3, t_2, t_1) = \left\langle \exp\left[i \int_{t_1+t_2}^{t_1+t_2+t_3} U_2(t')\, dt' \right] \exp\left[-i \int_0^{t_1} U_2(t')\, dt' \right] \right\rangle , \tag{2.33b}$$

$$R_3(t_3, t_2, t_1) = \left\langle \exp\left[i \int_{t_1+t_2}^{t_1+t_2+t_3} U_1(t')\, dt' \right] \exp\left[-i \int_0^{t_1} U_1(t')\, dt' \right] \right\rangle , \tag{2.33c}$$

$$R_4(t_3, t_2, t_1) = \left\langle \exp\left[i \int_{t_1+t_2}^{t_1+t_2+t_3} U_1(t')\, dt' \right] \exp\left[i \int_0^{t_1} U_1(t')\, dt' \right] \right\rangle . \tag{2.33d}$$

Here $\langle \cdots \rangle$ is defined in Eq. (2.15a). The initial conditions $(\mathbf{Q}, \mathbf{P})$ can be generated either from separate Monte Carlo equilibrations or from samples along a single base trajectory. In the calculations that follow, we use the base trajectory approach to find initial conditions.

The *static limit of spectroscopy* occurs when the timescale of molecular motion is slow compared to the inverse absorption linewidth. Equations (2.33a)–(2.33d) are exact in the static limit. They are also exact when V_g and V_e are displaced harmonic potential surfaces in the limit $k_B T \gg \omega$. In the static solvent limit, the phase factors in Eqs. (2.32) and (2.33a)–(2.33d) simplify, yielding [111]

$$J(t) = \langle \exp(-itU) \rangle , \tag{2.34a}$$

$$R_1(t_3, t_2, t_1) = \langle \exp[it_3 U_2(t_2)] \exp[it_1 U_2(0)] \rangle , \tag{2.34b}$$

$$R_2(t_3, t_2, t_1) = \langle \exp[it_3 U_2(t_2)] \exp[-it_1 U_2(0)] \rangle , \tag{2.34c}$$

$$R_3(t_3, t_2, t_1) = \langle \exp[it_3 U_1(t_2)] \exp[-it_1 U_1(0)] \rangle , \tag{2.34d}$$

$$R_4(t_3, t_2, t_1) = \langle \exp[it_3 U_1(t_2)] \exp[it_1 U_1(0)] \rangle . \tag{2.34e}$$

In this limit the solvent does not move when the system is in an electronic coherence (i.e., the t_1 and the t_3 periods). During t_2 it can move, resulting in spectral diffusion (see below).

We have implemented the phase-averaging approach as follows:

1. Determine the maximum time intervals $t_1^{(m)}$, $t_2^{(m)}$, and $t_3^{(m)}$ desired. This requires a rough knowledge of absorption linewidths (t_1, t_3) as well as the duration of the experiment.
2. Determine whether $U_2(t)$ is required. This depends on the desired spectroscopic technique.
3. Equilibrate the sample, and generate initial conditions. For an ergodic system, initial conditions can be generated at intervals along a "base" trajectory $[\Gamma_g(t)]$. Otherwise, separate equilibrations will be required. We will use the base trajectory approach here.
4. At time intervals t_j, run excited-state trajectories starting from initial conditions along $\Gamma_g(t)$. This is only necessary to find $U_2(t)$. The result is a family of trajectories $\Gamma_e(t, i)$, where $i = 0, 1, 2, \ldots$ and $\Gamma_e(0, i) = \Gamma_g(i * t_j)$. The excited-state trajectories $\Gamma_e(t, i)$ should be run for a time equal to $t_2^{(m)} + t_3^{(m)}$. The purpose of this scheme is to avoid running new trajectories for each value of t_1, t_2, and t_3. t_j should be chosen long enough so that successive excited-state trajectories are not strongly correlated.
5. Evaluate U along $\Gamma_e(t, i)$ and $\Gamma_g(t)$. We call the resulting functions $U_e(t, i)$ and $U_g(t)$.
6. For each desired $t_1 \le t_1^{(m)}$, $t_2 \le t_2^{(m)}$, and $t_3 \le t_3^{(m)}$, we make the identification:

$$U_1^{(i)}(t) = U_g(t + it_j)\,,$$
$$U_2^{(i)}(t) = U_g(t + it_j - t_1) \qquad (t \le t_1)\,,$$
$$U_2^{(i)}(t) = U_e(i, t - t_1) \qquad (t > t_1)\,.$$

   Here, $U_1^{(i)}$ is the ith sample for U_1, and $U_2^{(i)}$ is the ith sample for U_2.
7. Given $U_1^{(i)}$ and $U_2^{(i)}$, calculate the response functions using Eqs. (2.32) and (2.33a)–(2.33d). The evaluation of the integrals can be greatly accelerated by calculating the difference between the previous t_1, t_2, and t_3 values. Repeat for all the samples i.

It is possible to map phase averaging onto the cumulant approximation. This may be done as follows: Given $J(t)$ calculated from the

phase-averaging technique, the logarithm is taken. This defines an effective $g(t)$:

$$g_{\text{eff}}(t) \equiv -\ln J_P(t)\,, \tag{2.35}$$

where $J_P(t)$ is the approximation to $J(t)$ calculated by phase averaging. $g_{\text{eff}}(t)$ then defines an effective $C_c(t)$ through

$$C_{c\,\text{eff}}(t) \equiv \frac{d^2}{dt^2}\, g_{\text{eff}}(t)\,. \tag{2.36}$$

Equation (2.30) or (2.27) can then be used to calculate a quantum $C(t)$, and then a quantum $g(t)$ can be found. This procedure makes phase averaging exact for a displaced harmonic oscillator system, but destroys the exactness of phase averaging for a jump model (see Section II.E). We feel that it is best to use phase averaging without invoking g_{eff}, or use the cumulant technique directly. The cumulant method should be used when spectral asymmetry due to vibrational quantization is an important effect. Phase averaging should be used when spectral asymmetry due to differing potential shape or excited-state dynamics are important.

D. Exactly Solvable Models for the Optical Response

Exactly solvable models provide useful insight. They can also be used to interpret the results of simulation by mapping the simulation onto one or a combination of these models.

1. *The Multimode Brownian Oscillator Model*

The first model problem that we will study is the linearly displaced harmonic oscillator. This system has the potential energy surfaces [32,44,45].

$$V_g = \sum_j \frac{\omega_j}{2}\,(p_j^2 + q_j^2)\,, \tag{2.37a}$$

$$V_e = \omega_{eg} + \sum_j \frac{\omega_j}{2}\,(p_j^2 + q_j^2 + 2q_j d_j)\,. \tag{2.37b}$$

In addition, the oscillator is coupled to a bath by the Langevin equation [112]:

$$\ddot{q}_j + \omega_j^2 q_j + \gamma_j \dot{q}_j = f_j(t)\,, \tag{2.38}$$

where ground-state evolution is assumed, and $f_j(t)$ is the random force.

The Langevin equation assumes that $f_j(t)$ is a Gaussian random process which satisfies

$$\langle f_j(t) f_j(0) \rangle = 2k_B T \gamma_j \delta(t) . \tag{2.39}$$

Thus, each oscillator is characterized by a frequency ω_i and a damping γ_i. The ground state of the oscillator is displaced by d_i from the excited state of the oscillator, leading to

$$U = \sum_{i=1}^{M} \omega_i d_i q_i . \tag{2.40}$$

Using Eqs. (2.40) and (2.38) we get

$$C_s(t) = \sum_j \Delta_j^2 M_j(t) , \tag{2.41}$$

where

$$M_i(t) \equiv \mathrm{Re} \langle q_i(t) q_i(0) \rangle / \langle q_i^2 \rangle , \tag{2.42}$$

$$\Delta_i^2 \equiv (\bar{n}_i + \tfrac{1}{2}) d_i^2 \omega_i^2 , \tag{2.43}$$

$$\Delta \equiv (\langle U^2 \rangle - \langle U \rangle^2)^{1/2} = \left(\sum_i \Delta_i^2 \right)^{1/2} . \tag{2.44}$$

Δ_i^2 is the magnitude of the fluctuation of oscillator i. Using the Langevin equation, $M_i(t)$ satisfies the following equation of motion:

$$\frac{d^2}{dt^2} M_i(t) + \gamma_i \frac{d}{dt} M_i(t) + \omega_i^2 M_i(t) = 0 . \tag{2.45}$$

This gives the following correlation function of U:

$$C_s(\omega) = \frac{1}{2\pi} \sum_{i=1}^{M} \Delta_i^2 \left[\frac{\omega_i^2 \gamma_i}{(\omega_i^2 - \omega^2)^2 + \omega^2 \gamma^2} \right] . \tag{2.46}$$

Here we have associated the classical correlation function with the symmetrical part of the quantum correlation function. Other choices are also possible [99,113,114]. $C_c(\omega)$ has the same functional form as $C_s(\omega)$, except that

$$\Delta_i^2 = k_B T \omega_i d_i^2 . \tag{2.47}$$

This result can be easily extended to incorporate inhomogeneous broadening. We assume that the oscillator parameters carry a dependence on initial condition:

$$\omega_i = \omega_i(\Gamma)\,, \tag{2.48a}$$

$$\gamma_i = \gamma_i(\Gamma)\,, \tag{2.48b}$$

$$\Delta_i = \Delta_i(\Gamma)\,, \tag{2.48c}$$

$$\omega_{eg} = \omega_{eg}(\Gamma)\,. \tag{2.48d}$$

The linear response function thus becomes

$$J(t_1) = \int d\boldsymbol{\omega}\, d\boldsymbol{\gamma}\, d\boldsymbol{\Delta}\, d\boldsymbol{\omega}_{eg} W(\boldsymbol{\omega}, \boldsymbol{\gamma}, \boldsymbol{\Delta}, \boldsymbol{\omega}_{eg}) J(t_1; \boldsymbol{\omega}, \boldsymbol{\gamma}, \boldsymbol{\Delta}, \boldsymbol{\omega}_{eg})\,. \tag{2.49}$$

The response functions $R_i(t_3, t_2, t_1)$ have the form

$$R_i(t_3, t_2, t_1) = \int d\boldsymbol{\omega}\, d\boldsymbol{\gamma}\, d\boldsymbol{\Delta}\, d\boldsymbol{\omega}_{eg} W(\boldsymbol{\omega}, \boldsymbol{\gamma}, \boldsymbol{\Delta}, \boldsymbol{\omega}_{eg}) R_i(t_3, t_2, t_1; \boldsymbol{\omega}, \boldsymbol{\gamma}, \boldsymbol{\Delta}, \boldsymbol{\omega}_{eg})\,. \tag{2.50}$$

Here, the boldface quantities refer to all M oscillators; for example, $\boldsymbol{\omega} \equiv (\omega_1 \cdots \omega_M)$. $W(\boldsymbol{\omega}, \boldsymbol{\gamma}, \boldsymbol{\Delta}, \boldsymbol{\omega}_{eg})$ is the density of oscillators having parameters $\boldsymbol{\omega}, \boldsymbol{\gamma}, \boldsymbol{\Delta}, \boldsymbol{\omega}_{eg}$; and $R_i(t_3, t_2, t_1; \boldsymbol{\omega}, \boldsymbol{\gamma}, \boldsymbol{\Delta}, \boldsymbol{\omega}_{eg})$ is the response function for a given set of oscillator parameters. Inhomogeneous broadening is commonly introduced by assuming a distribution of the electronic transition frequencies $W(\omega_{eg})$. The inhomogeneous distribution of oscillators introduced here provides a more general line-broadening mechanism. In the present formulation the transition frequency ω_{eg} can be correlated with the underlying nuclear dynamics. The conventional use of $W(\omega_{eg})$ assumes that the transition frequency is uncorrelated with the nuclear dynamics.

2. *Stochastic Models*

In stochastic models, the transition frequency ω_{eg} is assumed to be a stochastic variable. The essential approximation in stochastic models is that the bath affects the chromophore, but the chromophore does not affect the bath. Consequently, effects such as the Stokes shift are missed [111]. The two most commonly used stochastic models are a Gauss–Markov process and a two-state jump process [59]. For linear absorption, we have

$$J(t) = \left\langle \exp\left(-i \int_0^t \omega_{eg}(t')\, dt'\right)\right\rangle_\infty , \tag{2.51}$$

where $\langle \cdots \rangle_\infty$ is defined in Eq. (2.15c). Expressions for R were given by Mukamel and Loring [54,100].

3. *The Optical Bloch Equations*

The optical Bloch equations describe a two-level system interacting with an electric field and a bath. In the rotating wave approximation we have [29,115]

$$\frac{d\hat{\rho}_{ee}}{dt} = -\tfrac{1}{2} iV^* \hat{\rho}_{ge} + \tfrac{1}{2} iV\hat{\rho}_{eg} - (1/T_1)\hat{\rho}_{ee} \tag{2.52a}$$

$$\frac{d\hat{\rho}_{eg}}{dt} = \tfrac{1}{2} iV(\hat{\rho}_{gg} - \hat{\rho}_{ee}) + [i(\omega_{eg} - \omega) - (1/T_2)]\hat{\rho}_{ge} , \tag{2.52b}$$

where $\hat{\rho}$ is the density matrix of the two-level system, $\hat{\rho}_{nm}$ is the nm matrix element of the density matrix, and $V \equiv E \cdot \mu_{eg}$. We also have

$$P(t) = \mu_{eg}\hat{\rho}_{ge}(t) + \mu_{ge}\hat{\rho}_{eg}(t) , \tag{2.53a}$$

$$J(t) = \exp(-i\omega_{eg}^0 t - t/T_2) . \tag{2.53b}$$

$R(t_3, t_2, t_1)$ was given by Mukamel and Loring [54]. The Bloch equations predict a Lorentzian absorption lineshape. This Lorentzian is often convoluted with a static distribution of transition frequencies $W(\omega_{eg})$. T_1 is the population decay time, and represents depletion of the excited state. T_2 is the dephasing time, and represents the effect of nuclear motions in destroying phase coherences. The Bloch equations and the stochastic model applied to a Gaussian random process are special cases of the Brownian oscillator model.

E. Comparison of Simulation Techniques and Models

In this section we compare the simulation methods and the applicability of the models presented above, concentrating on how the methods take into account the physical effects discussed in Section II.A. We first consider the second-order cumulant expansion. This expansion is closely related to the stochastic models. In fact, the stochastic model for a Gaussian random process can be considered a limiting case of the cumulant expansion when $\langle U(t)U(0)\rangle$ is real—that is, when quantum effects are not important. The second-order cumulant expansion predicts a Gaussian $I(\omega)$ in the static limit. Nuclear dynamics are included through

$\langle U(t)U(0)\rangle$. The dynamics can be either oscillatory or overdamped. Spectral diffusion processes are included, and the system can have an arbitrary distribution of timescales. Quantum effects are included through the complex-valued nature of the autocorrelation of U and through the possibility of including zero-point motion in the dynamics. The second-order cumulant expansion can give an asymmetric absorption lineshape. The second-order cumulant expansion implicitly assumes that V_g and V_e have the same shape. A practical consequence of this assumption is that the long-time behavior of the time-resolved Stokes shift (which is governed by V_e) is sometimes poorly predicted.

By including an explicit averaging over an inhomogeneous distribution of ω_{eg}, we can also account for a non-Gaussian $W(\omega_{eg})$. This is essential (for example) when handling a cluster spectra, which are often dominated by an inhomogeneous distribution of a few low-energy isomers. Below, we also show that the inhomogeneous cumulant approximation is appropriate even when there are jump dynamics which are much slower than a typical vibrational period. We have encountered exactly this kind of dynamics in our simulations. The inhomogeneous cumulant expansion fails for jump dynamics which occur on a timescale comparable to a typical vibrational period [116]. Also, the inhomogeneous cumulant expansion fails to take into account differences in the shape of V_g and V_e.

The phase-averaging technique makes the fewest assumptions of any technique discussed so far, since its derivation involves only taking the classical limit. Phase averaging correctly treats jump dynamics regardless of the jumping rate, and also takes into account effects due to differences in potential shape. The one limitation of the phase-averaging technique is that it is purely classical. Thus, asymmetry in the absorption spectrum due to vibrational quantization is left out by the phase-averaging technique. We feel the best strategy is to use the inhomogeneous cumulant approximation for low-temperature spectra ($k_B T \ll \omega$), where anharmonicity effects are small and the effects of vibrational quantization are important. At higher temperatures, phase averaging is most likely to become more accurate as barrier crossing produces jump dynamics.

The static approximation was shown in Section II.C.2 to be a limiting case of phase averaging when τ_r is assumed to be much smaller than a typical timescale of solvent motion. The term "static approximation" is often used in theories of pressure broadening. In small molecule spectroscopy it is often called the *classical Condon approximation*. It is perhaps the oldest semiclassical method of calculating optical lineshapes [117,118]. The static approximation is typically used in the calculation of $I(\omega)$ for pure fluids [119,120]. The static approximation leads to the following approximation for linear absorption:

$$I(\omega) = \langle \delta(\omega + V_g - \omega_{eg}^0 - V_e) \rangle \,. \tag{2.54}$$

Each solvent configuration has its own transition frequency given by the delta function of Eq. (2.54). The static approximation takes into account an arbitrary inhomogeneous distribution of transition frequencies $W(\omega_{eg})$. It neglects nuclear dynamics during the t_1 and t_3 periods. Zero-point motion can be incorporated into the thermal expectation values, but no other quantum effects are included. The static approximation has successfully been used to treat problems as varied as pump–probe photodissociation [108,121] and $I(\omega)$ for a solvated electron in water [122–124]. The neglect of nuclear dynamics, however, is a nontrivial approximation. If applied to a rare gas cluster such as benzene–Ar, the static approximation can overestimate linewidths by more than a factor of two [57]. Obviously, vibrational structure cannot be reproduced by the classical Condon approximation.

Despite its age, the classical Condon approximation has only recently been applied to nonlinear spectroscopy in a systematic way [111]. Fried and Mukamel [108] have applied the classical Condon approximation [Eqs. (2.34a)–(2.34e)] to the pump–probe photodissociation of ICN [18,121,125–129]. In this treatment, optical transitions are assumed to occur instantaneously, just as they are for linear absorption. Nuclear dynamics occurring while the system is in an electronic population, however, are taken into account. This method gave excellent agreement with a quantum calculation of the ICN photodissociation. Walsh and Loring [109] have recently used the static solvent approximation to calculate the impulsive stimulated scattering signal of a model Lennard-Jones solvent.

We next turn to the discussion of models. The multimode Brownian oscillator model predicts a specific form of the cumulant expansion, where $\langle U(t)U(0) \rangle$ is related to the dynamics of a collection of damped oscillators. It thus has all the properties of the cumulant expansion, and is best regarded as a tool for analyzing spectra in terms of the simple physical picture of a few Brownian oscillators.

We next discuss stochastic models [59]. The best known stochastic model is when $\omega_{eg}(t)$ is taken to be a Gauss–Markov process. Then $\langle \omega_{eg}(t)\omega_{eg}(0) \rangle_\infty$ is an exponential: $\langle \omega_{eg}(t)_{eg}(0) \rangle_\infty = \Delta^2 \exp(-\Lambda t)$. In the limit of slow nuclear dynamics ($\Lambda \ll 1/\tau_r$), this model predicts a Gaussian $I(\omega)$. On the other hand, for fast nuclear dynamics ($\Lambda \gg 1/\tau_r$), the model predicts a Lorentzian spectrum. The result of the Bloch equations applied to a system with a Gaussian $W(\omega_{eg})$ can be recovered from the stochastic model by assuming that $\langle U(t)U(0) \rangle = \Delta_I^2 + \Delta_H^2 \delta(t)$. That is, there is a timescale separation into fast (homogeneous broadening) and slow (inhomogeneous broadening) timescales.

The major advantage of the stochastic models is that they take into account in a simple way many features of nuclear dynamics. $\langle \omega_{eg}(t)\omega_{eg}(0)\rangle_\infty$ can be either overdamped or oscillatory. Also, an arbitrary distribution of system timescales can be taken into account. Quantum effects are missing from stochastic models. At most, one can take into account zero-point motion in the fluctuations of $\langle \omega_{eg}(t)\omega_{eg}(0)\rangle_\infty$. Effects due to potential shape and anharmonicity are also missing from stochastic models.

There is a close relationship between stochastic models and phase averaging. Comparing Eq. (2.32) to Eq. (2.51), we see that the phase-averaging result for $J(t)$ is the same as the stochastic model result for $J(t)$, with the exception that the average used in stochastic models is over time, while the average in Eq. (2.32) is over phase space. When applied to linear absorption, phase averaging can thus be viewed as a microscopic implementation of a stochastic model, where the identification $\omega_{eg}(t) = U(t)$ has been made. In other words, stochastic models implicitly use a microcanonical time average, whereas phase averaging uses a canonical average. For a large ergodic system (such as a liquid) the two approaches give the same result.

Another difference between phase-averaging and stochastic models arises when we consider nonlinear spectroscopy. The stochastic model gives the same result as Eqs. (2.33a)-(2.33d), except that the distinction between nuclear dynamics in the ground and excited electronic state is lost (i.e., U_2 is set equal to U_1). We thus get $R_1 = R_3$ and $R_2 = R_4$. Since the phase-averaging approach uses trajectories that hop from the ground potential energy surface to the excited-state potential energy surface, the chromophore can affect the bath. Phase averaging can be used to model the time-resolved Stokes shift, whereas the stochastic model cannot.

The next model that we will consider is the Bloch equations. The Bloch equations account for nuclear dynamics by the use of a single relaxation timescale, called the *dephasing time*. The dephasing time T_2 builds in the destruction of electronic coherences by fast nuclear dynamics. The Bloch equations also build in a second timescale, called the *population relaxation time* (T_1), that represents the relaxation of the excited-state population. Inhomogeneous effects are included by convoluting the lineshape with $W(\omega_{eg})$. The Bloch equations are most often used as a way of interpreting experimental data. For instance, if we assume that $W(\omega_{eg})$ is a Gaussian, the Bloch equations predict that the linear absorption lineshape $I(\omega)$ is the convolution of a Gaussian with a Lorentzian (the Voigt profile [49]). Deconvolution procedures can then be used to extract the dephasing time. The Bloch equations with a Gaussian $W(\omega_{eg})$ can be derived from the Brownian oscillator model by

assuming that $C_c(\omega) = A\delta(\omega) + B$; that is, only fast (homogeneous broadening) or slow (inhomogeneous broadening) motions exist.

The Bloch equations take into account rapid overdamped nuclear motion during an electronic coherence (the t_1 and t_3 periods). They do not take into account nuclear motion during an electronic population (the t_2 period), and hence they miss effects related to spectral diffusion such as the time-resolved Stokes shift. Since nuclear dynamics are described with a single parameter, a distribution of system timescales is obviously not taken into account. Quantum effects can be introduced only on the level of choosing a $W(\omega_{eg})$ that includes zero-point motion. The Bloch equations do not address effects produced by potential shape or anharmonicity.

Much about the inhomogeneous cumulant approximation and phase averaging can be learned by studying simple model problems. We first consider the undamped displaced harmonic oscillator [see Eq. (2.37b)]. In Appendix B, we show that the ordinary cumulant approximation is exact for this model. Phase averaging is also shown to be exact in the high-temperature limit of this model. Figure 1 compares the results of

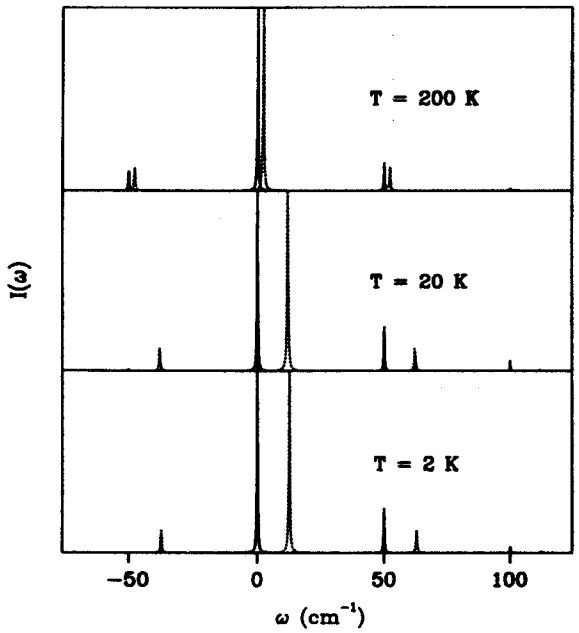

Figure 1. $I(\omega)$ for the displaced harmonic oscillator system described in the text. The solid line is the exact result, while the dotted line is the phase-averaging result. *Top panel:* $T = 200$ K. *Middle panel:* $T = 20$ K. *Bottom panel:* $T = 2$ K.

phase averaging and the exact result of Eq. (B.1a) for a displaced harmonic oscillator system with $\omega_{eg} = 0$, $\omega = 50\,\mathrm{cm}^{-1}$, $\Delta = 25\,\mathrm{cm}^{-1}$, and $T = 2$, 20, and 200 K. When $k_B T \gg \omega$, phase averaging agrees well with the exact result. At low T, the peaks of the phase-averaged result are shifted from those of the exact result. The phase-averaged result and the exact result, however, both have the same first and second moments.

It can be computationally laborious to carry out the averaging over different trajectories in the phase-averaging method. For a large ergodic system, equivalence of ensembles implies that a single trajectory microcanonical average should give the same results as a canonical average. With the cumulant method, a single trajectory run at an energy $E = (\bar{n} + \frac{1}{2})\omega$ will give the exact result for a displaced harmonic oscillator system. With phase averaging (see Appendix B), the optimal energy for a single trajectory is still $E = (\bar{n} + \frac{1}{2})\omega$, but the resulting $I(\omega)$ is not exact for a displaced harmonic oscillator. Figure 2 compares the exact result for a displaced harmonic oscillator ($\omega = 50\,\mathrm{cm}^{-1}$, $\Delta = 25\,\mathrm{cm}^{-1}$, $T = 20$ K) and an optimal single-trajectory phase-averaging calculation.

We next consider the two-state jump model [59]. In this model, $U(t)$ hops between values ω_1 and $-\omega_1$ with a rate $\gamma/2$. Figure 3 shows the results of applying the phase-averaging technique and the stochastic

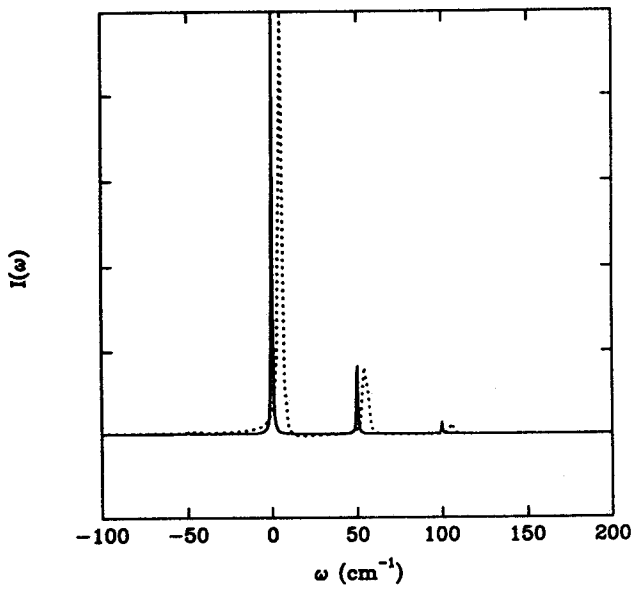

Figure 2. Single-trajectory phase averaging (dotted line) versus the exact $I(\omega)$ (solid line) for the displaced harmonic oscillator system described in the text.

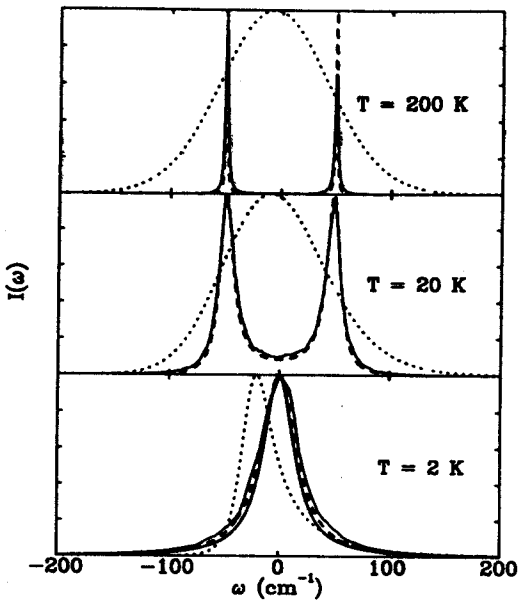

Figure 3. The absorption spectrum of the two-state jump model, for $\omega_1 = 50\,\mathrm{cm}^{-1}$ and $\gamma = 1.45$ (*top panel*), 14.5 (*middle panel*), and 145 (*bottom panel*) cm^{-1}. Dashed line: the exact result of Eq. (B.22). Dotted line: results of the cumulant approximation. Solid line: result of a phase-averaging calculation. In the bottom panel, the dotted line is a cumulant calculation performed at $T = 20\,\mathrm{K}$, and the dot–dash line is a cumulant calculation performed at $T = 2000\,\mathrm{K}$.

model to the two-state jump problem. In these calculations, $\omega_1 = 50\,\mathrm{cm}^{-1}$ and $\gamma = 145$, 14.5, and $1.45\,\mathrm{cm}^{-1}$. Stochastic $U(t)$ values were generated for a period of 950 psec, with a time step of 3.6 psec. The top panel in Fig. 3 has the slowest jump rate ($1.45\,\mathrm{cm}^{-1}$). The cumulant approximation combines the two peaks into a single average peak that is nearly Gaussian. In the bottom panel of Fig. 3, the jump rate has been increased so that the two peaks merge into one. The cumulant approximation agrees well with the exact result of Eq. (B.22), so long as the thermal asymmetrization factor of Eq. (2.30) is not used. In fact, there is no unique application of the cumulant approximation to the jump model, because the jump model can be specified without giving the temperature. In Appendix B, we show that the cumulant approximation correctly predicts the peak of $I(\omega)$ but incorrectly predicts the wings of the spectrum when $\gamma \gg \omega_1$ and $kT \gg \gamma$.

The inhomogeneous cumulant expansion, however, can accurately reproduce the spectrum produced by a slow two-state jump ($\gamma \ll \omega_1$). In Fig. 4, we show the spectrum calculated with the inhomogeneous cumul-

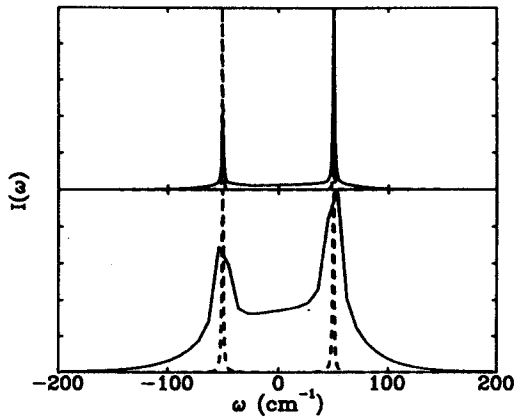

Figure 4. The absorption spectrum of the two-state jump model, for $\omega_1 = 50\,\mathrm{cm}^{-1}$ and $\gamma = 1.45\,\mathrm{cm}^{-1}$ (*bottom panel*) and $0.145\,\mathrm{cm}^{-1}$ (*top panel*). The exact result is shown in dashed lines, while the result of the inhomogeneous cumulant expansion is shown in solid lines.

ant approximation for jump rates of $\gamma = 1.45\,\mathrm{cm}^{-1}$ and $\gamma = 0.145\,\mathrm{cm}^{-1}$. For each value of γ, a trajectory of 950 psec was generated as described above. For the calculation with $\gamma = 1.45\,\mathrm{cm}^{-1}$, the trajectory was divided into 128 equal segments, and the spectrum of each segment was calculated via the inhomogeneous cumulant approximation. For the calculation with $\gamma = 0.145\,\mathrm{cm}^{-1}$, the trajectory was divided into 16 equal segments. The optimal segment length should be of the same order as, but smaller

TABLE I
Summary of the Features of Various Methods and Models for Calculating Spectroscopic Quantities[a]

Method	Arb. $W(\omega_{eg})$	Nuclear Dyn.	Many Timescales	V.Q.	Diff. Shape
Inhomogeneous cumulant	Yes	Yes	Yes	Yes	No
Phase averaging	Yes	Yes	Yes	No	Yes
Static approximation	Yes	No	No	No	Yes
Brownian oscillator	No	Yes	Yes	Yes	No
Stochastic models	No	Yes	Yes	No	No
Bloch equations	Yes	Yes	No	No	No

[a] Each of the features is described in detail in the text. "Arb. $W(\omega_{eg})$" indicates that the method is exact in the static limit, regardless of the form of $W(\omega_{eg})$. "Nuclear Dyn." indicates that the method includes the effects of nuclear dynamics. "Many Timescales" indicates that the method can incorporate a distribution of solvent timescales. "V.Q." indicates that vibrational quantization effects are included. "Diff. Shape" indicates that the method can take into account differences in the shape of V_g and V_e.

than, the inverse jump rate. The spectrum of the slower jump process is accurately reproduced, whereas the inhomogeneous cumulant approximation overestimates the width of the fast jump process. The error in the peak height of the spectrum with $\gamma = 0.145\,\mathrm{cm}^{-1}$ is due to the finite trajectory length. The conclusions of this section are summarized in Table I.

F. Direct Visualization of $R(t_3, t_2, t_1)$

As discussed in Section II.B, the signal of all third-order nonlinear spectroscopies can be related to the response function $R(t_3, t_2, t_1)$. Therefore, understanding the behavior of R directly can lead to a unified picture of many nonlinear spectroscopic techniques. In this subsection we discuss the behavior of R itself for a single Brownian oscillator in three limiting cases [57]. Case I is an underdamped mode, Case II is an overdamped mode in the fast modulation limit, and Case III is an overdamped mode in the slow modulation limit (see Fig. 5). We give the

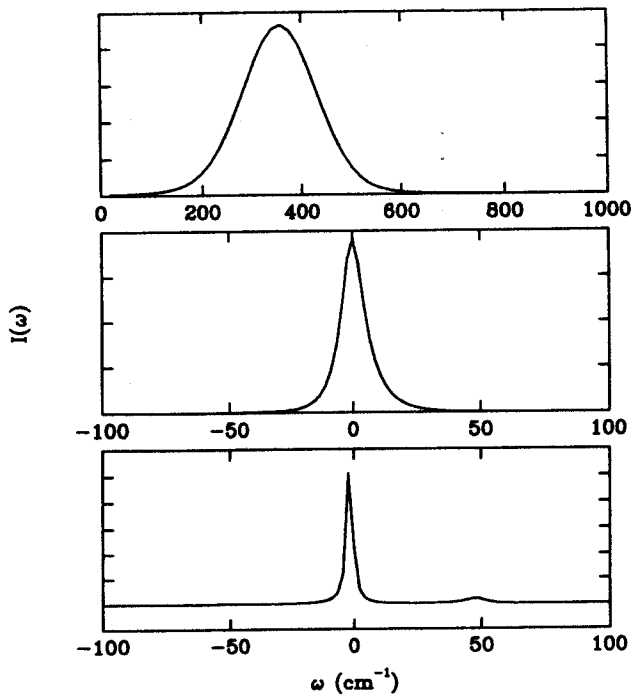

Figure 5. The absorption of the three Brownian oscillator systems described in Table II. *Top:* Overdamped oscillator in the slow modulation limit. *Center:* Overdamped oscillator in the fast modulation limit. *Bottom:* Underdamped oscillator.

most consideration to Case III because its response function shows the richest behavior.

We will consider two- and three-pulse photon echo and pump–probe spectroscopies in the ultrashort pulse limit. The two-pulse photon echo signal S_{PE} is [65]

$$S_{PE}(t_1) = \int_0^\infty dt_3 |R(t_3, 0, t_1)|^2 . \tag{2.55}$$

In photon echo spectroscopy, two pulses are applied with a delay t_1, and the radiation produced in a phase-matched direction is monitored. See Section III.B for a more complete explanation of photon echo spectroscopy. In three-pulse photon echo spectroscopy, the system is probed with three pulses; the delay time between the first and second pulses is t_1, and the delay time between the second and third pulses is t_2. The signal in three-pulse photon echo spectroscopy is

$$S_{3PE}(t_2, t_1) = \int_0^\infty dt_3 |R(t_3, t_2, t_1)|^2 . \tag{2.56}$$

The impulsive pump–probe signal [130] is given by

$$S_{PP}(\omega_3, t_2) = \frac{1}{\pi} \operatorname{Re} \int_0^\infty e^{-i\omega_3 t_3} R(t_3, t_2, t_1 = 0)\, dt_3 . \tag{2.57}$$

For photon echo spectroscopies, $R = R_2 + R_3$, while for impulsive pump–probe spectroscopy it also suffices to calculate just R_2 and R_3, since $R_1(t_3, t_2, t_1 = 0) = R_2(t_3, t_2, t_1 = 0)$ and $R_3(t_3, t_2, t_1 = 0) = R_4(t_3, t_2, t_1 = 0)$.

We first consider case III. See Table II for the parameters used. These parameter values were chosen to represent the slow reorientation dynamics often found in polar liquids. Figure 6 (see color plate) shows different "slices" of $|R(t_3, t_2, t_1)|^2$. The values of $|R(t_3, t_2, t_1)|^2$ were mapped into colors using the given color map. Red represents the maximum value of $|R(t_3, t_2, t_1)|^2$, while violet represents the minimum

TABLE II
Parameter Values for Brownian Oscillator Calculations

Type	ω (cm^{-1})	γ (cm^{-1})	d	Δ (cm^{-1})	T (K)
Case I (Underdamped)	50.0	6.25	0.34	12.5	20
Case II (Overdamped, fast modulation)	16.6	25.0	0.31	5.0	20
Case III (Overdamped, slow modulation	1.6	2.5	22.1	50	5

Figure 6. The square of the nonlinear response function $R(t_3, t_2, t_1)$ for the overdamped slow modulation limit Brownian oscillator model described in Table II. $|R(t_3, t_2, t_1)|^2$ is plotted as a function of t_3, t_2, and t_1 using the color map shown. The t_3, t_2, and t_1 axes are labeled on the graph. t_1 and t_3 vary from 0 to 0.7 psec. t_2 varies from 0 to 5.8 psec. Note that t_2 is not rendered with the same scale as t_1 and t_3. Parts *a* through *e* show slices in the t_1–t_3 plane for different t_2 values. (*a*) $t_2 = 0$, (*b*) $t_2 = 0.9$ psec, (*c*) $t_2 = 1.9$ psec, (*d*) $t_2 = 3.9$ psec, (*e*) $t_2 = 5.8$ psec.

Figure 9. $|R(t_3, t_2, t_1)|^2$ is shown for the overdamped Brownian oscillator in the slow modulation limit (see Table II) (*a*), the fast modulation limit (*b*), and the underdamped limit (*c*). t_1, t_2, and t_3 vary from 0 to 2.9 psec.

*. above for colour plates. *

value of 0. The color map was also banded—that is, an oscillating gray scale was superimposed on top of the red to violet mapping. The result is bands of oscillating light and dark color that serve as approximate contour lines.

In Fig. 6*a*, a slice in the t_1–t_3 plane at $t_2 = 0$ is shown. From Fig. 6*a*, we see that $R(t_3, 0, t_1)$ peaks in the neighborhood of (but not exactly at) $t_1 = t_3$. In the limit of large inhomogeneous broadening (large Δ), R becomes increasingly peaked at about $t_1 = t_3$. This peaking phenomenon is the reason for the name "photon echo." The outgoing light is produced at a time $t_3 \approx t_1$ after the first pulse. Thus, the delay time between the first two pulses is echoed in the outgoing light. The echo-like nature of the outgoing light is not guaranteed by the use of the photon echo technique itself, but is rather produced when the inhomogeneous broadening is much larger than characteristic frequencies of the motion. When frequencies are on the order of Δ, it is possible to get a signal from photon echo spectroscopy that is not echo-like.

In Fig. 6*b*, a slice of R at $t_2 = 0.9$ psec is shown. $R(t_3, t_2, t_1)$ remains peaked at about $t_3 = t_1$, but now extends over a shorter range of t_1 values. The decrease of this range reflects the destruction of t_1–t_3 coherences by the intervening nuclear dynamics during t_2. Only dynamics which are slow compared to the total duration of the experiment $(t_1 + t_2 + t_3)$ will cause an echo in R. Changing t_2 therefore modifies the relevant timescale τ_r discussed in Section II.A. Dynamics which produce inhomogeneous broadening become effectively *homogeneous* as t_2 is increased.

Figure 6*c* shows the $t_2 = 1.9$-psec slice of R. The echo-like nature of the polarization has been completely destroyed by nuclear dynamics during t_2; there is no peaking at about $t_1 = t_3$. Instead, we note an "island" forming in the t_1–t_3 plane. This island is caused by the Stokes shift. That is, $R_2(t_3, t_2, t_1)$ begins to oscillate at a frequency different from $R_3(t_3, t_2, t_1)$. This behavior occurs because the excited-state density matrix (ρ_{ee}) formed in R_2 relaxes to the excited-state equilibrium $e^{-H_e/kT}$ at long t_2, leading to a redshift in the emission from the excited state.

Figure 6*d* shows the $t_2 = 3.9$-psec slice of R. More islands appear as the Stokes shift continues. The distance in time between islands is equal to the inverse frequency of the separation between the ground- and excited-state peaks in the pump–probe spectrum. As this separation increases, the island spacing decreases. Finally, Fig. 6*e* shows the $t_2 = 5.8$-psec slice of R. Note how the islands are oriented along the t_1 direction, instead of along the $t_1 = t_3$ diagonal (as they were at short t_2). This is a sign of the complete loss of correlation between t_1 and t_3. We now have

$$R(t_1, t_2, t_3) \approx J(t_1)[J^e(t_3)^* + J(t_3)^*] \qquad (t_2 \to \infty), \tag{2.58}$$

where $J^e(t_3) \equiv \mathrm{Tr}[G_{ge}(t_3)\hat{\rho}_e]$ and $\hat{\rho}_e \equiv e^{-H_e/k_BT}/\mathrm{Tr}[e^{-H_e/k_BT}]$. $J^e(t_3)$ is the Fourier transform of the fluorescence lineshape. Equation (2.58) is only valid for an infinite ergodic system. For a finite ergodic system, heating produced by the optical transition will change the temperature in $J^e(t_3)$.

The other planes in Fig. 6*e* also have significance. When $t_3 = 0$, $R(0, t_2, t_1) = J(t_1)$. Thus, the width of the linear absorption lineshape can be estimated from the $t_3 = 0$ plane. The $t_1 = 0$ plane is responsible for impulsive pump–probe spectroscopy.

As mentioned previously, nonlinear spectroscopies measure various aspects of $R(t_3, t_2, t_1)$. We will now consider how the behavior of R is monitored by these different spectroscopies, starting with three-pulse photon echo spectroscopy. The three-pulse photon echo signal corresponding to $R(t_3, t_2, t_1)$ is shown in Fig. 7. The overdamped nature of the Brownian oscillator is reflected in the lack of quantum beats (oscillations) in the signal. As t_2 increases, the three-pulse photon echo signal decays faster as a function of t_1, until a maximum decay rate is obtained. At long t_2 we have

$$S_{3PE}(t_2, t_1) \propto |J(t_1)|^2 \qquad (t_2 \to \infty)\,, \tag{2.59}$$

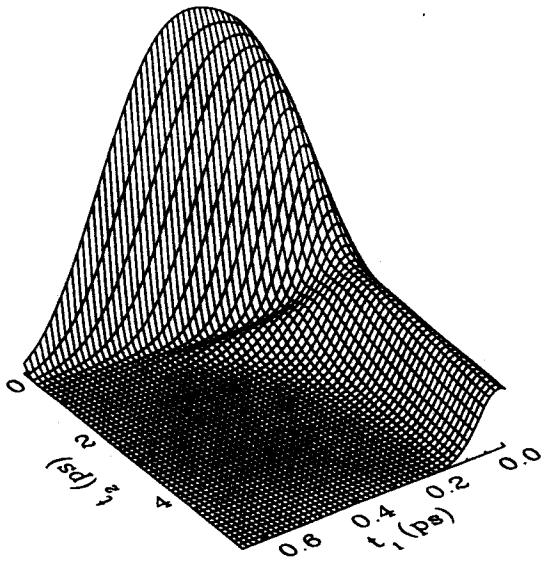

Figure 7. The three-pulse photon echo signal S_{3PE} is shown as a function of the two time delays t_1 and t_2 for the overdamped slow modulation Brownian oscillator system of Table II.

where $J(t_1)$ is defined in Eq. (2.6c). No information is gained over linear spectroscopy by looking at the long time limit of 3PE signal.

A more interesting situation can occur if we have two modes. Let us assume that mode 1 is in the static limit: $\Delta_1 \gg \omega_1, \gamma_1$. Let us also assume that $\Gamma_1 \gg \Gamma_2$, where Γ_i is the full width at half-maximum (FWHM) of the absorption of mode i. For two uncoupled modes we have

$$J(t_1) = J_1(t_1)J_2(t_1)\,, \tag{2.60}$$

where J_n is the contribution mode n. The above choice of parameters indicates that $J_1(t_1)$ will decay much faster than $J_2(t_1)$. Thus, J_1 prevents the collection of useful information on mode 2 from the linear absorption spectrum. Let us define t_i^e to be the "equilibration time" for mode i; that is, t_i^e is chosen so that $M_i(t) \ll 1$ for $t > t_i^e$. If t_2 is chosen to be much greater than t_2^e but much less than t_1^e, we have

$$S(t_1, t_2) \approx |J_2(t_1)|^2 |J_2^*(t_1) + J_2^e(t_1)|^2, \quad (t_2^e \ll t_2 \ll t_1^e)\,. \tag{2.61}$$

Thus, information on mode 2 alone can be collected from the 3PE spectrum.

Three-pulse photon echo spectroscopy is not sensitive to the island structure in $R(t_3, t_2, t_1)$ because t_3 is integrated over. In Fig. 7, we show the three-pulse photon echo signal obtained by integrating R as in Eq. (2.56). When $t_2 = 0$ the signal shows the greatest intensity. This is because phase coherences have not been destroyed by nuclear dynamics while the system is in an electronic population. While the overall relaxation of R can be monitored by the three-pulse photon echo technique, all information on the Stokes shift is lost in the integration over t_3.

Impulsive pump–probe spectroscopy [47,131–136], on the other hand, is sensitive to the Stokes shift. Figure 8 shows the pump–probe signal. When $t_2 = 0$ the impulsive pump–probe signal is the same as the linear absorption. As t_2 increases, the oscillations in R are reflected in the time-resolved Stokes shift. At large t_2 the signal is equal to the sum of the fluorescence and absorption lineshapes. Impulsive pump–probe spectroscopy and three-pulse photon echo spectroscopy provide complementary information when applied to this system. The three-pulse photon echo technique has potentially more information, because it depends on all of $R(t_3, t_2, t_1)$. Since the signal depends on the integral of $|R^2|$ over t_3, however, certain features of R, such as the time-resolved Stokes shift, are not apparent in S_{3PE}. The impulsive pump–probe signal can be strictly inverted to find $R(t_3, t_2, t_1 = 0)$. Information about $t_1 \neq 0$, however, can

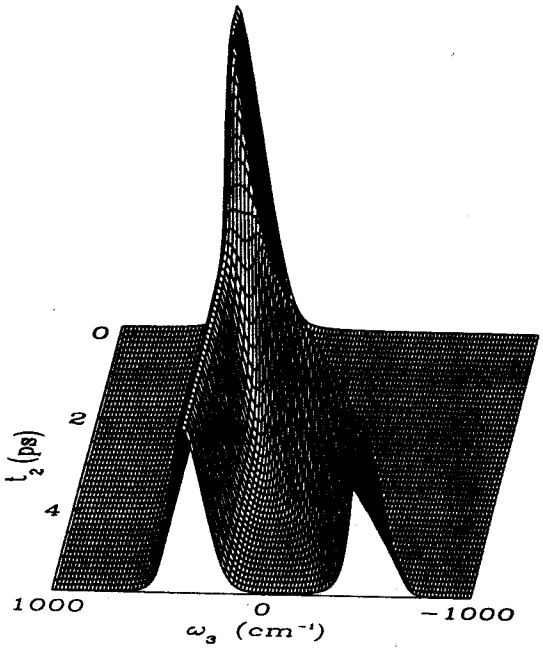

Figure 8. The impulsive pump probe signal S_{PP} for the overdamped slow modulation limit Brownian oscillator of Table II is shown as a function of the detection frequency ω_3 and the delay time t_2.

only be obtained by using longer pulses, which leads to the hole burning limit. The hole burning signal cannot, however, be inverted to give R unless special conditions apply (i.e., the snapshot limit must hold [32]).

In Fig. 9 (see color plate) we show $R(t_3, t_2, t_1)$ for the Case I, II and III systems (see Table II). The case III system is shown to aid comparison with Fig. 6. Let us consider the underdamped oscillator (Case I) first. R shows quantum beats in the planes of constant t_2. The phase of these oscillations changes with t_2. R is not echo-like for this system, even when $t_2 = 0$. This contrasts with the behavior found above for the overdamped oscillator in the slow modulation limit. The 3PE signal for this system is shown in Fig. 10. The oscillations in R are manifested in quantum beats. The impulsive pump–probe signal for Case I is shown in Fig. 11. The signal clearly shows the underlying oscillator frequency in the sidebands at $\omega_3 = \pm 50\,\mathrm{cm}^{-1}$. Oscillations also appear in the t_2 dynamics.

The last system we consider is the overdamped Brownian oscillator in the fast modulation limit (Case II). R is never peaked around $t_1 = t_3$, so the polarization does not demonstrate an echo. This is because the fast modulation dynamics destroys t_1–t_3 phase coherences. In contrast to the

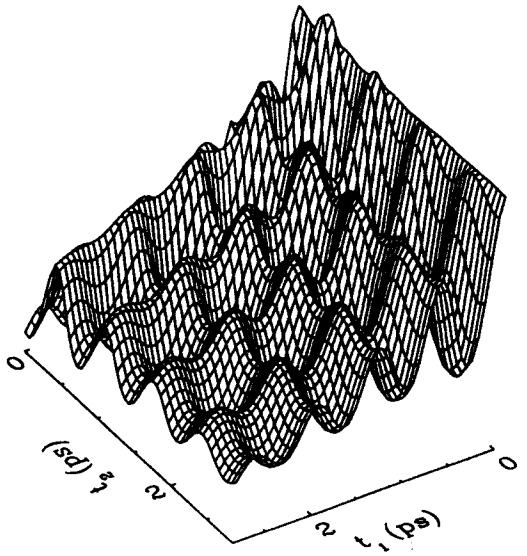

Figure 10. The three-pulse photon echo signal S_{3PE} is shown as a function of the two time delays t_1 and t_2 for the underdamped Brownian oscillator system of Table II.

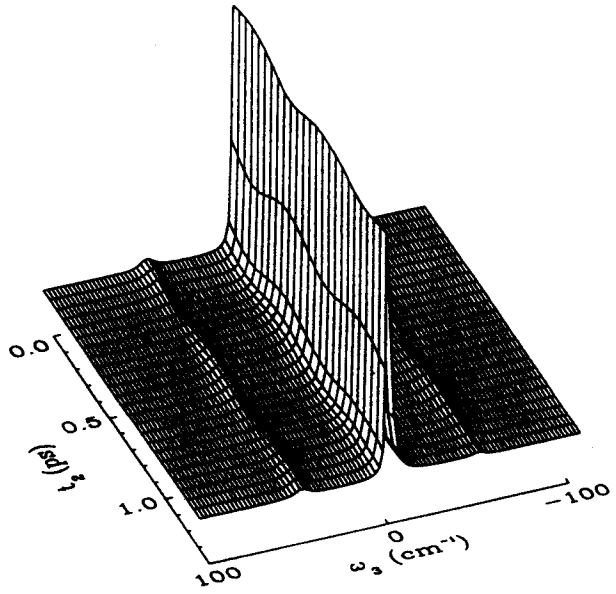

Figure 11. The impulsive pump probe signal S_{PP} for the underdamped Brownian oscillator of Table II is shown as a function of the detection frequency ω_3 and the delay time t_2.

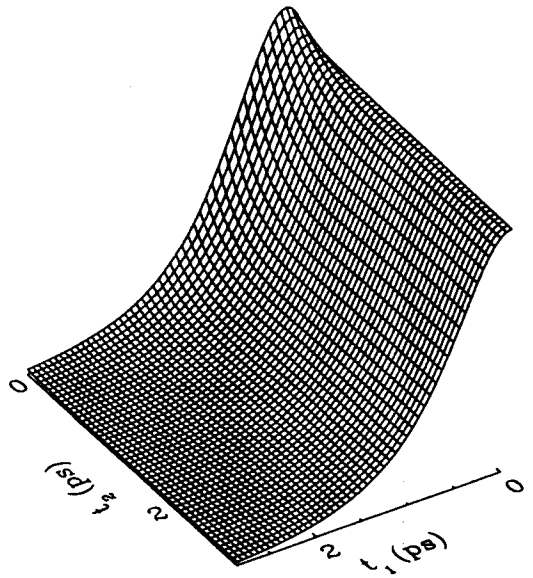

Figure 12. The three-pulse photon echo signal S_{3PE} is shown as a function of the two time delays t_1 and t_2 for the overdamped fast modulation Brownian oscillator system of Table II.

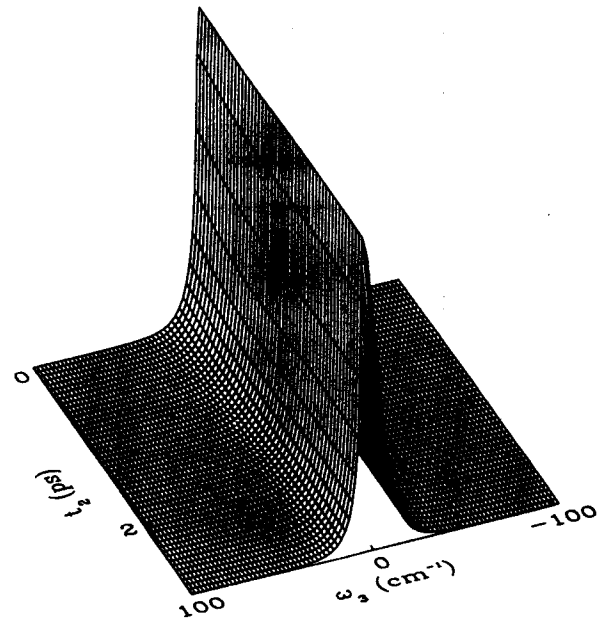

Figure 13. The impulsive pump probe signal S_{PP} for the overdamped fast modulation limit Brownian oscillator of Table II is shown as a function of the detection frequency ω_3 and the delay time t_2.

Case I system, there is little significant dynamics during the t_2 period. Figure 12 shows the three-pulse photon echo signal for this system. The three-pulse photon echo signal for the slow and fast modulation systems are fairly similar, although the impulsive pump–probe signals are strikingly different (see Fig. 13). This illustrates how optical techniques can have varying sensitivity to different aspects of the dynamics.

G. Brownian Oscillator Analysis

In this section we discuss how Brownian oscillator model parameters should be obtained from experiments [26,137,138] or simulations. One of the main advantages of the Brownian oscillator model is that it gives a simple picture of a few damped collective coordinates. Also, the analytic expressions for the response functions can easily be used to predict the outcome of other nonlinear spectroscopies. Comparison between the parameter values obtained from different experiments should provide a valuable check on the applicability of the Brownian oscillator model. A simple case of the inhomogeneous Brownian oscillator model has been used by McMorrow and Lotshaw [26] to analyze the optical Kerr effect in liquids. In their work a single oscillator ($M = 1$) was used. While a distribution of ω values was used, the values of γ and Δ were kept fixed.

Let us describe our method for extracting Brownian oscillator parameters from simulation data. It is possible to fit the simulation data to either $C_c(\omega)$ or $C_s(\omega)$. We expect the results of both methods to be very similar. We fit to $C_c(\omega)$ here. In that case, Eq. (2.47) should be used to relate Δ_i^2 to the Hamiltonian parameter d_i. Trajectories are run for a period t_a (chosen as discussed in Section II.C.1) from independent initial conditions Γ. The values of U are then used to determine the autocorrelation function $C_c(t)$. The autocorrelation function will in general be converged for a time $t_c \ll t_a$; after that time, $C_c(t)$ oscillates randomly about 0. Since these oscillations are numerical artifacts of the finite trajectory length, we damp them out by multiplying $C_c(t)$ by the damping factor e^{-t/t_d}, where the damping time t_d is of the same order of magnitude as the convergence time t_c, while being longer than experimental times of interest. In the frequency domain, this has the effect of producing a smooth $C_c(\omega)$.

The smoothed $C_c(\omega)$ is then fit to the functional form of Eq. (2.46). We have found the following nonlinear least-squares method to be stable: The number of oscillators M is determined from visual inspection of $C_c(\omega)$. The model order should be equal to or somewhat greater than the number of distinct peaks in $C_c(\omega)$. A simulated annealing procedure [139,140] is then used to produce a rough estimate of the correct model parameters. In simulated annealing, a Monte Carlo minimization of the root mean square (RMS) deviation of the fit from $C_c(\omega)$ is performed, much as one would find the minimum energy configuration of a physical

system. Initially, a high "temperature" is chosen which allows various local minima to be sampled. The temperature is gradually reduced through the annealing procedure, leading to nearly optimal parameter values. The final parameters produced by the simulated annealing procedure are then used as initial guesses in a final minimization which uses Powell's method [102]. Although Powell's method cannot distinguish between two global minima, it is efficient at converging to a precise local minimum. We find that this method can reliably fit $C_c(\omega)$ to a Brownian oscillator form. A more traditional algorithm, such as the use of Powell's method alone, requires a good initial guess for the parameter values, which is hard to provide when undertaking a multi-oscillator fit. $W(\boldsymbol{\omega}, \boldsymbol{\gamma}, \boldsymbol{\Delta}, U)$ can be determined by fitting to trajectories obtained from a large number of initial conditions.

An alternative way of parameterizing experimental results has been employed by Tang and co-workers [132,141] in analyzing time-resolved pump–probe experiments. In this technique the *experimental signal* $S(\tau)$, where τ is the delay time between pump and probe, is fit by autoregressive [142] analysis to the functional form:

$$S(\tau) = \sum_{j=1}^{M} (A_j + iB_j) e^{i\Omega_j t} e^{-\Gamma_j t} + \text{c.c.} \tag{2.62}$$

Although the Brownian oscillator model gives the same functional form for $C_c(t)$ in the underdamped limit, we must emphasize that there is in general no simple relation between $(A_j, B_j, \Omega_j, \Gamma_j)$ and the Brownian oscillator parameters $(\Delta_j, \omega_j, \gamma_j)$. One obvious distinction is that different quantities are being fit. In the Brownian oscillator model, $C_c(t)$ is fit to a sum of damped exponentials, not $S(\tau)$. Often (e.g., photon echo spectroscopy) $C_c(t)$ can be extracted by appropriate processing of the experimental signal. A second point is that autoregressive analysis of $C_c(t)$ does not lead directly to the Brownian oscillator model. This is because in the Brownian oscillator model, the $(A_j, B_j, \Omega_j, \Gamma_j)$ are not independent parameters: The ratio A_j/B_j is determined by Ω_j and Γ_j.

III. APPLICATION TO BENZENE–Ar_N CLUSTERS

Molecular and atomic clusters have been a subject of extensive experimental [46,143–152] and theoretical [75,153–164] investigation. Clusters play an important role in nucleation and catalysis. On a more fundamental level, clusters are a bridge between condensed-phase systems and isolated molecules. It is therefore important to ask what

analogues of condensed-phase behaviors exist in clusters, and what behaviors are unique to clusters (such as magic numbers [143]).

Recent interest in the analogues of a bulk phase transition in a finite cluster was initiated by the work of Berry and co-workers [154–160], who have proposed that it is possible for finite clusters to have separate melting and freezing temperatures. Between the melting and freezing temperature is a coexistence regime, where segments of a trajectory at fixed energy show liquid-like or solid-like behavior. This picture has been confirmed by classical molecular dynamics simulations of Ar clusters [155]. Pure Ar clusters can exhibit strikingly sharp phase transitions. For instance, Amar and Berry [155] found a dramatic jump in the RMS bond fluctuation δ for Ar_{13} as the energy was changed by a fraction of the Lennard-Jones well depth. Pure Ar clusters have been studied through properties that have clear macroscopic analogues, such as caloric curves [155], as well as through properties most often used to characterize the dynamics of small systems, such as isomerization rates, fractal dimensions, power spectra, and the K entropy [156]. Freeman and Doll [161] have studied quantum mechanical effects in the melting of Ar clusters.

In an examination of temperature-dependent cluster spectra, Hahn and Whetten [46] have studied size-resolved benzene–Ar_N clusters. They found that spectra with N between 18 and 25 showed both broad (FWHM $\approx 30\,cm^{-1}$) and sharp (FWHM $\approx 5\,cm^{-1}$) spectral features. Hahn and Whetten were able to obtain some temperature control by changing the preparation conditions of the clusters. The spectral features did not shift with temperature, and the sharp features became dominant as the temperature was decreased. These observations were suggested to support the picture of phase coexistence with the sharp and broad features resulting from solid-like and liquid-like configurations, respectively. Very recently Schmidt et al. [150,151] have reported the absorption spectrum of benzene–Ar clusters in the size range $N = 1$–9. They used an improved two-color technique which is less susceptible to cluster fragmentation (providing better control of cluster size) than the one-color technique used by Hahn and Whetten.

Bösiger, Knochenmuss, and Leutwyler [144,165] have studied size-resolved carbazole–Ar_N clusters. They conducted Monte Carlo calculations of the lowest temperature at which a rare gas atom can cross the plane of the carbazole, and studied this behavior as a function of the number of Ar atoms. This behavior is called a "side-crossing transition." Bösiger et al. found that as N was increased, the clusters moved from non-side-crossing to side-crossing configurations. This N-dependent transition correlated well with an increase in the experimental FWHM as a function of N. Knochenmuss and Leutwyler [166b] have conducted a hole

burning study of carbazole–Ar clusters. They were able to burn a hole in the narrow absorption feature which persisted for at least 50 nsec, but were unable to burn a hole in the broad absorption feature. This suggests that the underlying cluster relaxations in the narrow feature are slower than in the broad feature. Even et al. [147] have studied the electronic absorption spectrum of size-resolved dichloroanthracene–Kr_N and dichloroanthracene–Ar_N clusters. They found that the spectrum is sharp at $N = 1$, but becomes broad and featureless at $N = 11$. They interpreted this behavior in terms of a wetting–nonwetting transition from two-dimensional configurations to three-dimensional configurations. Interestingly, at $N = 17$, sharp spectral features once again appear. This change was assigned to a nonrigid-3D-to-rigid-3D transition.

Previous theoretical work [167,168] on rare gas clusters containing a chromophore molecule has centered upon several problems. There have been attempts [162,163] to explain the spectral shift of chromophore–rare-gas clusters via Longuet–Higgins–Pople theory [164] and semiempirical electronic structure calculations [169]. An electrostatic model taking into account intermolecular electronic overlap was used by Ben-Horin et al. [170] to calculate the ionization potential of large van der Waals molecules. Penner et al. [152] have compared experimental results on the radiative lifetime and spectral shift of dichloroanthracene–Ar, Kr, and Xe clusters with the predictions of a classical electrostatic model [171]. Leutwyler and Bösiger [166b] have performed Monte Carlo simulations of carbazole–Ar clusters. They studied how cluster configurations and RMS bond fluctuations changed with the number of Ar atoms and temperature.

There has also been previous theoretical work on benzene–Ar clusters. Adams and Stratt [75] have conducted a Monte Carlo simulation of benzene–Ar_{19} and Ar_{19} clusters. By examining the distribution of instantaneous normal mode frequencies, they found that the presence of the benzene in the cluster made the solid-to-liquid-phase transition less sharp. Schmidt et al. [151] recently reported Monte Carlo simulations of benzene–Ar_2 clusters in conjunction with rotationally resolved spectra.

In previous work [56,57] we used the inhomogeneous cumulant method to calculate the absorption spectrum of benzene–Ar clusters for $N = 1, \ldots, 21$. We found that benzene–Ar_N clusters at 20 K undergo a transition from solid at $N = 1$ to a two-dimensional liquid at $N = 2, 4$, and then change to a three-dimensional liquid as N increases from 10 to 21. We also looked closely at the role of diffusion, large-amplitude cluster motions, the timescale of cluster motions, and cluster structure in determining the observed spectra. Corresponding to these structural transitions, we identified *spectroscopic transitions* as the absorption moves

between the underdamped oscillator regime to the motional narrowing regime.

We discuss here several other aspects of the spectroscopy of benzene–Ar clusters. We focus on the convergence of spectroscopic quantities as a function of cluster size. We find that interesting changes in the distribution of Ar atoms around the benzene occur at cluster sizes as large as 200. This leads to a highly structured, nonmonotonic convergence of the spectral shift with N. We also examine how the spectroscopy of benzene–Ar clusters can be understood with the Brownian oscillator model. We find that three to five oscillators can adequately represent the spectra of benzene–Ar clusters. In previous work [72], we did not find any evidence of phase coexistence in benzene–Ar_N clusters for $N = 1, \ldots, 21$. Here we report behavior that is suggestive of phase coexistence in a larger cluster ($N = 40$); in particular we have found jump dynamics of $U(t)$ associated with a shell-specific melting phenomenon. We also look at nonlinear optical quantities here.

To calculate the optical properties of the cluster, we must specify the ground-state and excited-state potential surfaces V_g and V_e. *Ab initio* potential energy surfaces are only available for the benzene–Ar_1 isomer [172]. Therefore, we used empirical potentials described in detail elsewhere [57]. We took the benzene molecule to be rigid but not fixed. The ground-state potential consisted of a standard pairwise additive Lennard-Jones carbon–argon and hydrogen–argon parameterization that has been successfully applied to other conjugated chromophore/rare-gas clusters [173]. Similarly, we used an empirical excited-state potential function. Since the first excited state of benzene has only modest charge separation, it was natural to take a Lennard-Jones form (thus neglecting charge-induced dipole interactions). The parameters of the excited state were previously determined by fitting to the progression of spectral shifts in the linear absorption as a function of the number of Ar atoms N.

Initial conditions corresponding to a Boltzmann distribution at a given temperature were generated by a staged classical Monte Carlo annealing procedure [139]. Following the annealing, a molecular dynamics calculation was undertaken to find $U_1(t)$ [Eq. (2.31)]. We do not consider spectroscopies involving excited-state populations here, so it was unnecessary to calculate $U_2(t)$. The annealing run of 100,000 cycles (i.e., each particle was moved 100,000 times) began at a temperature of 100 K, which was then gradually lowered to a final temperature of 20 K. During the annealing, a confining sphere about the benzene was imposed by adding an extra term to the potential

$$V_{\text{sphere}}(r) = A(r/r_c)^{20} . \tag{3.1}$$

We took $A = 0.07\,\text{cm}^{-1}$. r_c was set to 15 Å for the clusters with $N \leq 50$, while r_c was set to 18 Å for the $N = 75$, 100, and 200 clusters. Initial velocities were chosen from a classical thermal distribution at the given temperature. The center-of-mass velocity of the entire cluster was set to zero at the beginning of the molecular dynamics calculation. The clusters had nonzero total angular momentum.

Each trajectory was run for 262,144 time steps of 3.6 fsec. This made for a total trajectory length of 943 psec. A leap-frog Verlet algorithm [103] was used. The energy was fixed by scaling the velocities once every 1024 steps. The motion of the benzene was described by center-of-mass and quaternion parameters. At each step along the trajectories the energy gap U was evaluated. The classical autocorrelation function $C_c(\omega)$ was then determined from the U values by the method discussed in the previous section. A damping time of $t_d = 5.6$ psec (see Section II.G) was employed in the calculation of $C_c(\omega)$. Since we were interested in treating quite large clusters to study convergence to the bulk, a single 943-psec trajectory was generated for each cluster. Processes occurring on a timescale slower than 943 psec could be included by running multiple independent trajectories. See Refs. 56 and 57 for a determination of the inhomogeneous contribution to linear spectroscopy in smaller clusters.

A. Brownian Oscillator Analysis of $C_c(\omega)$

In this subsection we analyze the spectral density $C_c(\omega)$ as a function of N. Figure 14 shows the calculated $C_c(\omega)$ for a single representative trajectory drawn from the canonical ensemble at 20 K for $N = 10 \ldots 30$ clusters. The appropriate number of Brownian oscillators (M) changes with N. For instance, when $N = 10$, $C_c(\omega)$ has two distinct peaks, a shoulder at $30\,\text{cm}^{-1}$, and a second shoulder at about $70\,\text{cm}^{-1}$. This suggests that M should be set to 4 for this trajectory. Similarly, we found the following model orders (N, M): (10, 4), (14, 5), (16, 4). It sufficed to choose $M = 3$ for the other clusters.

Also shown in Fig. 14 are the results of the M-mode Brownian oscillator model to fit $C_c(\omega)$ by the combination of simulated annealing and Powell's method described in Section II.G. A good fit was achieved. There are several interesting trends in the shape of $C_c(\omega)$ as a function of N. The peak at $\omega = 0$ decreases in weight from $N = 10$ to $N = 16$, then increases in weight from $N = 21$ to $N = 30$. This peak can be thought of as corresponding to slow, diffusive motions. In Section III.C we show that the change in the weight of the zero-frequency peak correlates with the Ar–Ar and benzene–Ar (B–Ar) RMS bond fluctuations. That is, clusters with a smaller zero-frequency peak of $C_c(\omega)$ in the $N = 10$–30 size regime are more rigid than clusters with larger zero-frequency peaks of $C_c(\omega)$.

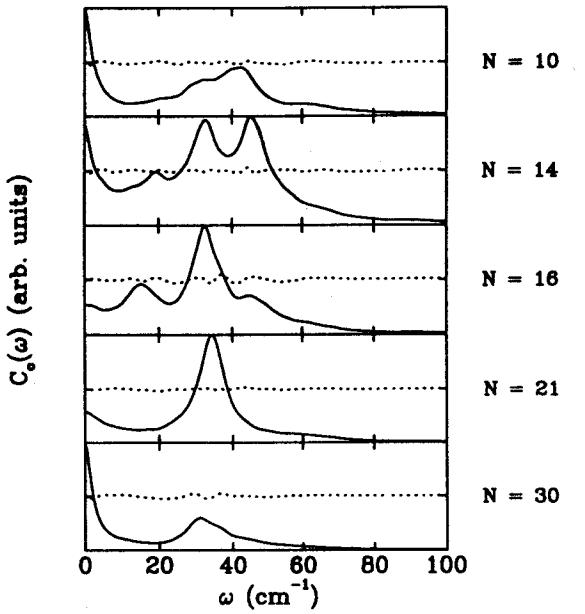

Figure 14. The spectral density $C_c(\omega)$, as a function of N for representative trajectories from the $T = 20$ K thermal ensemble. Solid line: $C_c(\omega)$, normalized to have unit maximum value. Dotted line: difference between the Brownian oscillator fit to $C_c(\omega)$ and $C_c(\omega)$, plotted with the origin shifted for clarity.

The largest nonzero peak of $C_c(\omega)$ is the dominant frequency of the motion. Inspecting Fig. 14, we see that the dominant frequency of the motion decreases from $N = 10$ to $N = 14$, then remains nearly constant for $N = 16$ to $N = 30$.

In Fig. 15, we display $C_c(\omega)$ in the size range $N = 40$ to $N = 200$. For $N = 40$ and $N = 75$–200 the maximum peak in $C_c(\omega)$ occurs at $\omega = 0$; diffusive motions mostly determine spectroscopic observables for these sizes. The first peak in $C_c(\omega)$ decreases monotonically with N, whereas the second peak *increases* monotonically with N. Recall that (see Section II.D) the Bloch equations in conjunction with a Gaussian inhomogeneous distribution can be derived from the Brownian oscillator model by assuming that $C_c(\omega) = A\delta(\omega) + B$; that is, only fast (homogeneous broadening) or slow (inhomogeneous broadening) motions exist. The divergence and broadening of the two nonzero frequency peaks of $C_c(\omega)$ with N makes the Bloch equation description become better for larger N.

The decomposition of $C_c(\omega)$ in terms of the three-mode Brownian oscillator fit is displayed in Figs. 16 and 17. Each oscillator clearly

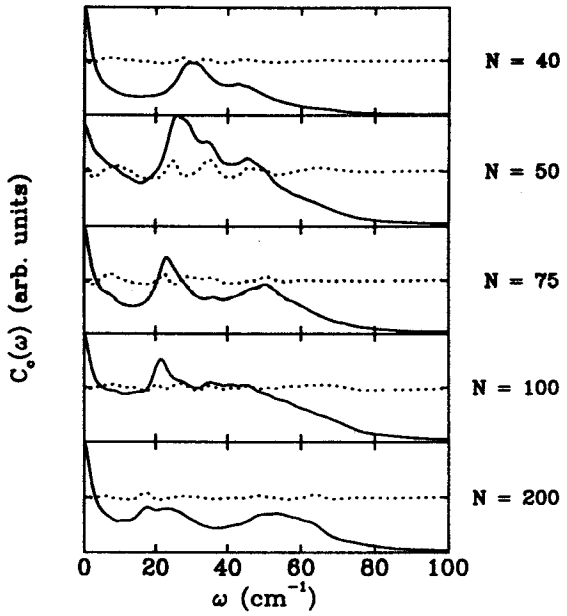

Figure 15. As in Fig. 14, but for $N = 40 \ldots 200$.

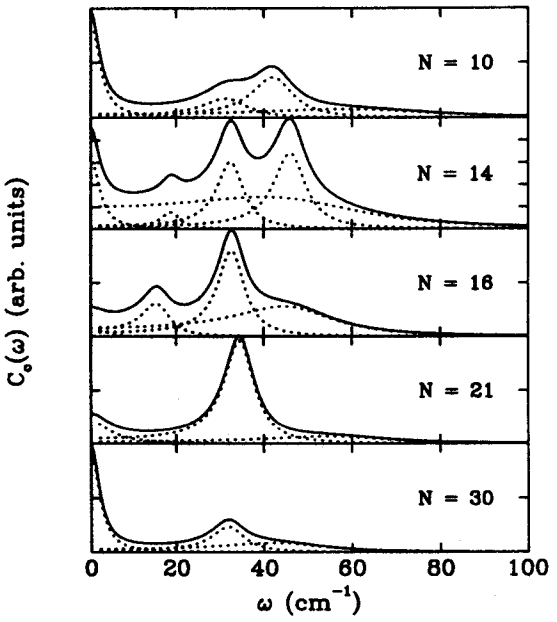

Figure 16. Solid line: the best fit of $C_c(\omega)$ to a three-mode Brownian oscillator model. Dotted lines: the individual contributions to $C_c(\omega)$ from each Brownian oscillator.

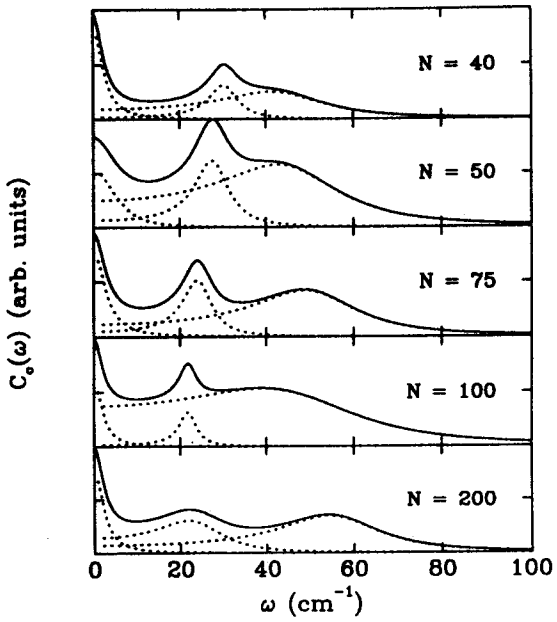

Figure 17. As in Fig. 16, but for $N = 40 \ldots 200$.

corresponds to a peak or a shoulder in $C_c(\omega)$. In general, we have found that the number of oscillators is best chosen to be equal to the number of peaks in $C_c(\omega)$. Adding more oscillators improves the fit, but the oscillator parameters become less physical and vary erratically as system parameters (such as temperature or N) is varied. Sometimes extra insight into $C_c(\omega)$ can be gained by examining individual oscillators. For instance, the $N = 16$ cluster has an overdamped oscillator with very small weight, indicating that overdamped motions are not relevant to spectroscopic observables for this trajectory. Another interesting feature revealed by Figs. 16 and 17 is that the widths of the zero-frequency modes decrease between $N = 50$ and $N = 200$, whereas the width of the nonzero-frequency modes increase over the same size range. This is a manifestation of the transition to Block-like behavior as N increases.

The Brownian oscillator picture has greater significance and predictive power if the oscillator parameters vary smoothly as system parameters are changed. As mentioned above, this smooth variation is lost if M is chosen to be too large. Figure 18 shows the parameters used in the Brownian oscillator fits as a function of N; the actual values used are given in Table III. It is clear that the present method of analysis gives parameters that vary smoothly with N. For instance, the maximum oscillator frequency

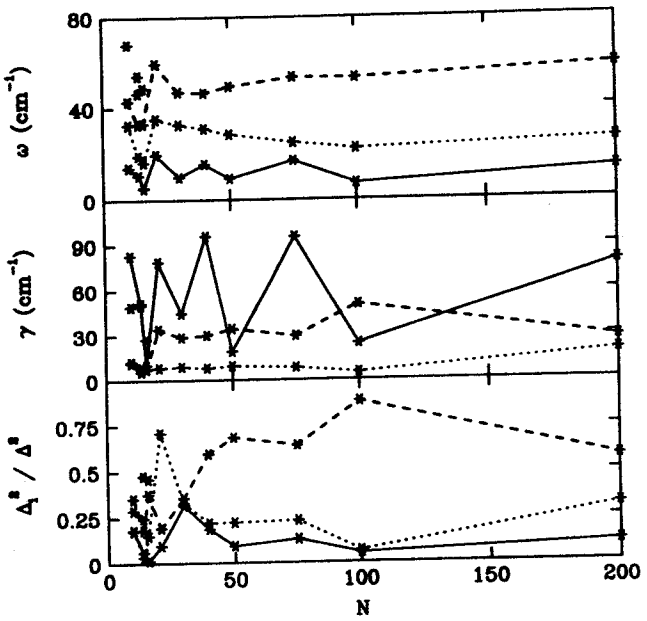

Figure 18. Parameters for the Brownian oscillator model.

increases smoothly with N between $N = 40$ and $N = 200$. On the other hand, the middle oscillator frequency decreases smoothly with N. The γ_i and the Δ_i show similar progressions in this size regime. On the other hand, the oscillator parameters behave more erratically for smaller sizes ($N < 30$). This is not a failure of the fitting procedure, however, but is instead caused by the rapid variation of $C_c(\omega)$ itself. The lowest-frequency modes show oscillations in ω and γ. Since this oscillator is strongly overdamped ($\gamma \gg \omega$), $M(t)$ for this mode will decay exponentially with the rate $\Lambda = \omega^2/\gamma$. Thus, only the ratio Λ is relevant for a strongly overdamped mode. Λ varies more smoothly with N than does ω or γ.

We now discuss the behavior of Brownian oscillator analysis in the time domain. Autoregressive analysis can require high model orders to give good results at long times [142], because it is essentially a fit to the short time behavior of $C_c(t)$. Brownian oscillator analysis gives equally good results in the time and frequency domain. Figures 19 and 20 shows the behavior of $C_c(t)$ and the Fourier transform of the Brownian oscillator fit to $C_c(\omega)$ as a function of N. The behavior of $C_c(t)$ is well reproduced by the Brownian oscillator model for several vibrational periods. The $N = 21$ trajectory shows the most prominent vibrational structure, whereas the Bloch-like behavior of the larger clusters is clearly

TABLE III
Parameters Used in the Brownian Oscillator Fits

N	Δ_i^2/Δ^2	γ_i (cm^{-1})	ω_i (cm^{-1})	Δ (cm^{-1})	ω_{eg} (cm^{-1})
10	0.352	42.8	11.4	12.57	42.21
	0.289	67.8	49.1		
	0.181	32.6	12.4		
	0.178	13.9	83.1		
14	0.477	54.0	51.4	13.19	43.33
	0.247	46.4	8.78		
	0.183	32.9	7.38		
	0.060	10.6	50.4		
	0.035	19.2	5.65		
16	0.46	48.6	27.5	14.47	39.93
	0.375	33.1	7.34		
	0.15	16.3	7.96		
	0.0147	5.21	10.1		
21	0.71	35.0	8.26	17.16	35.49
	0.194	59.3	34.1		
	0.0959	19.7	79.0		
30	0.356	46.8	28.8	19.54	54.11
	0.328	32.6	9.03		
	0.316	9.78	44.8		
40	0.595	46.4	30.1	16.25	68.90
	0.22	30.8	8.16		
	0.186	15.4	95.9		
50	0.684	49.2	34.4	17.31	58.02
	0.222	28.3	9.44		
	0.0932	9.21	19.2		
75	0.64	53.2	29.6	14.94	84.94
	0.231	24.8	8.29		
	0.129	16.8	95.5		
100	0.882	7.0	24.4	16.03	78.24
	0.066	22.1	4.9		
	0.052	52.8	50.3		
200	0.314	25.7	19.1	16.42	86.89
	0.574	57.9	27.9		
	0.112	13.4	78.6		

demonstrated by the combination of fast (<1 psec) and slow (>5 psec) relaxation in the $N = 100$ and $N = 200$ clusters.

Let us summarize the conclusions of this subsection:

- $C_c(\omega)$ makes a transition from damped behavior at $N = 10$ to oscillatory behavior at $N = 16, 21$ and then finally back to damped behavior at $N = 75 \ldots 200$. The $N = 100$ and 200 trajectories showed "Bloch-like" behavior.

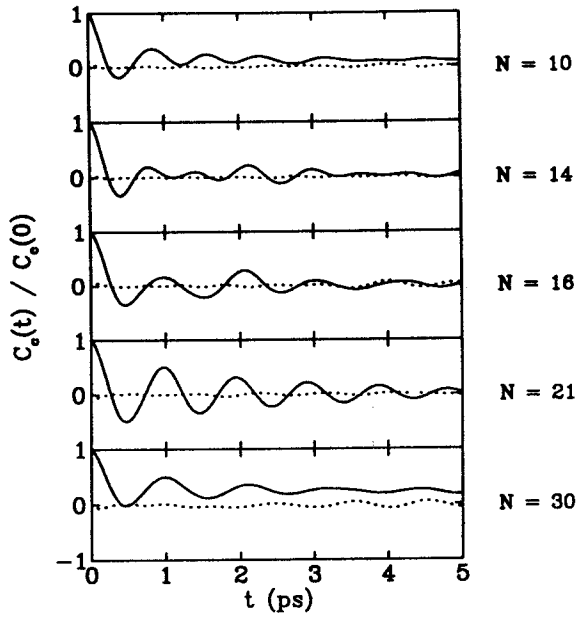

Figure 19. $C_c(t)/C_c(t=0)$ for $N = 10 \ldots 30$. The dotted line shows the difference between the Brownian oscillator fit and the actual correlation function.

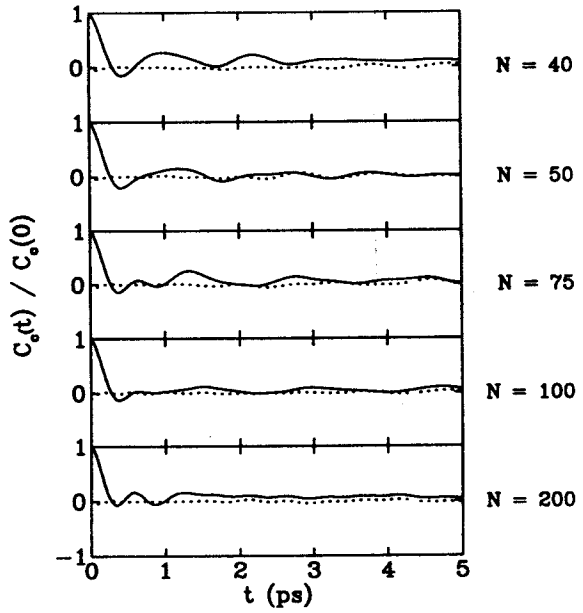

Figure 20. Same as Fig. 19, except $N = 40 \ldots 200$.

- Three to five Brownian oscillators sufficed to fit $C_c(\omega)$. The parameters of the Brownian oscillator model varied smoothly with N, suggesting that the Brownian oscillator model should be useful in interpreting cluster spectra.
- Unlike low-order autoregressive fitting, Brownian oscillator analysis can give a good fit to $C_c(t)$ for several vibrational periods.

B. Calculation of Spectroscopic Quantities

In this subsection, we study the linear and nonlinear spectroscopy of benzene–Ar_N clusters. In Section II.C we have outlined three ways of finding spectroscopic observables given classical dynamics: phase averaging, the second-order cumulant approximation, and the static approximation. We first study linear absorption. Figures 21 and 22 show the linear absorption of benzene–Ar clusters calculated via phase averaging [Eq. (2.32)], the cumulant approximation [Eq. (2.20)], and the static approximation [Eq. (2.34a)]. The static approximation (dotted line) always overestimates the absorption linewidth. This is a result of motional

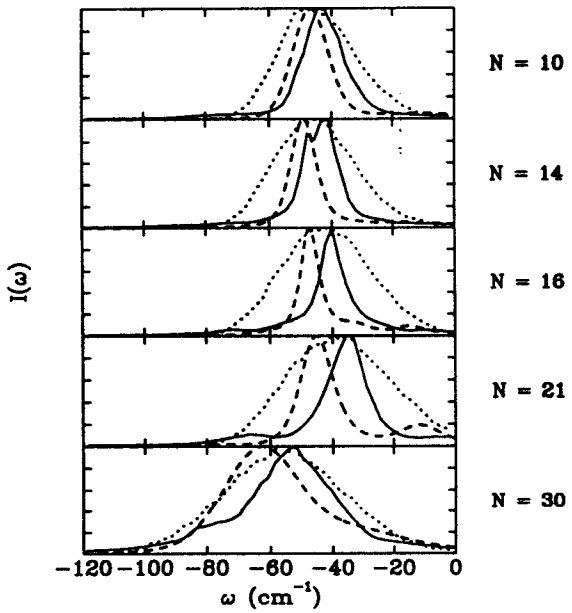

Figure 21. Absorption spectra of benzene–Ar_N clusters. Solid line: phase-averaging formula. Dashed line: second-order cumulant approximation. Dotted line: static approximation. Here and in subsequent spectra, ω is plotted relative to the gas-phase 0–0 absorption frequency ω_{eg}^0.

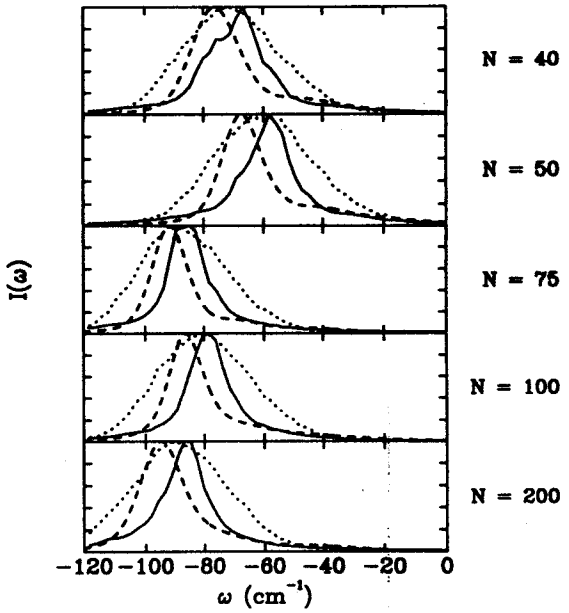

Figure 22. As in Fig. 3.8, but with $N = 40 \ldots 200$.

narrowing. In a previous paper, we found that motional narrowing is crucial to understanding the spectroscopy of benzene–Ar_N clusters. The motional narrowing effect becomes most pronounced when rapid motions dominate, such as when $N = 16$ and $N = 21$. The static approximation works best for the $N = 30$ spectrum, which shows the greatest weight of $C_c(\omega)$ around $\omega = 0$. Motional narrowing in nuclear magnetic resonance is normally achieved by raising the temperature. Then Δ is fixed and Λ^{-1} becomes shorter as T is raised. In solids, motional narrowing is less pronounced at higher T since Δ increases while Λ^{-1} remains fixed (phonon frequencies).

For all the spectra, $I(\omega)$ as predicted by the cumulant approximation is red shifted with respect to $I(\omega)$ as predicted by phase averaging. Both methods, however, predict the same first moment of $I(\omega)$. This is because the cumulant approximation predicts more spectral asymmetry (see Section II.C) than does the phase-averaging technique. The importance of vibrational quantization effects at 20 K means that the cumulant approximation is the preferred method at this temperature.

Figures 21 and 22 show an interesting pattern of spectral shifts. From $N = 10$ to $N = 21$, the spectral shift decreases, which is in agreement with experimental data [46,150]. For larger N values an oscillation in the

spectral shift occurs. Recently, Li et al. [174] have pointed out that the spectral shift of clusters containing a chromophore can often be non-monotonic, with regions of slow variation with N. We find a non-monotonic variation of the spectral shift with N in our calculations. Below, we show that the oscillations in the spectral shift as a function of N are due to changes in the solvation structure around the benzene. The Ar–Ar structure, on the other hand, remains insensitive to N.

We can gain further insight by determining the extent to which the changes in the first and second spectral moments of $I(\omega)$ can be predicted by simple scaling arguments. Previously, Penner et al. [152] have discussed the scaling of the spectral shift and the radiative lifetime with cluster size. The spectral shift, $\langle U \rangle - \omega_{eg}^0$, is related to the first moment of the electronic absorption spectrum:

$$\langle U \rangle = \frac{\int_{-\infty}^{\infty} I(\omega)\omega \, d\omega}{\int_{-\infty}^{\infty} I(\omega) \, d\omega} . \tag{3.2}$$

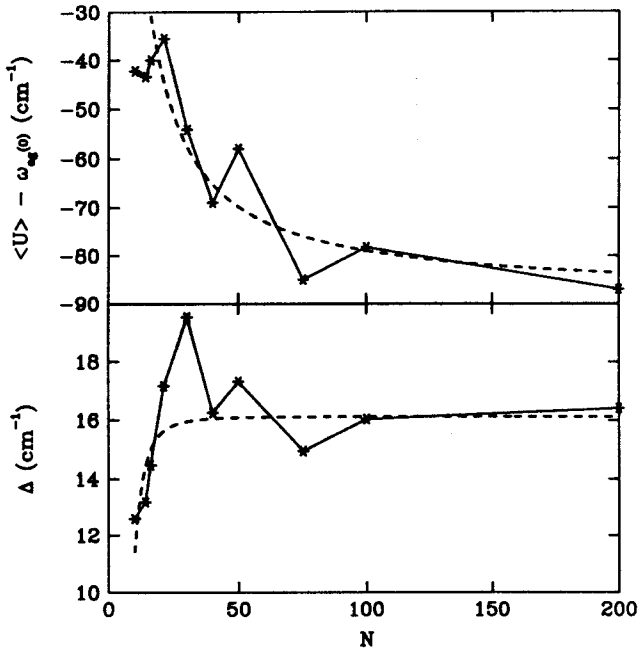

Figure 23. Scaling of the first ($\langle U \rangle$) and second (Δ) moments of the electronic absorption of benzene–Ar_N clusters. The dotted line shows the best fit to $d = 3$ scaling. The solid line is provided as a visual aid.

In Appendix A, we show that $\langle U \rangle$ should scale as

$$\langle U \rangle - \langle U \rangle_{N=\infty} \propto N^{(d-m)/d}, \tag{3.3}$$

where d is the spatial dimension, and $U(r) \propto r^{-m}$ at large r. For the benzene–Ar clusters, we take $m = 6$. We also show that Δ should scale as

$$\Delta - \Delta_{N=\infty} \propto N^{(d-2m)/d}. \tag{3.4}$$

In the top panel of Fig. 23, we show $\langle U \rangle$ as a function of N. Apparently, $\langle U \rangle$ undergoes significant oscillations in the size range considered. In Section III.C we relate these oscillations to changes in the local structure around the benzene. Also shown in Fig. 23 is the best fit of the $N = 40 \ldots 200$ spectral shift to scaling law of Eq. (3.3) for $m = 6$ and $d = 3$. The scaling law gives a reasonable fit to the overall behavior of the spectral shift for $N \leq 16$. Between $N = 10$ and $N = 16$ there is an oscillation in the spectral shift that cannot be predicted by simple size effects.

Also shown in Fig. 23 is the behavior of the second cumulant moment of the electronic absorption lineshape (which is equal to Δ^2). Δ shows

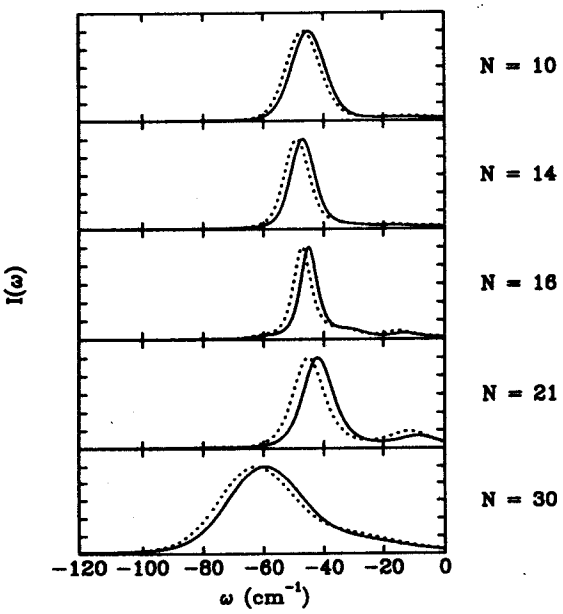

Figure 24. Absorption spectra of benzene–Ar_N clusters. Solid line: cumulant technique without zero-point energy correction of Eq. (2.27). Dotted line: cumulant technique with zero-point energy correction.

oscillations that correlate well with the oscillations in $\langle U \rangle$. We show the best fit of the scaling law [Eq. (3.4)] for $N = 40 \ldots 200$. The scaling law predicts the rapid decrease of Δ for $N \leq 30$ reasonably well.

In Figs. 24 and 25 we compare $I(\omega)$ calculated through the cumulant method with and without the zero-point energy correction factor. That is, one calculation used Eq. (2.27) to relate $C_c(\omega)$ to $C_s(\omega)$. The other calculation simply set $C_c(\omega) = C_s(\omega)$. We conclude that zero-point effects are present but not dominant at 20 K for $N = 10 \ldots 200$. Adding zero-point energy increases Δ. This causes the spectra to become more asymmetric, so the peak of the calculations with zero-point energy always lies to the red of the peak of the calculations without zero-point energy. The first moments of the spectra are unchanged by the inclusion of zero-point energy.

We next turn our attention to nonlinear spectroscopies, which offer more sensitive probes of dynamical properties than linear absorption. We consider photon echo spectroscopy here. In the photon echo experiment, a laser with wavevector k_1 and frequency ω_1 sets up an optical coherence in the sample. After the pulse, the coherence decays during the t_1 period because of dephasing processes. The part of this decay due to inhomoge-

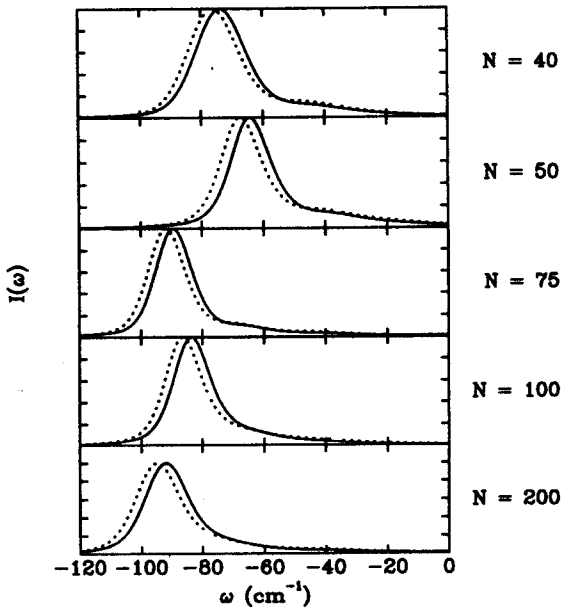

Figure 25. Absorption spectra of benzene–Ar_N clusters. As in Fig. 24, but with $N = 40 \ldots 200$.

neous broadening, however, can be reversed by the application of a second pulse with wavevector k_2 and frequency ω_2. The echo signal is produced with wavevector $k_S \equiv 2k_2 - k_1$ and frequency $2\omega_2 - \omega_1$. The experimental observable in the photon echo experiment is the total number of photons produced in the k_S direction as a function of the delay time τ between the two pulses. The signal $S(\tau)$ is proportional to the square of the third-order (in E) macroscopic polarization with wavevector k_S:

$$S(\tau) = \int_0^\infty dt |P^{(3)}(k_S, t)|^2 . \tag{3.5}$$

Given the above assumption of ultrashort pulses, the photon echo experiment directly measures the nonlinear response function $R_3(t, 0, \tau)$ of Eqs. (2.11a)–(2.11d):

$$P^{(3)}(k_S, t) \propto R_3(t, 0, \tau) \equiv \mathrm{Tr}[G_{eg}(t) G_{ge}(\tau) \hat{\rho}_g] . \tag{3.6}$$

Figures 26 and 27 show the photon echo signal as calculated by phase averaging and the cumulant approximation. The cumulant results show a

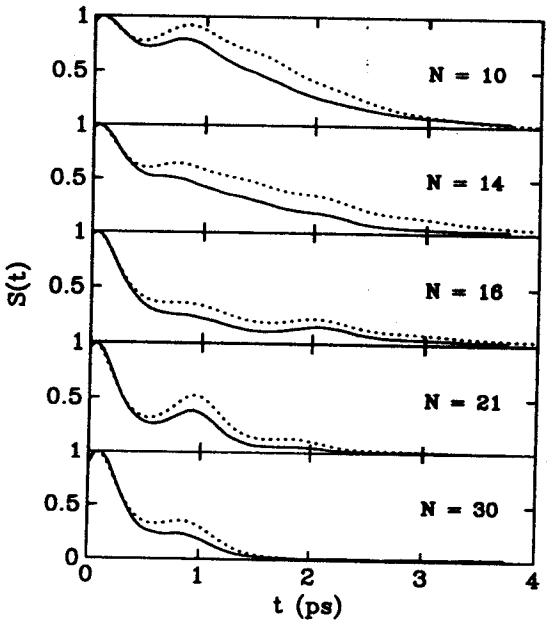

Figure 26. Normalized photon echo signal of benzene–Ar_N clusters, for $N = 10 \ldots 30$. Solid line: phase-averaging calculation. Dotted line: cumulant calculation.

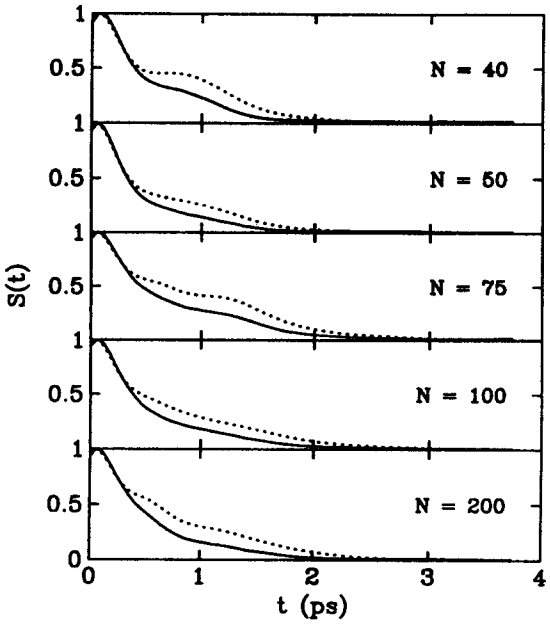

Figure 27. Same as Fig. 26, for $N = 40 \ldots 200$.

more pronounced vibrational structure than do the phase-averaging results. This is because the cumulant calculations include the zero-point energy correction of Eq. (2.27), which has the effect of increasing the amplitude of high-frequency modes. We have also used the cumulant approximation without the zero-point correction. In that case the phase-averaging and cumulant results are nearly identical. The $N = 10$ cluster shows the largest difference between the cumulant and phase-averaged results. This is not surprising, since the central limit theorem suggests that the cumulant method should be best for systems with many independent degrees of freedom.

As N increases, the photon echo signal decays more rapidly. This is because Δ increases with N, thus destroying phase coherences more effectively. For instance, the Bloch equations predict that the photon echo signal decays exponentially at long times with a rate equal to $4/T_2$. On the basis of the Brownian oscillator model, we can show that $T_2 = 1/\Delta^2\tau$, where t is the timescale of solvent relaxation. Thus, as Δ increases, the photon echo decays more rapidly, Nevertheless, the photon echo signals in Fig. 26 do not decay exponentially with time. Similar nonexponential photon echoes have been observed recently in polar liquids [50,51]. For both clusters and polar liquids, the nonexponential

photon echo decay is due to a vibrational solvent response occurring with a finite timescale, as opposed to the overdamped fast response assumed in the Bloch equations.

The photon echo signals closely reflect the dynamics revealed by $C_c(\omega)$. For instance, the most vibrational (as opposed to overdamped) $C_c(\omega)$ occurred when $N = 21$. This cluster also shows the most vibrational photon echo signal. As N is further increased, the photon echo signal gradually becomes less vibrational. At $N = 200$, the decay is approximately exponential, reflecting the Bloch-like shape of $C_c(\omega)$. The overall decay of the photon echo signal is also of interest. In the fast modulation limit the Brownian oscillator model predicts that

$$t_{PE} \equiv \int_0^\infty S_{PE}(t)\, dt = T_2/4\,. \tag{3.7}$$

In Appendix A, we use scaling arguments to show that t_{PE} should vary with N as

$$t_{PE}(N) - t_{PE}(N=\infty) \propto N^{(d-2m)/d}\,, \tag{3.8}$$

where d is the dimensionality of the cluster and U behaves as $1/r^m$ at large r. For benzene–Ar clusters, we predict that t_{PE} should scale as $1/N^3$. A comparison between this scaling law and calculated t_{PE} values based on phase averaging is shown in Fig. 28. A good fit is obtained. In particular, the rapid increase in t_{PE} with N for small N is predicted.

Let us summarize the main conclusions of this subsection:

- The electronic absorption of benzene–Ar_N clusters is in the intermediate modulation limit. Motional narrowing is important for the N values studied here.
- There is an interesting oscillation in the spectral shift between $N = 40$ and $N = 200$. Thus, the transition to bulk behavior occurs slowly in benzene–Ar_N clusters.
- For $N < 40$ the photon echo signals have a substantial vibrational character. This closely reflects the behavior of $C_c(\omega)$. At $N = 100$ and $N = 200$ the decay becomes more nearly exponential, reflecting the Bloch-like character of $C_c(\omega)$ found at these N values.
- The cumulant approximation agreed qualitatively with phase averaging for the electronic absorption and for photon echo spectroscopy. The main difference between the two methods when applied to photon echo spectroscopy is the zero-point correction of Eq. (2.27).

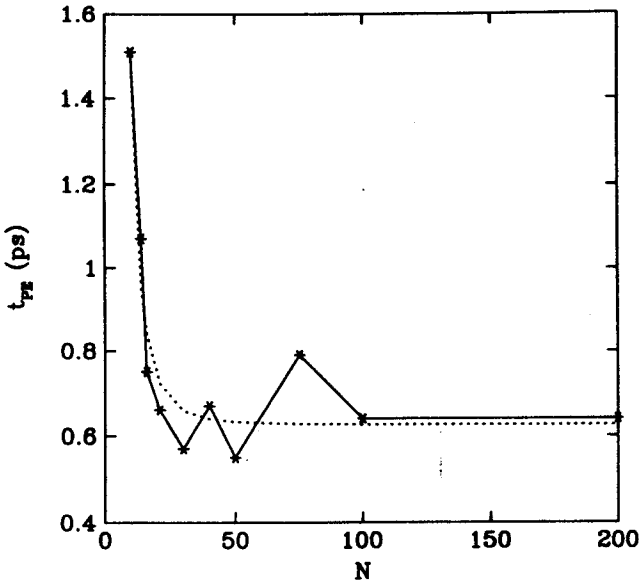

Figure 28. Photon echo decay times (t_{PE}) as a function of N. Dotted line: prediction of the scaling law of Eq. (3.8). The calculated values are shown with symbols; a solid line has been drawn through these symbols to serve as a visual aid.

C. Dynamical and Structural Trends as a Function of N

In this subsection we consider how the dynamics and structure of benzene–Ar_N clusters vary with N. Figure 29 shows how the Ar–Ar pair distribution function $g_{Ar-Ar}(r)$ and the B–Ar pair distribution function $g_{B-Ar}(r)$ (defined with respect to the center of mass of the benzene) vary with N. $g_{Ar-Ar}(r)$ shows a remarkably smooth variation with N. For instance, the first peak at $r \approx 3.8$ Å and the second peak at $r \approx 7$ Å remain largely unchanged from $N = 10$ to $N = 30$. $g_{B-Ar}(r)$, however, shows a striking dependence on N. As N is increased from 10 to 16, $g_{Ar-Ar}(r)$ becomes more solid-like, with sharp peaks and minima near zero. This change correlates well with the spectral narrowing of the linear absorption that occurs in the same size range. For $N = 21$ and $N = 30$, $g_{B-Ar}(r)$ becomes more liquid-like whereas the linear absorption broadens.

In Fig. 30 we show $g_{Ar-Ar}(r)$ and $g_{B-Ar}(r)$ for $N = 40 \ldots 200$. Once again, $g_{Ar-Ar}(r)$ shows a gradual evolution with N that is devoid of any striking changes. As N increases from 40 to 200, the second peak of $g_{Ar-Ar}(r)$ splits into two closely spaced peaks at $r \approx 7$ and $r \approx 7.7$ Å. Also, as N increases, $g_{Ar-Ar}(r)$ is nonzero over larger r values, a consequence of

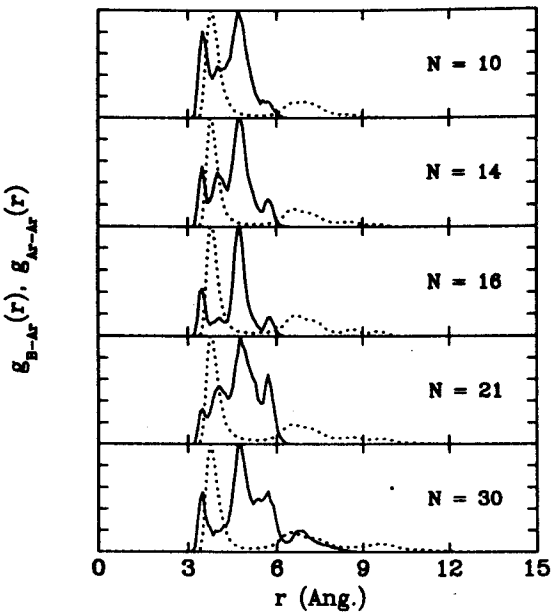

Figure 29. Pair distribution functions for benzene–Ar_N clusters. Solid line: the benzene–Ar pair distribution function. Dotted line: the Ar–Ar pair distribution function.

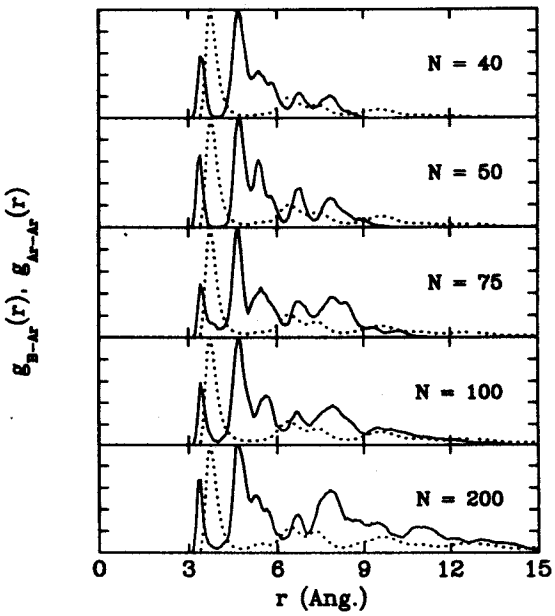

Figure 30. As in Fig. 29, but for $N = 40 \ldots 200$.

increasing cluster size. In contrast to $g_{Ar-Ar}(r)$, $g_{B-Ar}(r)$ changes dramatically with N. At $N = 40$, $g_{B-Ar}(r)$ shows an interesting combination of short-range order (note the well-defined first solvation shell) and longer-range disorder. The presence of short-range order and long-range disorder is a sign of frustration [175]. In a frustrated system (such as a spin glass [175]), a source of disorder prevents the existence of an ordered lowest-energy state. Instead, many equivalent disordered low-energy states exist. The $N = 40$ cluster also shows jump dynamics (see Section III.D). In this problem the benzene can be regarded as an impurity preventing the Ar from taking an ordered configuration. $N = 50$ has the most ordered $g_{B-Ar}(r)$, which displays several well-defined peaks. These peaks begin to fill in at $N = 75$ and $N = 100$. The first peak in $g_{B-Ar}(r)$ is at the same location for $N = 40 \ldots 200$.

We next consider how the amplitude of the vibrational motion changes as a function of N. To do this, we use the Ar–Ar RMS bond fluctuation δ_{Ar-Ar} and the B–Ar RMS bond fluctuation δ_{B-Ar} defined by

$$\delta_{Ar-Ar} = \frac{1}{N(N-1)} \sum_{i=1}^{N} \sum_{j<i} \left[\frac{\langle r_{ij}^2 \rangle_{t_a} - \langle r_{ij} \rangle_{t_a}^2}{\langle r_{ij} \rangle_{t_a}^2} \right]^{1/2}, \tag{3.9a}$$

$$\delta_{B-Ar} = \frac{1}{N} \sum_{i=1}^{N} \left[\frac{\langle r_{Bi}^2 \rangle_{t_a} - \langle r_{Bi} \rangle_{t_a}^2}{\langle r_{Bi} \rangle_{t_a}^2} \right]^{1/2}, \tag{3.9b}$$

where r_{ij} is the distance between Ar atoms i and j, and r_{Bi} is the distance between the center of mass of the benzene and Ar atom i. The expectation value in Eqs. (3.9a) and (3.9b) is defined in Eq. (2.15b). Benzene–Ar clusters can have rearrangements of the Ar atoms occurring on slow time scales, so that δ values based on a short trajectory will be smaller than those based on a longer trajectory. Previously, we have reported δ values for benzene–Ar_N clusters that are somewhat smaller than the δ values reported here [56,57]; those δ values were based on 120-psec trajectories, as opposed to the 940-psec trajectories used here.

Figure 31 shows δ_{Ar-Ar} and δ_{B-Ar} as a function of N. For $N < 40$, δ_{B-Ar} is much larger than δ_{Ar-Ar}. This is consistent with the previous observation that $g_{Ar-Ar}(r)$ was smoother than $g_{B-Ar}(r)$. The difference in the δ values means that the Ar atoms are more ordered with respect to the benzene than they are to each other. Corresponding to the spectral narrowing observed around $N = 16$ in Fig. 21, both δ_{Ar-Ar} and δ_{B-Ar} show a pronounced minimum in the neighborhood of $N = 16$. The decrease in the amplitude of the motion is the most probably cause of the spectral narrowing observed by Hahn and Whetten [46] around this N value.

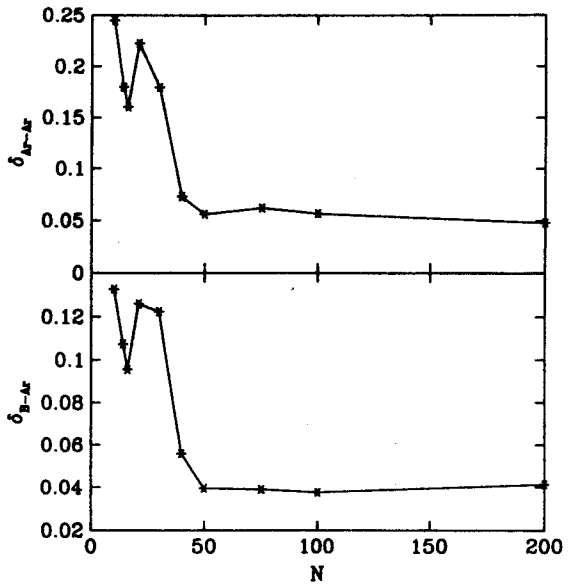

Figure 31. The benzene–Ar RMS bond fluctuation δ_{B-Ar}, and the Ar–Ar RMS bond fluctuation δ_{Ar-Ar} as a function of N.

Previous simulations which used only a 120-psec timescale [56,57] did not find the decrease in δ_{Ar-Ar} around $N = 16$. We conclude that slow ($t > 100$ psec) dynamics are less important for the $N = 16$ cluster than for the $N = 21$ cluster. The sharpening in $g_{B-Ar}(r)$ observed around $N = 50$ is reflected in a minimum of δ_{Ar-Ar}. This minimum is much more shallow than the one observed around $N = 16$. The δ values are small (around 0.05) for $N \geq 40$. This is indicative of a solid-like cluster. δ_{Ar-Ar} and δ_{B-Ar} are similar when $N \geq 40$. We conclude that benzene–Ar_N clusters undergo a transition from a phase that is ordered with respect to the benzene, but less ordered with respect to the Ar from $N = 10 \ldots 30$, to a solid-like phase that shows no significant difference in the ordering from $N = 40 \ldots 200$. δ_{Ar-Ar} and δ_{B-Ar} show a weak size dependence for $N > 40$.

Dynamical characteristics, such as δ, can ultimately be related to the potential energy surface. We consider one property of the potential energy surface here: the average potential energy per particle ($v_g \equiv \langle V_g \rangle / N$). As shown in Appendix A, v_g should approach its asymptotic value as

$$v_g(N) - v_g(N = \infty) \propto N^{-1/d}, \tag{3.10}$$

where d is the dimensionality of the cluster. In Fig. 32, we show v_g as a function of N for the calculations performed here. Also shown is a fit to the $N^{-1/3}$ scaling of v_g, based on the calculations at $N = 100$ and $N = 200$. The scaling law holds well for $N > 40$. The smooth behavior of v_g as a function of N contrasts with the dramatic fluctuations observed for the spectral shift. This is because the spectral shift is sensitive to the local benzene–Ar environment, whereas v_g is more sensitive to the Ar–Ar structure, since the number of Ar–Ar bonds is much larger than the number of B–Ar bonds. Thus, the smooth dependence of v_g is a consequence of the gradual evolution of $g_{Ar-Ar}(r)$ with N.

It is clear that the scaling law of Eq. (3.10) does not hold for the smaller cluster sizes. An alternative scaling law, however, can be derived for smaller clusters. If we assume that the Ar atoms lie in a plane on the benzene, then we predict that v_g should reach its asymptotic value as $N^{-1/2}$. The dotted line of Fig. 32 shows a fit to this scaling, based on the $N = 10$ and $N = 14$ calculations. The scaling law does a good job of predicting v_g for $N = 16$, and then breaks down as the clusters go through a crossover regime. The transition to the crossover regime is accompanied by spectral broadening (see Fig. 21). In the crossover regime, v_g oscillates as a function of N.

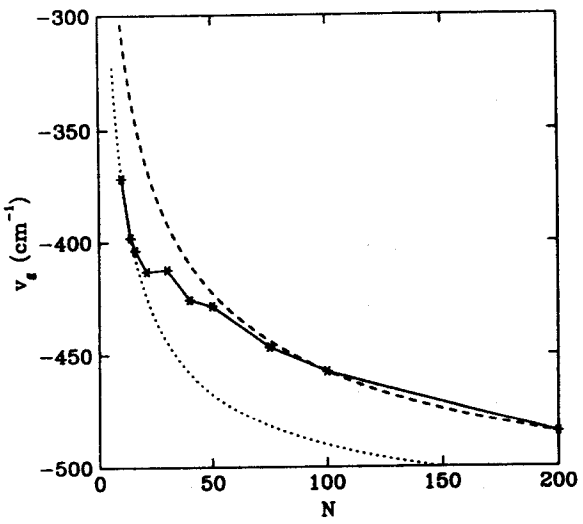

Figure 32. The average potential energy per particle (v_g), as a function of N. Calculated values are shown as symbols. The solid line is provided as a visual aid. Dashed line: asymptotic behavior of v_g based on a three-dimensional cluster [Eq. (3.10)]. Dotted line: asymptotic behavior of v_g based on a two-dimensional cluster.

There are several ways to classify clusters as two- or three-dimensional. In previous work [57], we used the term *two-dimensional* to refer to clusters that did not undergo side crossing transitions. Based on that criterion, clusters with $N \geq 10$ were found to be *three-dimensional*. Based on the scaling of v_g with N, however, we can classify clusters with $N \leq 16$ as two-dimensional. The comparable size of the benzene and an Ar atom prevents a unique definition of a two- or three-dimensional cluster.

Cluster shape is an important attribute influencing the spectroscopy of benzene–Ar clusters. For instance, a spherical cluster will have a greater spectral shift than an ellipsoidal cluster, given that the benzene occupies the same position in the cluster and that the local structure around the benzene is unchanged. The shape of a cluster can be conveniently quantified by introducing the parameter z:

$$z(t) \equiv \frac{I_{\max}(t) - I_{\min}(t)}{I_{\max}(t)} , \tag{3.11}$$

where $I_{\max}(t)$ is the maximum instantaneous moment of inertia at time t, and $I_{\min}(t)$ is the minimum instantaneous moment of inertia. While no one number can describe the shape of a cluster, $z(t)$ has the useful property of being equal to 0 for a sphere and 1 for a line of Ar atoms; it is thus reasonable to think of $z(t)$ as a measure of whether the cluster is spherical or rod-like.

In Figs. 33 and 34 we show $z(t)$ for various N values. The $N = 10$ cluster has the largest fluctuations in z. The magnitude of the fluctuations of z decreases until $N = 21$. This reflects a gradual transition to a well-defined cluster shape at $N = 21$. The decrease in the z fluctuations correlates roughly with the decrease in δ values in this size range. Note that the minimum δ value occurs at $N = 16$, whereas the minimum z fluctuations occur at $N = 21$. This serves to illustrate that different physical observables can have distinct "magic numbers." The average z value undergoes gradual changes in the range $N = 10 \ldots 200$.

The location of the benzene within the cluster is another structural property influencing spectra. In Figs. 35 and 36 we show $R(t)$, defined to be the distance of the benzene from the cluster center of mass. The $N = 10$ cluster shows the largest fluctuations in $R(t)$. $R(t)$ values are often nearly constant for a period of time, then switch to another near-constant value. The switching dynamics are probably due to isomerization processes. As N increases from 10 to 21 the benzene moves more toward the center of the cluster. For the $N = 21$ cluster the benzene is located almost exactly in the center of the cluster, and the fluctuations of $R(t)$ are small. For $N = 40 \ldots 100$, switching dynamics are not evident in $R(t)$. Between

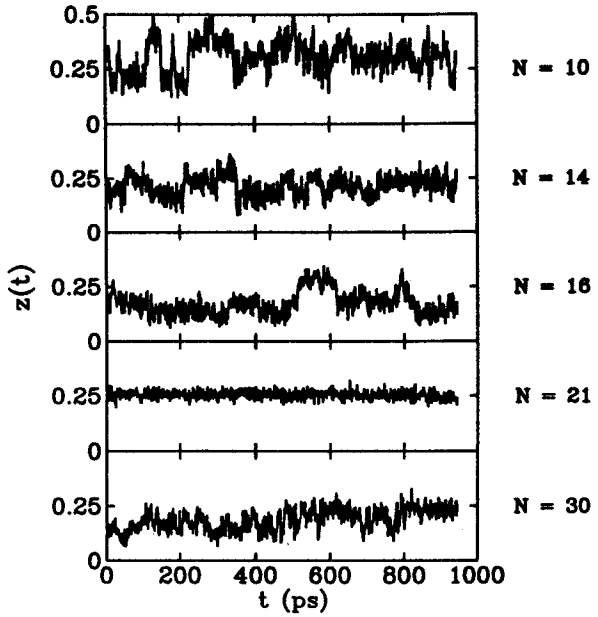

Figure 33. The cluster shape asymmetry $z(t)$ for cluster sizes $N = 10 \ldots 30$.

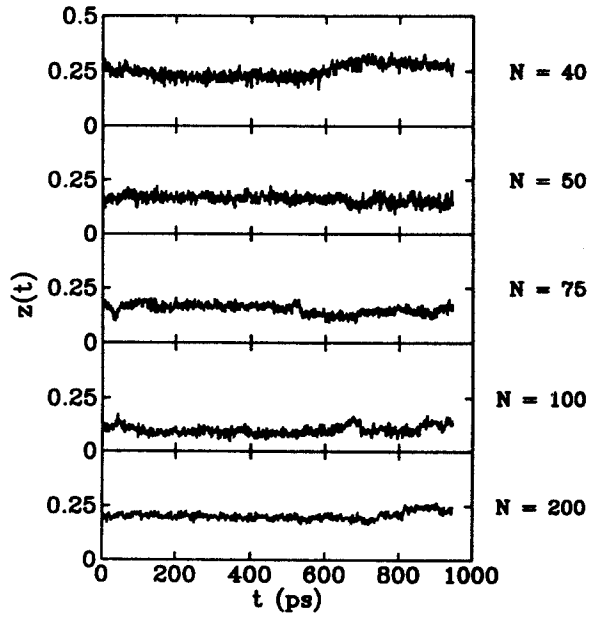

Figure 34. The cluster shape asymmetry $z(t)$ for cluster sizes $N = 40 \ldots 200$.

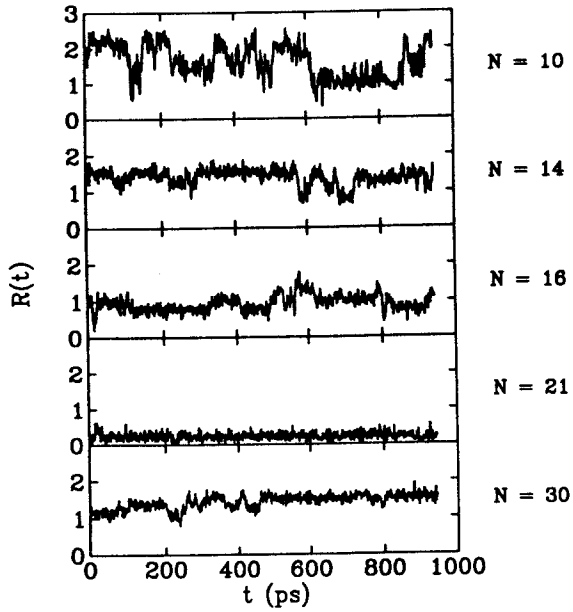

Figure 35. The distance (in angstroms) of the benzene from the center of mass of the cluster, for $N = 10 \ldots 30$.

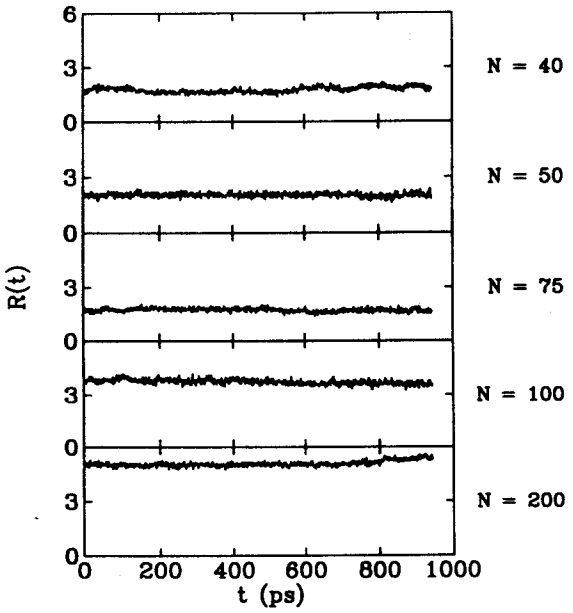

Figure 36. The distance (in angstroms) of the benzene from the center of mass of the cluster, for $N = 40 \ldots 200$.

$N = 50$ and $N = 75$, the average value of R decreases. Finally, at $N = 200$, the R value increases to about 5 Å. Several properties of large rare-gas/aromatic molecule clusters have been explained by proposing a quasi-surface location [152] of the aromatic molecule (e.g., the aromatic molecule lies one or two solvation layers below the surface of the cluster). Based on this definition, we can say that benzene–Ar_N clusters do not demonstrate quasi-surface configurations for $N \leq 100$. At $N = 200$, the benzene occupies a quasi-surface location.

Let us now summarize the conclusions of this subsection:

- The evolution of the width of the linear absorption closely follows dramatic changes in the benzene–Ar pair distribution function. The Ar–Ar pair distribution, on the other hand, shows only gradual changes with N. This underlines how the spectroscopy of rare-gas/chromophore clusters measures the local chromophore environment, rather than the overall dynamics of the cluster.
- The narrowing of the linear absorption around $N = 16$ is produced by a sharp decrease in the overall amplitude of the motion, as reflected by δ_{Ar-Ar} and δ_{B-Ar}. This decrease in the amplitude of the motion explains experimental observations of spectral narrowing in this size regime.
- The energetics of benzene–Ar_N clusters are dominated by two scaling regimes. For $N \leq 16$, v_g scales as a two-dimensional cluster, whereas for $N \geq 50$, v_g scales as a three-dimensional cluster. Scaling behavior plays a more limited role in determining $\langle U \rangle$ and Δ. The rapid changes in the benzene–Ar structure as a function of N produce large oscillations in $\langle U \rangle$ and Δ about their scaling predictions.
- The benzene is roughly in the center of the cluster for $N \leq 100$. For $N = 200$, the cluster occupies a quasi-surface position.

D. Jump Dynamics in Benzene–Ar_N Clusters

In this section we discuss an example of jump dynamics in benzene–Ar_N clusters. By jump dynamics, we mean that $U(t)$ behaves like a jump model. Microscopically, jump dynamics can occur because of slow barrier crossing events; the "jumps" are due to transitions from one potential well to another. Jump dynamics can occur in many different physical contexts [176]. Since barrier crossings (and jump dynamics) occur in the transition from small-amplitude motion to large-amplitude motion, there is a close connection between jump dynamics and phase transitions in clusters.

We have observed jump dynamics in intermediate-size ($N = 30, 40$)

benzene–Ar clusters. We consider benzene–Ar_{40} at $T = 20\ K$ here. Figure 37 shows $U(t)$ averaged over a few vibrational periods (5.6 psec) for a 3.7-nsec trajectory. This is analogous to the local averaging used by the Berry group in discussing the kinetic energy. Its purpose is to eliminate fluctuations in $U(t)$ caused by short-time dynamics, thus making the long-time trends in the dynamics of U clearer. In the bottom panel of Fig. 37 we also show a histogram of coarse-grained U values. Unlike the examples considered previously, the distribution of U is bimodal.

Jump dynamics have interesting dynamical and spectroscopic consequences. We will show the effect of jump dynamics on the linear absorption spectrum here. Figure 38 shows $I(\omega)$ calculated with the phase-averaging technique, the cumulant expansion, and the inhomogeneous cumulant expansion. The phase-averaged result shows two peaks which correspond to the two peaks in $W(U)$. The ordinary cumulant expansion predicts one peak, with an FWHM spanning the two peaks of the phase-averaged result. For the inhomogeneous cumulant calculation, the trajectory was broken up into 16 equal segments, and the absorption spectrum of each segment was added. The peak of the inhomogeneous cumulant result has a similar FWHM to the spectrum predicted by phase averaging. The smaller peak in the phase-averaged result, however, appears as a shoulder in the inhomogeneous cumulant calculation. This is because the peak of the inhomogeneous cumulant calculation appears to

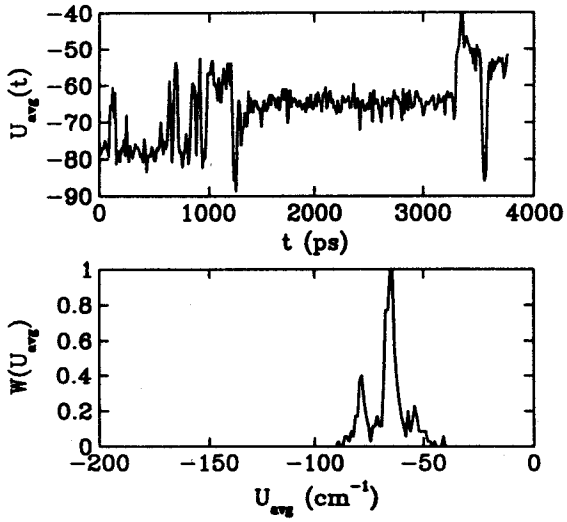

Figure 37. *Top panel:* Time-averaged U values [$U_{avg}(t)$] for benzene–Ar_{40} at 20 K. *Bottom panel:* $W(U)$.

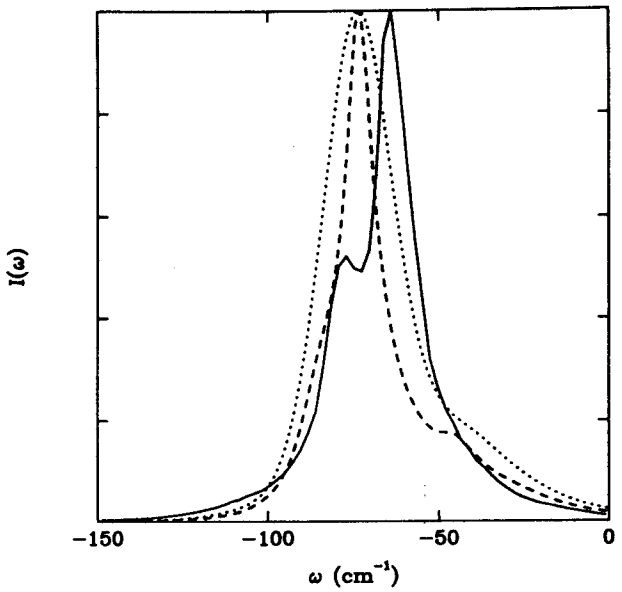

Figure 38. The normalized absorption profile $I(\omega)$ for the $N = 40$ cluster. Solid line: results of the phase-averaging technique. Dotted line: results of the cumulant approximation. Dashed line: results of the inhomogeneous cumulant approximation.

the red of the peak in the phase-averaged calculation. The shift is a consequence of the inclusion of asymmetry in the inhomogeneous cumulant calculation; when asymmetry is included, peaks tend to shift to the red. The amount of shifting depends on the magnitude of Δ, as well as dynamical factors. Here, the larger peak is shifted more than the smaller peak. In Section II.E, we have demonstrated this effect in the context of an undamped harmonic oscillator.

We can now ask which method is best in treating jump dynamics. Since jumps occur on the nanosecond timescale, it is easy to separate them from dynamics within a particular potential well. The inhomogeneous cumulant method is thus the preferred method for this problem, because it includes quantum low-temperature effects in the spectrum. If the timescale of jumping were much faster (picosecond timescale) or if the temperature were higher, the phase-averaging method would be better.

We next analyze the origin of the jump dynamics in benzene–Ar_{40}. In Fig. 39 we show $g_{B\text{-}Ar}(r)$ and $g_{Ar\text{-}Ar}(r)$ calculated along two segments of the trajectory: one segment from 0 to 1400 psec (corresponding to the segment with larger fluctuations in U), and one segment from 1400 to 3200 psec (corresponding to the segment with small fluctuations in U).

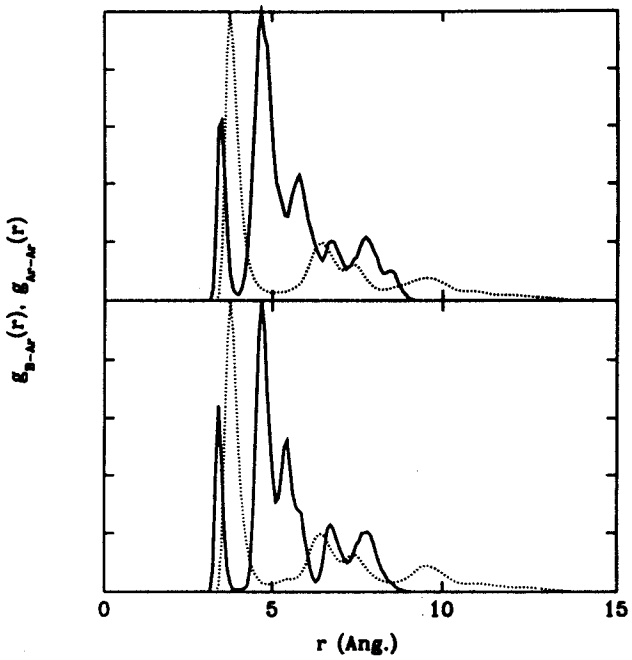

Figure 39. $g_{B-Ar}(r)$ (solid line) and $g_{Ar-Ar}(r)$ (dotted line) for two segments of the trajectory shown in Fig. 37. *Top panel:* $g(r)$ for the segment from 0 to 1400 psec is shown. *Bottom panel:* $g(r)$ for the segment from 1400 to 3200 psec. The results are indicative of *shell-specific melting*.

$g_{Ar-Ar}(r)$ is very similar in both cases. Thus, changes in the Ar–Ar structure are not producing the jumps in U. There are fascinating changes, however, in $g_{B-Ar}(r)$. The first peak of $g_{B-Ar}(r)$ is nearly the same in the two segments. Beyond the first peak, however, the peaks of $g_{B-Ar}(r)$ are much broader in the first segment than in the second. The most dramatic difference appears in the third minimum of $g_{B-Ar}(r)$. The second segment has a minimum near zero, which is indicative of a solid-like cluster. The first segment, on the other hand, has a minimum well above zero, which is indicative of a liquid-like cluster.

In conclusion, we have found that jump dynamics in $U(t)$ can occur in intermediate-sized clusters ($N = 30 \ldots 40$). We have run long trajectories on smaller benzene–Ar_N clusters, but have not observed any jump dynamics. Jump dynamics are responsible for a peak + shoulder structure in the absorption spectrum. The physical cause of the jump dynamics is a *shell-specific melting* phenomenon.

APPENDIX A. SCALING OF SPECTROSCOPIC AND ENERGETIC QUANTITIES WITH N

In this section we give some simple scaling laws for quantities relevant to the spectroscopy and dynamics of benzene–Ar_N clusters. The spirit of the treatment is to take into account only dimensionality and the long-range behavior of the potential function. Of course, other factors, such as short-range structure, can play a role in determining spectroscopic quantities. The results presented here can be regarded as a reference that allows structural effects to be distinguished from simpler finite size effects, such as the ratio of volume to surface area.

We first study the mean potential energy per particle on the ground-state potential energy surface (v_g). Let us say that the potential energy of an Ar inside the cluster is v_i, whereas the potential energy of an Ar atom on the surface of the cluster is v_s. Then

$$v_g = (1 - cN^{-1/d})v_i + cN^{-1/d}v_s \,, \tag{A.1}$$

where c is a factor depending on cluster shape, and d is the dimensionality of the cluster. This immediately gives Eq. (3.10). For small N, benzene–Ar_N clusters are expected to be effectively two-dimensional, since the Ar atoms will lie along the plane of the benzene. For larger N, benzene–Ar_N clusters will become three-dimensional.

Next we consider the behavior of $\langle U \rangle$ and Δ as a function of N. In the following discussion, we make the simplifying assumption that U [see Eq. (2.17)] only depends on the distance of the solvent atom from the chromophore atom (and not on orientation with respect to the chromophore). Let us introduce the instantaneous density of solvent atoms $\rho(\mathbf{r}, t)$:

$$\rho(\mathbf{r}, t) \equiv \sum_i \delta(\mathbf{r} - \mathbf{Q}_i) \,, \tag{A.2}$$

where $\mathbf{Q}_i$ is the position of atom i, and the center of mass of the chromophore is at $\mathbf{r} = 0$. We have

$$U(t) = \int d\mathbf{r}\, U(|\mathbf{r}|)\rho(\mathbf{r}, t) \,, \tag{A.3}$$

which leads to

$$\langle U(t) \rangle_\infty \propto \int_0^\infty U(r)\bar{\rho}(r)r^{d-1}\, dr \,, \tag{A.4}$$

where $\langle \cdots \rangle_\infty$ is defined in Eq. (2.15c), and $\bar{\rho}(r) = \langle \rho(\mathbf{r}, t) \rangle_\infty$. We also assume that $\bar{\rho}(r)$ is uniform when r is greater than a cutoff radius r_0 and less than the cluster radius r_M: $\bar{\rho}(r) = c\theta(r - r_0)\theta(r_M - r)$, where c is a constant and θ is the Heaviside function. This gives Eq. (3.3), once we set $r_M \propto N^{1/d}$ and $U \propto r^{-m}$.

We next consider the scaling of Δ^2, the magnitude of the fluctuations of U, with N. Thus, we must find $\langle U(t)^2 \rangle_\infty - \langle U(t) \rangle_\infty^2$. We have

$$\langle U^2 \rangle_\infty = \left\langle \left[\int d\mathbf{r}\, \rho(\mathbf{r}, t) U(r)\, d\mathbf{r} \right]^2 \right\rangle_\infty . \tag{A.5}$$

Dividing $\rho(\mathbf{r}, t)$ up into its average value and a fluctuation [namely, $\rho(\mathbf{r}, t) = \bar{\rho}(r) + \delta\rho(\mathbf{r}, t)$] then leads to

$$\Delta^2 = \int d\mathbf{r}\, d\mathbf{r}'\, U(r)U(r') \langle \delta\rho(\mathbf{r}, t)\delta\rho(\mathbf{r}', t) \rangle_\infty . \tag{A.6}$$

We will assume that the fluctuations in $\delta\rho(\mathbf{r}, t)$ are due to uncorrelated motion of each atom, and that the amplitude of fluctuation does not depend on location in the cluster. Thus,

$$\langle \delta\rho(\mathbf{r}, t)\delta\rho(\mathbf{r}', t) \rangle_\infty = c'\delta(\mathbf{r} - \mathbf{r}')\theta(r - r_0)\theta(r_M - r) . \tag{A.7}$$

Doing the integral in Eq. (A.6) then gives Eq. (3.4). This result can immediately be extended to the photon echo decay time. Assuming a Bloch-like photon echo decay (which was observed in the above calculations for large N), we have $t_{PE} \propto 1/\tau\Delta^2$, where τ is the decay time of $C(t)$. In the above calculations, we found that this decay time was fairly insensitive to N when $N > 30$. This motivates the assumption that τ is independent of N, giving the scaling law of Eq. (3.8).

APPENDIX B. ANALYTICAL RESULTS FOR MODEL PROBLEMS

We discuss two model problems here: the two-state jump model and the undamped displaced harmonic oscillator [Eq. (2.37b)]. First we show that the second-order cumulant expansion is exact for the displaced harmonic oscillator model. The analytic solution for $I(\omega)$ is [41]

$$I(\omega') = \exp[-d^2(\bar{n} + \tfrac{1}{2})] \sum_{N=-\infty}^{\infty} \exp[N\omega/2kT] , \tag{B.1}$$

$$I_N[d^2\sqrt{\bar{n}(\bar{n}+1)}]\, \frac{\gamma}{(\omega' - N\omega - \omega_{eg})^2 + \gamma^2} ,$$

where γ is the experimental resolution, I_N is the modified Bessel function [177], and ω is the frequency of the oscillator. $\bar{n}$ is defined in Eq. (2.1).

A simpler form exists for $J(t)$ [41,178]:

$$J(t) = \exp[-\gamma t - g(t)] , \tag{B.2a}$$

$$g(t) = i\omega_{eg}t + \frac{d^2}{2}[(2\bar{n}+1)\cos(\omega t) + i(\sin\omega t - \omega t)] . \tag{B.2b}$$

The second-order cumulant expansion predicts that

$$g(t) = i\langle U\rangle t + \int_0^t dt' \int_0^{t'} dt'' \, C(t'') . \tag{B.3}$$

$C(t)$ is defined in Eq. (2.16). The classical autocorrelation function of U is equal to

$$C_c(t) = \Delta^2 \cos(\omega t) , \tag{B.4}$$

$$C_c(\omega') = \frac{\Delta^2}{2}[\delta(\omega+\omega') + \delta(\omega-\omega')] , \tag{B.5}$$

where Δ is defined in Eq. (2.44). Applying the fluctuation–dissipation correction to Eq. (B.5) then yields the exact result Eq. (B.2b), once the relations

$$1 + \tanh(-\omega/2kT) = \frac{\bar{n}}{\bar{n}+1/2} \tag{B.6}$$

$$1 + \tanh(\omega/2kT) = \frac{\bar{n}+1}{\bar{n}+1/2} \tag{B.7}$$

are used.

We next apply the phase-averaging method to the displaced harmonic oscillator system. The formula for $I(\omega)$ predicted by the phase-averaging technique is given in Eq. (2.32). U for the displaced harmonic oscillator system is equal to

$$U(q) = qd\omega . \tag{B.8}$$

Using the equation of motion $q(t) = q_0\cos(\omega t) + p_0\sin(\omega t)$ yields

$$J(t) = e^{-i\omega_{eg}t}\int dp_0 \, dq_0 \exp\{i\omega d[q_0\sin\omega t - p_0(\cos\omega t - 1)]\}\rho(q_0, p_0) , \tag{B.9}$$

where $\rho(q_0, p_0)$ is the Wigner function of the harmonic oscillator:

$$\rho(q_0, p_0) = \exp\left(-\frac{q^2 + p^2}{2\bar{n} + 1}\right). \tag{B.10}$$

The integral over q_0 and p_0 in Eq. (B.9) can be done by completing the square, giving

$$J(t) \propto \exp[-i\omega_{eg}t - d^2(2\bar{n} + 1)(1 - \cos \omega t)]. \tag{B.11}$$

Comparing this with Eq. (B.2b), we see that phase averaging correctly reproduces the real part of $g(t)$. The imaginary part of $g(t)$ is quantum mechanical in origin for a displaced harmonic oscillator system and is thus missed by the classical phase-averaging technique. In general, the imaginary part of $g(t)$ contains both classical and quantum mechanical contributions. Phase averaging neglects the quantum contributions.

We next consider the extent to which multiple trajectory averages can be replaced by a single long trajectory in the cumulant and phase-averaging technique. This is an interesting practical question, because averaging over many trajectories is more computationally difficult than using a single trajectory. It is easy to show that the cumulant technique can give the exact result with a single trajectory, if that trajectory is chosen to have energy $E = (\bar{n} + \frac{1}{2})\omega$. We next consider phase averaging. Averaging over a long trajectory is the same as averaging over a single period of the oscillator. Thus, we want to calculate

$$I_T(t; q_0, p_0) = \frac{\omega}{2\pi} \int_0^{2\pi/\omega} dt_0 \exp\left[i \int_{t_0}^{t+t_0} dt' \, U(t; q_0, p_0)\right], \tag{B.12}$$

where the T subscript denotes time averaging. It is easy to show that

$$\int_{t_0}^{t_0+t} U(t'; q_0, p_0) \, dt' = a \cos \omega t_0 + b \sin \omega t_0, \tag{B.13}$$

where

$$a = d[q_0 \sin \omega t - p_0(\cos \omega t - 1)], \tag{B.14}$$

$$b = d[q_0(\cos \omega t - 1) + p_0 \sin \omega t]. \tag{B.15}$$

Using these results, I_T now reads:

$$I_T(t) = \frac{1}{2\pi}\int_0^{2\pi} dt_0 \exp[ia\cos t_0 + ib\sin t_0]\,. \tag{B.16}$$

This can be further simplified by writing $a\cos t_0 + b\sin t_0 = c\cos(t_0+\alpha)$. Since the integral is over one full period, it does not depend on α. We then have that $c = 2d[(E/\omega)(1-\cos\omega t)]^{1/2}$, where $E = (\omega/2)(p_0^2+q_0^2)$. Using this transformation reduces the integral to

$$I_T(t) = \frac{1}{2\pi}\int_0^{2\pi} dt_0 \cos[c\cos t_0] + i\sin[c\cos t_0]\,. \tag{B.17}$$

The first term in Eq. (B.17) is an integral representation of the Bessel function of the first kind (J_0). The second term is equal to zero. This gives

$$I_T(t) = J_0\left\{2d\left[\frac{E}{\omega}(1-\cos\omega t)\right]^{1/2}\right\}. \tag{B.18}$$

Phase averaging does not exactly reproduce either the real or the imaginary part of $g(t)$ unless multiple trajectories are used. We can still ask, however, what energy is optimal for a single trajectory phase-averaging calculation. The nth moment of $I(\omega)$ is proportional to the nth derivative of $I(t)$ evaluated at $t=0$. The first moment of $I(\omega)$ is the same for the single trajectory phase average and the exact result [Eq. (B.2b)]:

$$\frac{d}{dt}J(t)|_{t=0} = -i\omega_{eg}\,. \tag{B.19}$$

We next find the second moment of $I(\omega)$. Equation (B.2b) gives us

$$\frac{d^2}{dt^2}J(t)|_{t=0} = -(\bar{n}+\tfrac{1}{2})d^2\omega^2\,, \tag{B.20}$$

whereas Eq. (B.18) gives us

$$\frac{d^2}{dt^2}I_T(t)|_{t=0} = -\omega d^2 E\,. \tag{B.21}$$

The two results agree if we choose $E = (\bar{n}+\frac{1}{2})\omega$. The optimal choice of energy is the same for single-trajectory cumulant and phase-averaging calculations. While the single-trajectory cumulant result is exact, the single-trajectory phase-averaging result is approximate. This analysis represents a worst-case scenario for single-trajectory phase averaging.

Ergodic systems with many degrees of freedom should show little difference between microcanonical and canonical phase-averaging results.

We next study the spectrum of the two-state jump model. In this model, $U(t)$ jumps between values ω_1 and $-\omega_1$ with a hopping rate equal to $\gamma/2$. Kubo's result for this model is that [59]

$$I(\omega) = \frac{1}{\pi} \frac{\omega_1^2}{(\omega^2 - \omega_1^2)^2 + \omega^2\gamma^2} . \tag{B.22}$$

Phase averaging gives the same result, because the phase-averaging formula for linear absorption is essentially a microscopic implementation of the stochastic model. We can also apply the second-order cumulant approximation to this model. The correlation function of U is

$$\langle U(t)U(0)\rangle = \omega_1^2 \exp(-\gamma t) , \tag{B.23}$$

which gives

$$I(t) = \exp\left[- \frac{\omega_1^2}{\gamma^2} (e^{-\gamma t} - 1 + \gamma t)\right] \tag{B.24}$$

when $k_B T \gg \gamma$. This is the same result that the cumulant approximation predicts for an overdamped oscillator. The cumulant result always has a single peak around $\omega = 0$, while the exact result interpolates between a two-peaked structure at small γ to a single-peaked structure at large γ. At large γ and high temperature, the cumulant approximation gives a good approximation to the spectrum near $\omega = 0$, but does not predict the correct wings of the spectrum. In the low-temperature limit, the cumulant approximation incorrectly predicts an asymmetry in the absorption lineshape about $\omega = 0$.

APPENDIX C. HARMONIC REFERENCE MODEL

The primary limitation of purely classical simulation methods is that quantum effects due to vibrational quantization are neglected. We take the approach here of using a *harmonic reference system* to add quantum effects *a posteriori* to our classical simulations.

The reference model is an infinite set of displaced harmonic oscillators:

$$H_g = \int_0^\infty d\omega\, W(\omega) \frac{\omega}{2} (\mathbf{p}[\omega]^2 + \mathbf{q}[\omega]^2) ,$$

$$H_e = \omega_{eg} + \int_0^\infty d\omega\, W(\omega) \frac{\omega}{2} (\mathbf{p}[\omega]^2 + \mathbf{q}[\omega]^2 + 2d(\omega)\mathbf{q}[\omega]) . \tag{C.1}$$

Here, $W(\omega)$ is the probability density of oscillators. $\mathbf{p}[\omega]$ and $\mathbf{q}[\omega]$ are infinite-dimensional vectors parameterized by the continuous index ω. $d(\omega)$ is a function giving the displacement of an oscillator with frequency ω. Equation (2.37b) is a limiting case of Eq. (C.1) when $W(\omega) = \Sigma_j \delta(\omega - \omega_j)$.

Our task here is to derive relations which relate the classical autocorrelation of U [Eqs. (2.29) and (2.26a)] to $C(t)$. For the reference model we have

$$C_s(\omega) = W(\omega)d^2(\omega)^2(\bar{n} + \tfrac{1}{2}) . \tag{C.2}$$

A classical calculation gives

$$C_c(\omega) = W(\omega)d^2(\omega)|\omega|k_B T . \tag{C.3}$$

Equations (C.2) and (C.3) result in Eq. (2.27).

ACKNOWLEDGMENT

The support of the National Science Foundation and the Air Force Office of Scientific Research is gratefully acknowledged.

REFERENCES

1. R. W. Hellwarth, *Proc. Quant. Elect.* **5**, 1 (1977).
2. D. Frenkel and J. P. McTague, *J. Chem. Phys.* **72**, 2801 (1980).
3. B. M. Ladanyi, *J. Chem. Phys.* **78**, 2189 (1983).
4. P. A. Madden and D. J. Tildesley, *Mol. Phys.* **55**, 969 (1985).
5. P. A. Madden and T. I. Cox, *Mol. Phys.* **56**, 223 (1985).
6. P. A. Madden and R. W. Impey, *Chem. Phys. Lett.* **123**, 502 (1986).
7. M. Evans, G. J. Evans, W. T. Coffey, and P. Grigolini, *Molecular Dynamics and Theory of Broad Band Spectroscopy*, John Wiley & Sons, New York, 1982.
8. B. J. Berne and G. D. Harp, *Adv. Chem. Phys.* **17**, 63 (1970).
9. R. G. Gordon, *J. Chem. Phys.* **45**, 1643 (1966); *ibid* **45**, 1649 (1966).
10. I. C. Percival, *Adv. Chem. Phys.* **36**, 1 (1977).
11. D. W. Noid, M. L. Koszykowski, and R. A. Marcus, *Annu. Rev. Phys. Chem.* **31**, 267 (1981).
12. M. V. Berry, in *Chaotic Behavior of Deterministic Systems*, I. Gérard, R. H. G. Helleman, and R. Stora, Eds., North-Holland, Amsterdam, 1983.
13. E. B. Stechel and E. J. Heller, *Annu. Rev. Phys. Chem.* **35**, 563 (1984).
14. R. G. Littlejohn, *Phys. Rep.* **138**, 193 (1986).
15. S. Mukamel, *J. Phys. Chem.* **89**, 1077 (1985).

16. R. J. D. Miller, R. Casalegno, K. A. Nelson, and M. D. Fayer, *Chem. Phys.* **72**, 371 (1982).
17. A. B. Myers and R. M. Hochstrasser, *IEEE J. Quant. Elect.* **22**, 1482 (1986).
18. M. Dantus, M. J. Rosker, and A. H. Zewail, *J. Chem. Phys.*, **87**, 2395 (1987).
19. G. R. Fleming, G. R. Martin, and J. L. Bretan, *Nature* **333**, 190 (1988).
20. R. A. Mathies, C. H. Brito-Cruz, W. T. Pollard, and C. V. Shank, *Science* **240**, 777 (1988).
21. P. F. Barbara and W. Jarzeba, *Acc. Chem. Res.* **21**, 195 (1988).
22. J. D. Simon, *Acc. Chem. Res.* **21**, 128 (1988).
23. K. A. Nelson and E. P. Ippen, *Adv. Chem. Phys.* **75**, 1 (1989).
24. F. H. Long, H. Lu, and K. B. Eisenthal, *J. Chem. Phys.* **91**, 4413 (1989).
25. B. I. Greene, J. Orenstein, and S. Schmitt-Rink, *Science* **247**, 679 (1990).
26. D. McMorrow and W. T. Lotshaw, *Chem. Phys. Lett.* **178**, 69 (1991).
27. D. Vanden Bout, L. J. Muller, and M. Berg, *Phys. Rev. Lett.* **67**, 3700 (1991).
28. C. B. Harris, E. P. Ippen, G. A. Mourou, and A. H. Zewail, Eds., *Ultrafast Phenomena VII*, Springer-Verlag, Berlin, 1990.
29. Y. R. Shen, *The Principles of Nonlinear Optics*, John Wiley & Sons, New York, 1984.
30. M. D. Levenson, *Introduction to Nonlinear Laser Spectroscopy*, Academic Press, New York, 1982.
31. S. Mukamel, *Adv. Chem. Phys.* **70**, 165 (1988).
32. S. Mukamel, *Annu. Rev. Phys. Chem.* **41**, 647–681 (1990).
33. C. H. Brito-Cruz, R. L. Fork, W. H. Knox, and C. V. Shank, *Chem. Phys. Lett.* **132**, 341 (1986).
34. I. Lee, J. M. Hayes, and G. J. Small, *J. Chem. Phys.* **91**, 3463 (1989).
35. H. A. Ferwerda, J. Terpstra, and D. A. Wiersma, *J. Chem. Phys.* **91**, 3296 (1989).
36. S. Kinoshita, H. Itoh, H. Murakami, H. Miyasaka, T. Okada, and N. Mataga, *Chem. Phys. Lett.* **166**, 123 (1990).
37. W. B. Bosma, S. Mukamel, B. I. Greene, and S. Schmitt-Rink, *Phys. Rev. Lett.* **68**, 2456 (1992).
38. D. A. Wiersma and W. H. Hesselink, *Phys. Rev. Lett.* **43**, 1991 (1979).
39. W. H. Hesselink and D. A. Wiersma, *J. Chem. Phys.* **75**, 4192 (1981).
40. P. C. Becker, H. L. Fragnito, J. Y. Bigot, C. H. Brito-Cruz, and C. V. Shank, *Phys. Rev. Lett.* **63**, 505 (1989).
41. S. Mukamel, *J. Chem. Phys.* **77**, 173 (1982).
42. L. E. Fried and G. S. Ezra, *J. Phys. Chem.* **92**, 3144 (1988).
43. Strictly speaking, the origin of the singularity is the presence of a quantum degree of freedom with kT much smaller than its characteristic energy. Similar singularities are found when applying semiclassical techniques to the IR spectra of small isolated molecules at low temperatures. In practice, electronic optical transitions are of interest in the low-temperature limit.
44. Y. J. Yan and S. Mukamel, *J. Chem. Phys.* **88**, 5735 (1988).
45. Y. J. Yan and S. Mukamel, *J. Chem. Phys.* **89**, 5160 (1988).
46. M. Y. Hahn and R. L. Whetten, *Phys. Rev. Lett.* **61**, 1190 (1988).
47. H. L. Fragnito, J. Y. Bigot, P. C. Becker, and C. V. Shank, *Chem. Phys. Lett.* **160**, 101 (1989).

48. A. Abragam, *The Principles of Nuclear Magnetism*, Clarendon, Oxford, 1961.
49. R. Loudon, *The Quantum Theory of Light*, Oxford University Press, London, 1983.
50. J. Y. Bigot, M. T. Portella, R. W. Schoenlein, C. J. Bardeen, A. Migus, and C. V. Shank, *Phys. Rev. Lett.* **66**, 1138 (1991).
51. E. T. J. Nibbering, D. A. Wiersma, and K. Duppen, *Phys. Rev. Lett.* **66**, 2464 (1991).
52. R. F. Loring and S. Mukamel, *Chem. Phys. Lett.* **114**, 426 (1985).
53. R. F. Loring and S. Mukamel, *J. Chem. Phys.* **83**, 2116 (1985).
54. S. Mukamel and R. F. Loring, *J. Opt. Soc. Am. B* **3**, 595 (1986).
55. J. S. Bader and D. Chandler, *Chem. Phys. Lett.* **157**, 501 (1989).
56. L. E. Fried and S. Mukamel, *Phys. Rev. Lett.* **66**, 2340 (1991).
57. L. E. Fried and S. Mukamel, *J. Chem. Phys.* **96**, 116 (1992).
58. N. Bloembergen, N. Purcell, and R. V. Pound, *Phys. Rev.* **73**, 679 (1948).
59. R. Kubo, *Adv. Chem. Phys.* **15**, 101 (1969).
60. Y. X. Yan, L. T. Chang, and K. A. Nelson, in *Advances in Nonlinear Spectroscopy*, R. J. H. Clark and R. E. Hester, Eds., John Wiley & Sons, New York, 1988, p. 299.
61. N. F. Scherer, A. Ruggiero, M. Du, and G. R. Fleming, *J. Chem. Phys.* **93**, 856 (1990).
62. N. F. Scherer, R. J. Carlson, A. Matro, M. Du, A. J. Ruggiero, V. Romero-Rochin, J. A. Cina, G. R. Fleming, and S. A. Rice, *J. Chem. Phys.* **95**, 1487 (1991).
63. N. F. Scherer, A. Matro, L. D. Ziegler, M. Du, R. J. Carlson, J. A. Cina, and G. R. Fleming, *J. Chem. Phys.* **96**, 4180 (1992).
64. Y. J. Yan, R. M. Wintell, K. R. Wilson, and A. H. Zewail, *Chem. Phys. Lett.* **193**, 402 (1992).
65. Y. J. Yan and S. Mukamel, *J. Chem. Phys.* **94**, 179 (1991).
66. M. Maroncelli and G. R. Fleming, *J. Chem. Phys.* **89**, 875 (1988).
67. P. F. Barbara and W. Jarzeba, *Acc. Chem. Res.* **21**, 195 (1988).
68. L. E. Fried and S. Mukamel, *J. Chem. Phys.* **93**, 932 (1990).
69. J. Sue, Y. J. Yan, and S. Mukamel, *J. Chem. Phys.* **85**, 462 (1986).
70. Z. Deng and S. Mukamel, *J. Chem. Phys.* **85**, 1738 (1986).
71. J. Sue, S. Mukamel, H. Okamoto, H. Hamaguchi, and M. Tasumi, *Chem. Phys. Lett.* **134**, 87 (1987).
72. L. E. Fried, N. Berstein, and S. Mukamel, *Phys. Rev. Lett.* **68**, 1842 (1992).
73. E. B. Wilson, J. C. Decius, and P. C. Cross, *Molecular Vibations*, Dover, New York, 1955.
74. G. Seeley and T. Keyes, *J. Chem. Phys.* **91**, 5581 (1989).
75. J. E. Adams and R. M. Stratt, *J. Chem. Phys.* **93**, 1358 (1990).
76. J. E. Adams and R. M. Stratt, *J. Chem. Phys.* **93**, 1332 (1990).
77. M. Lee, J. W. Haseltine, A. B. Smith, and R. M. Hochstrasser, *J. Am. Chem. Soc.* **111**, 4563 (1989).
78. S. Abrash, S. Repinec, and R. M. Hochstrasser, *J. Chem. Phys.* **93**, 1041 (1990).
79. W. T. Pollard, C. H. Cruz, C. V. Shank, and R. A. Mathies, *J. Chem. Phys.* **90**, 199 (1989).
80. P. R. Weiss and P. W. Anderson, *Rev. Mod. Phys.* **25**, 269 (1953).
81. P. G. Wolynes, *J. Chem. Phys.* **86**, 5133 (1987).

82. D. Chandler, in *Liquids, Freezing and Glass Transitions*, D. Levesque, J. P. Hansen, and J. Zinn-Justin, Eds., Elsevier, Amsterdam, 1990.
83. R. A. Marcus and N. Sutin, *Biochim. Biophys. Acta* **811**, 265 (1985).
84. W. A. Phillips, *Amorphous Solids; Low Temperature Properties*, Springer-Verlag, New York, 1981.
85. R. Jankowiak and G. J. Small, *Science* **237**, 618 (1987).
86. M. Berg, C. A. Walsh, L. R. Narasimhan, K. A. Littau, and M. D. Fayer, *J. Chem. Phys.* **88**, 1564 (1988).
87. S. Volker, *Annu. Rev. Phys. Chem.* **40**, 499 (1989).
88. C. Amitrano and R. S. Berry, *Phys. Rev. Lett.* **68**, 729 (1992).
89. Y. J. Yan and S. Mukamel, *Phys. Rev. A* **41**, 6485 (1990).
90. M. Cho, N. F. Scherer, G. R. Fleming, and S. Mukamel, *J. Chem. Phys.* **96**, 5618 (1992).
91. C. M. Bender and S. A. Orszag, *Advanced Mathematical Methods for Scientists and Engineers*, McGraw–Hill, New York, 1978.
92. N. Bloembergen, *Nonlinear Optics*, John Wiley & Sons, New York, 1965.
93. U. Fano, *Phys. Rev.* **131**, 259 (1963).
94. R. Zwanzig, *Physica* **30**, 1109 (1964).
95. A. Ben Reuven, *Adv. Chem. Phys.* **33**, 235 (1975).
96. S. Mukamel, *Phys. Rep.* **93**, 1 (1982).
97. S. Mukamel, *Adv. Chem. Phys.* **70**, 165 (1988).
98. M. Hillery, R. F. O'Connell, M. O. Scully, and E. P. Wigner, *Phys. Rep.* **106**, 121 (1984).
99. Y. J. Yan and S. Mukamel, *J. Chem. Phys.* **94**, 179 (1991).
100. S. Mukamel, *Phys. Rev. A* **28**, 3480 (1983).
101. N. Balazs and B. Jennings, *Phys. Rep.* **104**, 347 (1984).
102. W. H. Press, B. P. Flannery, S. A. Teukolsky, and W. T. Vetterling, *Numerical Recipes*, Cambridge University Press, London, 1986.
103. M. P. Allen and D. J. Tildesley, *Computer Simulation of Liquids*, Oxford University Press, London, 1987.
104. A. Einstein, *Archives de Sciences Physiques et Naturelles*, **37**, 254 (1914). [Reproduced in IEEE ASSP Magazine, **4**, 6 (1987).]
105. D. Lu and W. L. Hase, *J. Chem. Phys.* **91**, 7490 (1989).
106. J. M. Bowman, B. Gazdy, and Q. Sun, *J. Chem. Phys.* **91**, 2859 (1989).
107. R. Alimi, A. García-Vela, and R. B. Gerber, *J. Chem. Phys.* **96**, 2034 (1992).
108. L. E. Fried and S. Mukamel, *J. Chem. Phys.* **93**, 3063 (1990).
109. A. M. Walsh and R. F. Loring, *J. Chem. Phys.* **94**, 7575 (1991).
110. N. E. Shemetulskis and R. F. Loring, *J. Chem. Phys.* **95**, 4756 (1991).
111. R. F. Loring, Y. J. Yan, and S. Mukamel, *J. Chem. Phys.* **87**, 5840 (1987).
112. N. G. Van Kampen, *Stochastic Processes in Physics and Chemistry*, North-Holland, Amsterdam, 1981.
113. B. Berne, J. Jortner, and R. G. Gordon, *J. Chem. Phys.* **47**, 1600 (1967).
114. J. Borysow, M. Moraldi, and L. Frommhold, *Mol. Phys.* **56**, 913 (1985).
115. R. P. Feynman, F. L. Vernon, and R. W. Hellwarth, *J. Appl. Phys.* **28**, 49 (1957).

116. Alternatively, a continued fraction expansion of the lineshape in the frequency domain is adequate for jump dynamics. See S. Mukamel, *Chem. Phys.* **31**, 327 (1978).
117. M. Lax, *J. Chem. Phys.* **20**, 1752 (1952).
118. A. A. Gordus and R. B. Bernstein, *J. Chem. Phys.* **22**, 790 (1954).
119. B. Cichocki and B. U. Felderhof, *J. Chem. Phys.* **90**, 4960 (1989).
120. K. Ganguly and R. M. Stratt, *J. Chem. Phys.* **95**, 4418 (1991).
121. I. Benjamin and K. R. Wilson, *J. Phys. Chem.*, **90**, 4176 (1989).
122. A. Wallqvist, G. Martyna, and B. J. Berne, *J. Phys. Chem.* **92**, 1721 (1988).
123. P. J. Rossky and J. Schnitker, *J. Phys. Chem.* **92**, 4277 (1988).
124. F. A. Webster, J. Schnitker, M. S. Friedrichs, R. A. Friesner, and P. J. Rossky, *Phys. Rev. Lett.* **66**, 3172 (1991).
125. M. J. Rosker, M. Dantus, and A. H. Zewail, *Science* **241**, 1200 (1988).
126. M. J. Rosker, M. Dantus, and A. H. Zewail, *J. Chem. Phys.* **89**, 6113 (1988).
127. M. Dantus, M. J. Rosker, and A. H. Zewail, *J. Chem. Phys.* **89**, 6128 (1988).
128. R. Bersohn and A. H. Zewail, *Ber. Bunsenges Phys. Chem.* **92**, 373 (1988).
129. R. B. Bernstein and A. H. Zewail, *J. Chem. Phys.* **90**, 829 (1989).
130. W. B. Bosma, Y. J. Yan, and S. Mukamel, *Phys. Rev. A* **42**, 6920 (1990).
131. P. C. Becker, R. L. Fork, C. H. Brito-Cruz, J. P. Gordon, and C. V. Shank, *Phys. Rev. Lett.* **60**, 2462 (1988).
132. M. J. Rosker, F. W. Wise, and C. L. Tang, *Phys. Rev. Lett.* **57**, 321 (1986).
133. F. W. Wise, M. J. Rosker, and C. L. Tang, *J. Chem. Phys.* **86**, 2827 (1987).
134. S. Ruhman, A. G. Joly, and K. A. Nelson, *J. Chem. Phys.* **86**, 6563 (1987).
135. A. M. Weiner and E. P. Ippen, *Chem. Phys. Lett.* **114**, 456 (1985).
136. J. Chesnoy and A. Mokhtari, *Phys. Rev. A* **38**, 3566 (1988).
137. M. Cho, S. J. Rosenthal, N. F. Scherer, L. D. Ziegler, and G. R. Fleming, *J. Chem. Phys.* **96**, 5033 (1992).
138. N. F. Scherer, L. D. Ziegler, and G. R. Fleming, *J. Chem. Phys.* **96**, 5544 (1992).
139. S. Kirkpatrick, C. D. Gelatt, and M. P. Vecchi, *Science* **220**, 671 (1983).
140. S. Kirkpatrick, *J. Stat. Phys.* **34**, 975 (1984).
141. C. L. Tang, F. W. Wise, and I. A. Walmsley, *J. Mod. Opt.* **35**, 1939 (1988).
142. S. M. Kay and S. L. Marple, *Proc. IEEE* **69**, 1380 (1981).
143. M. L. Alexander, M. A. Johnson, N. E. Levinger, and W. C. Lineberger, *Phys. Rev. Lett.* **57**, 976 (1986).
144. J. Bösiger and S. Leutwyler, *Phys. Rev. Lett.* **59**, 1895 (1987).
145. S. Wuelfert, D. Herren, and S. Leutwyler, *J. Chem. Phys.* **86**, 3751 (1987).
146. U. Even, N. Ben-Horin, and J. Jortner, *Chem. Phys. Lett.* **156**, 138 (1989).
147. U. Even, N. Ben-Horin, and J. Jortner, *Phys. Rev. Lett.* **62**, 140 (1989).
148. G. Rajagopal, R. Barnett, A. Nitzan, E. Honea, U. Landman, P. Labastie, M. L. Homer, and R. L. Whetten, *Phys. Rev. Lett.* **64**, 2933 (1990).
149. M. Mons, J. Le Calvé, F. Piuzzi, and I. Dimicoli, *J. Chem. Phys.* **92**, 2155 (1990).
150. M. Schmidt, M. Mons, and J. Le Calvé, *Chem. Phys. Lett.* **177**, 371 (1991).
151. M. Schmidt, M. Mons, J. Le Calvé, P. Millié, and C. Cossart-Magos, *Chem. Phys. Lett.* **183**, 69 (1991).

152. A. Penner, A. Amirav, J. Jortner, A. Nitzan, and J. Gersten, *J. Chem. Phys.* **93**, 147 (1990).
153. F. H. Stillinger and T. A. Weber, *J. Chem. Phys.* **81**, 5095 (1984).
154. R. S. Berry, J. Jellinek, and G. Natanson, *Phys. Rev. A* **30**, 919 (1984).
155. F. G. Amar and R. S. Berry, *J. Chem. Phys.* **85**, 5943 (1986).
156. T. L. Beck, D. M. Leitner, and R. S. Berry, *J. Chem. Phys.* **89**, 1681 (1988).
157. T. L. Beck and R. S. Berry, *J. Chem. Phys.* **88**, 3910 (1988).
158. R. S. Berry, *Sci. Am.* **263**, 68 (1990).
159. D. J. Wales and R. S. Berry, *J. Chem. Phys.* **92**, 4473 (1990).
160. D. J. Wales and R. S. Berry, *J. Chem. Phys.* **92**, 4283 (1990).
161. D. L. Freeman and J. D. Doll, *Adv. Chem. Phys.* **70**, 139 (1988).
162. S. Leutwyler, *Chem. Phys. Lett.* **115**, 40 (1985).
163. J. C. Kettlet, T. F. Palmer, J. P. Simons, and A. T. Amos, *Chem. Phys. Lett.* **126**, 107 (1986).
164. H. C. Longuet-Higgins and J. A. Pople, *J. Chem. Phys.* **27**, 192 (1957).
165. J. Bösiger, R. Knochenmuss, and S. Leutwyler, *Phys. Rev. Lett.* **62**, 3058 (1989).
166a. R. Knochenmuss and S. Leutwyler, *J. Chem. Phys.* **92**, 4686 (1990).
166b. S. Leutwyler and J. Bosiger, *Chem. Rev.* **90**, 489 (1990).
167. R. Islampour and S. Mukamel, *Chem. Phys. Lett.* **107**, 2391 (1984).
168. R. Islampour and S. Mukamel, *J. Chem. Phys.* **80**, 5487 (1984).
169. E. Shalev, N. Ben-Horin, and J. Jortner, *Chem. Phys. Lett.* **177**, 161 (1991).
170. N. Ben-Horin, U. Even, and J. Jortner, *J. Chem. Phys.* **91**, 331 (1989).
171. N. Liver, A. Nitzan, and J. Jortner, *J. Chem. Phys.* **88**, 3516 (1988).
172. P. Hobza, H. L. Selzle, and E. W. Schlag, *J. Chem. Phys.* **95**, 391 (1991).
173. M. J. Ondrechen, Z. Berkovitch-Yellin, and J. Jortner, *J. Am. Chem. Soc.* **103**, 6586 (1981).
174. X. Li, M. Y. Hahn, M. S. El-Shall, and R. L. Whetten, *J. Phys. Chem.* **95**, 8524 (1991).
175. D. Chowdhury, *Spin Glasses and Other Frustrated Systems*, Princeton University Press, Princeton, NJ, 1986.
176. Z. Deng, G. J. Martyna, and M. L. Klein, *Phys. Rev. Lett.* **68**, 2496 (1992).
177. M. Abramowitz and I. A. Stegun, *Handbook of Mathematical Functions*, Dover Books, 1972.
178. J. J. Markham, *Rev. Mod. Phys.* **31**, 956 (1959).